David M. Bastidas · Emilio Cano *Editors*

Advanced Characterization Techniques, Diagnostic Tools and Evaluation Methods in Heritage Science

Springer

Advanced Characterization Techniques, Diagnostic Tools and Evaluation Methods in Heritage Science

David M. Bastidas · Emilio Cano
Editors

Advanced Characterization Techniques, Diagnostic Tools and Evaluation Methods in Heritage Science

Springer

Editors
David M. Bastidas
National Center for Education and Research on Corrosion and Materials Performance, NCERCAMP–UA, Department of Chemical, Biomolecular and Corrosion Engineering
The University of Akron
Akron, OH, USA

Emilio Cano
Centro Nacional de Investigaciones Metalúrgicas (CENIM), Corrosion and Protection of Metallic Materials for Cultural Heritage and Construction Research Group (COPAC)
Consejo Superior de Investigaciones Científicas (CSIC)
Madrid, Spain

ISBN 978-3-319-75315-7 ISBN 978-3-319-75316-4 (eBook)
https://doi.org/10.1007/978-3-319-75316-4

Library of Congress Control Number: 2018961217

This Springer imprint is published by the registered company Springer Nature Switzerland AG
The registered company address is: Gewerbestrasse 11, 6330 Cham, Switzerland

Foreword

Heritage Science is a multidisciplinary field embracing a wide array of knowledge, domains and research disciplines assisting the various aspects of Heritage Conservation, Interpretation and Management. It connects researchers from Arts and Humanities (A&H), Science, Technology, Engineering and Mathematics (STEM) and Information and Communication Technologies (ICT) working together to enhance the understanding, use, management and preservation of Cultural Heritage.

Cultural Heritage is the inheritance of our past, including tangible artefacts or intangible aspects of our culture. It helps us to understand what we are, why we are this way and where we come from. UNESCO defines Heritage as our legacy from the past, what we live with today and what we pass on to future generations. This Heritage is a source of well-being and an element of individual and collective identity. It has been increasingly recognized as a valuable asset for social and economic development, being the main element of cultural tourism and serving as inspiration and foundation of many creative industries.

The present use and future preservation of Cultural Heritage faces many challenges derived from their intrinsically fragile nature, materials degradation, environmental threats (including climate change), mass tourism, demographic changes, vandalism, terrorism, and other factors. These challenges can only be tackled by means of cutting-edge scientific and technological research and innovation in this field.

The increasing recognition of Heritage Science as a key enabler to confront this situation explains the rapid expansion of this field in recent years. According to the International Centre for the Study of the Preservation and Restoration of Cultural Property (ICCROM), the number of publications in this field has increased ninefold over the last 20 years.

Currently, Heritage Science is demanding more advanced and specific research infrastructures to carry out increasingly complex research projects. The European Union and different member countries have taken a leading role in the development

of these infrastructures by means of different projects and initiatives. One of them, the "Integrated Platform for the European Research Infrastructure ON Cultural Heritage"[1] (IPERION CH, http://www.iperionch.eu) is in the genesis of this book. IPERION CH is formed by 24 partners from Europe and USA and is offering access to a wide range of high-level scientific facilities, characterization techniques, methodologies, data and tools for advancing knowledge and innovation in the preservation of Cultural Heritage.

This book gathers the lectures of the 1st IPERION CH Doctoral Summer School on Advanced Characterization Techniques, Diagnostic Tools and Evaluation Methods in Heritage Science, with the aim of compiling into a single and accessible work the application of novel advanced characterization techniques for the study of heritage assets, its conservation condition and the evaluation of different conservation treatments. The event was organized in Madrid by the Spanish Node of IPERION CH, comprised of research groups from the Spanish National Research Council (CSIC), the Spanish Cultural Heritage Institute (IPCE) and the Prado National Museum.

The contents of the book present in a coherent and practical way several advanced and innovative characterization techniques beyond those already established in Heritage Science. The two first chapters cover applications of electrochemical techniques to monitor degradation of metallic heritage assets: the first one is devoted to their application to monitoring and controlling corrosion in reinforcing metallic elements in contemporarily built heritage, specifically those made of reinforced concrete; the second one presents a novel gel polymer electrolyte (G-PE) electrochemical cell for in-situ assessment of patinas and coatings on metallic heritage. Next chapters present different imaging techniques that allow data collection from underlayers in paintings and other materials: multispectral infrared reflectography is presented, and its advantages over traditional wide-band reflectography are discussed; the application of optical coherence tomography (OCT) and its usefulness to obtain cross sections in a non-invasive way is covered in the next chapter; and the capabilities of the nuclear magnetic resonance (NMR) analysis by means of the innovative portable NMR mouse sensor complete this second group of techniques. The book continues with the description of the capabilities of high-performance liquid chromatography coupled to UV–VIS diode array detector and tandem mass spectrometry detectors as quadrupole–time of flight (HPLC-DAD-QTOF) for the analysis of different organic components in microsamples from heritage artefacts. And the book concludes with the description of an image analysis technique based on Fourier transform to precisely characterize, count threats and compare painting canvases.

[1] IPERION CH is a project funded by the European Commission, H2020-INFRAIA-2014-2015, under Grant No. 654028.

In all cases, the fundamentals of the techniques are presented in a simple yet rigorous way and the specific advantages and challenges of their application to Heritage Science studies are discussed. This application is exemplified in all chapters with several studies of real heritage objects, showing how these innovative techniques can give answers to different questions regarding the conservation condition of objects, restoration procedures and stylistic or historic issues.

Akron, OH, USA — David M. Bastidas
Madrid, Spain — Emilio Cano

Acknowledgements

This project has received funding from the European Union's Horizon 2020 research and innovation programme under grant agreement No. 654028.

Contents

Chapter 1
On-Site Corrosion Diagnosis and Its Control by Electrochemical Techniques in Contemporary Built Heritage

David M. Bastidas and Sean Coleman

1 Introduction to Corrosion in Contemporary Built Heritage

Corrosion prevention of Contemporary Built Heritage is an essential part of the corrosion umbrella that not only includes construction, but also antiques and works of art. Preserving these treasures are crucial because it allows for their historical importance to remain to future generations, so the first step is to conserve and restore history by monitoring, maintaining and preventing corrosion.

Within the past decade there has been an increased interest in conserving the heritage of the 20th century due to the devastating effects and challenges corrosion poses for management and conservation practitioners. Lack of recognition (with the exception of the icons), and the absence of comprehensive research frameworks for identifying 20th-century heritage and correspondingly poor protection have resulted in the loss of many places that will be lamented in the near future.

Engineers in the corrosion field are constantly troubled with predicting the service-life of concrete structures due to climate change, but an important and useful laboratory and field technique for assessing reinforced concrete structures (RCS) corrosion is the use of electrochemical instruments. This is because it is aimed at monitoring corrosion without having to remove slabs of reinforced concrete, neither disturbing nor destroying the structure. These electrochemical techniques can assist engineers and technicians to decide on type of repairs and maintenance are required and to evaluate the corrosion state of the internal structure [1].

RCS proliferation of historical buildings has attracted concern due to the need to preserve and control its integrity, as shown in Fig. 1. Prompted by the need to

D. M. Bastidas (✉) · S. Coleman
National Center for Education and Research on Corrosion and Materials Performance, NCERCAMP–UA, Department of Chemical, Biomolecular and, Corrosion Engineering, The University of Akron, 302 E Buchtel Ave, Akron, OH 44325–3906, USA
e-mail: dbastidas@uakron.edu

D. M. Bastidas and E. Cano (eds.), *Advanced Characterization Techniques, Diagnostic Tools and Evaluation Methods in Heritage Science*,
https://doi.org/10.1007/978-3-319-75316-4_1

Fig. 1 Corroded rebar under concrete slab

rebuild historical building structures in Europe devastated in many places during World War II and taking the advantage of two decades of a flourishing economy that accelerated infrastructure development; it raises continual dilemmas about the advisability of undertaking costly repair operations or deciding the demolition and construction of new structures. The number of structures that are rehabilitated is increasing with respect to the structures already built, which is due to two main reasons: new practical uses attributed to existing built heritage structures that can be restored preserving their historical value and, because society takes into consideration the high costs that involves the demolition of existing structures [1, 2].

Nowadays, historical buildings are in dire need of serious overhaul to increase the value and extend the lifetime of service. Since built heritage becomes older, some conservation and preventive strategies need to be put in practice.

Usually, the rebar reinforcements are in the passive state because of concrete high pH, according to Pourbaix diagram depicted in Fig. 2 [3]. However exceptional circumstances can occur in which the passivity of the steel is destroyed, the reinforcement corroding in the active state, due to certain factors that precipitate the corrosion process, essentially, as already described in previous chapters, the carbonation of concrete and the presence of chlorides above a critical concentration threshold [1, 2]. The transition from the passive state to the active one happens then by a complex mechanism that comprises a series of successive stages.

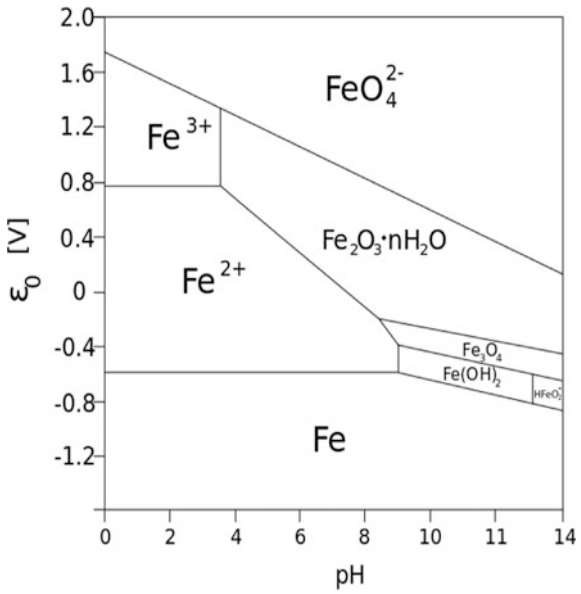

Fig. 2 Pourbaix diagram for iron in H_2O at 25 °C

1.1 *Factors Controlling Corrosion in Contemporary Built Heritage*

Corrosion of heritage buildings and structures made of concrete and reinforced steel has been identified as a main reason for their deterioration. Steel reinforcements remain in a passive state when embedded in chloride-free and non-carbonated concrete, because its high alkalinity (pH higher than 12). Passive layers formed on steel reinforcement surfaces present low dissolution reaction kinetics, which lead to very low corrosion rates. Therefore negligible risk of corrosion occurs, thus providing a long-lasting service lifetime. A corrosion life-time prediction diagram is proposed by Tutti (Fig. 3).

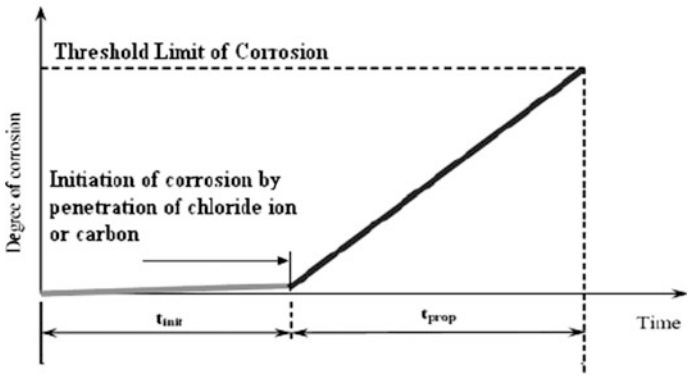

Fig. 3 Tutti diagram corrosion life-time prediction for reinforced concrete structures

It was once thought that after passivity breakdown, corrosion of steel in concrete during active state was under cathodic control, i.e. limited by oxygen access and its diffusion through the concrete pores network, to the metal surface [1, 2]. This mechanism leads to i_{corr} values around 0.1 μA/cm^2 [4]. However, either carbonated or chloride-contaminated concrete, it is commonly found that corrosion current density increase up to i_{corr} values of 10 μA/cm^2. This preliminary hypothesis, is not accepted as those i_{corr} values of 10 μA/cm^2 are larger than the dissolved oxygen diffusion limit intensity within the concrete pore solution, i_{lim,O_2}. Furthermore, those high i_{corr} values cannot either be attributed to passive films formation.

Another mechanism of this particular case is where i_{corr} values are found to be unusually high; thus, a controlling stage that allows a much faster dissolution process than the passive layers either the i_{lim,O_2}, can be assured. Previous research results show that once the passive to active transition takes place the concrete resistivity, ρ, is the key factor controlling corrosion rate.

The concrete resistivity value (ρ), strongly depends on the hydration degree of concrete pores. Moisture can ranges from 10^3 Ω cm, for saturated conditions up to 10^{11} Ω cm, for dried concrete. On the other hand, the supply of oxygen and moisture plays a crucial role on the active state of reinforcements corrosion. Mainly moisture is to be responsible for the large resistivity variations since oxygen supply is continuously present. As a result, i_{corr} shows a close dependence on concrete resistivity (ρ).

There is no consensus when establishing a threshold of ρ above which the risk of corrosion can be neglected. This is due to the lack of a clear awareness of tolerable and inadmissible corrosion rate values in reinforced concrete structures (RCS). Although it is clear and accepted with no doubt the existence of an inverse relationship between i_{corr} and ρ.

1.2 *Electrochemical Corrosion Techniques and Methods: Fundamentals and Concepts*

During last decades, great advances were made on development of electrochemical techniques and devices for on-site monitoring of corrosion processes. Different corrosion characterization techniques are included in Table 1, including direct quantification methods, accelerated corrosion test and electrochemical techniques. Advantages and drawbacks are also reported for each method.

A notable advantage is that electrochemical methods provide a true value of corrosion rate. Therefore, there is no need to use a correlation factor to quantify electrochemical data measurements with real corrosion rate. Those electrochemical techniques make possible on-site monitoring of different combinations of metal and environments.

The two most common methods for obtaining quantitative information on the corrosion rate of reinforcements are the DC linear polarization resistance method and the AC electrochemical impedance spectroscopy method [1–9]. The ideal

Table 1 Experimental corrosion characterization methods, pros and cons

Method	Pros	Cons
Direct methods		
• Gravimetric analysis • Chemical analysis • Volumetric analysis	– Direct corrosion measure, by either weight gain or loss, concentration of metal species in solution, and/or either H_2 evolution or O_2 consumption, during corrosion processes – No need of expertise to run the experiments	– Destructive methods – Very large exposure times when high corrosion resistance materials are evaluated – Obtained data results for the overall time exposed. No specific instant values are provided – Low reproducibility measurements
Accelerated corrosion testing		
• Salt spray (fog) test • Acetic acid salt spray test • Intergranular corrosion test • Stress corrosion cracking test • Fatigue corrosion test	– Short exposures times required – High versatile methods to get comparative results – Provide reliable output for materials selection	– Destructive methods – Accelerated testing conditions strongly influence corrosion mechanisms – Correlation factors are need for each testing conditions, to estimate corrosion rates under real environments – No universal correlation exist
Electrochemical methods		
Steady-state-methods • Tafel slope methods • Linear polarization resistance method • Potentiometric *Non-steady-state (transient) methods* • Electrochemical impedance spectroscopy (EIS) • DC-pulse techniques • Electrochemical noise • Cyclic Potentiodynamic Polarization	– Non-destructive methods, low applied current/voltage – High accuracy and precision on corrosion potential (E_{corr}) and corrosion current density (i_{corr}) elucidation – Fast data acquisition – Instant corrosion rates are determined – Corrosion mechanism can be elucidated by means those electrochemical methods	– Some system perturbation applies for high voltage/current range – Indirect estimate of corrosion rates – Need of expertise to elucidate corrosion mechanism and relationship between electrochemical results and the corrosion process itself

solution for studying RCS behavior would be to directly measure the corrosion rate of real size structures. The technique most widely used in the field, due to its simplicity, is that of potential measurements, whose most serious limitation is its exclusively qualitative nature [7]. The essential difficulty in real structures stems

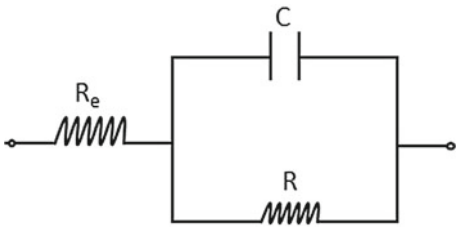

Fig. 4 Equivalent electrical circuit (EEC), used for modeling reinforced concrete structures electrochemical response

from the impossibility of knowing with certainty the surface area of the reinforcements affected by the electrical signals in the measuring process.

The signals are applied with small counter electrodes (CEs) and extend, while progressively decaying, to a critical length which is unknown in each case. Using a CE of the same size as the structures, with the aim of achieving a uniform distribution of the current lines, is obviously not possible.

The behavior of a RCS may be represented, in a first approximation, by the modified Randles circuit (Fig. 4), though other more complex circuits allow a better simulation of the steel-concrete system [1, 2].

Several researchers have explored the possibility of applying to the steel-concrete system, different corrosion rate measuring methods based on the application of short duration galvanostatic pulses [1, 2, 10], or the instantaneous discharging of a capacitor (Coulostatic method). Besides their great speed, these methods offer the advantage of causing minimal disturbance of the electrode. Following on from these valuable contributions, the objective pursued is twofold:

(i) To demonstrate that it is possible to estimate the corrosion rate of steel in concrete also by means of potentiostatic pulses, and
(ii) That by supposing an approximate value of the double layer capacitance, this estimation can be made with sufficient exactitude for many practical purposes without the need to know the surface area of the rebar.

2 Concrete as an Electrolyte

It may be surprising that concrete, a solid ceramic material with a stony appearance and consistency, behaves like an electrolyte and electrochemical methods can be applied to the study of the degradation processes of reinforcements in reinforced concrete structures (RCS). But this is indeed the case, otherwise there would be no risk of corrosion for the reinforcements. Cement mortar and concrete are porous

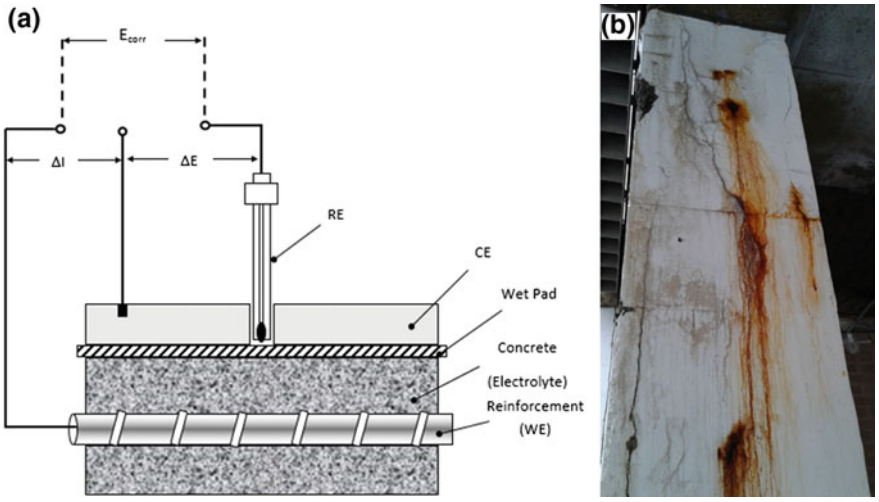

Fig. 5 **a** Wiring diagram for the application of the on-site electrochemical technique for reinforced concrete corrosion, including working electrode (WE), counter electrode (CE) and reference electrode (RE). **b** Delamination on reinforced concrete pillar caused by corrosion

materials, with an aqueous phase that partially fulfills its pore network and provides electrical conductivity. Water uptake through the concrete pore network increases as moisture increases. RCS immersed in water (docks, piers, onshore and offshore structures), they reach saturation conditions. Concrete conductivity varies between very wide limits depending on the degree of saturation of the pores [10, 11], that is, the amount of electrolyte present. There is the possibility that corrosion electrochemical cells form, as a result of the movement of the ions that are generated in local anodes and cathodes, that electrical signals can be applied to the reinforcements and, consequently, to measure their response and estimate their corrosion rate (Fig. 5). All electrochemical techniques for the study of corrosion are therefore applicable to metals embedded in concrete, having contributed to a considerable advance, since they began (during the 60s) to be used in the RCS, and to a better knowledge about the corrosion behavior of RCS in the most varied environments [10, 11].

2.1 On-Site Electrochemical Corrosion Methods

Corrosion processes involve the presence and transport of charged species, either ions or electrons. Reason why electrochemical methods provide a very useful tool to quantify those electrochemical processes and elucidate corrosion mechanisms. In 1957, Stern and Geary first introduced electrochemical quantitative methods to measure corrosion [5]. This methods was based on previous corrosion cells model

proposed by Evans and mixed potential (E_{corr}) theory established by Wagner and Traud [4].

Reviewing some electrochemical principles, it is considered electrical equivalence of both half-reactions (Eq. 1), anodic (oxidation) and cathodic (reduction) at mixed potential (E_{corr}). Therefore, it is not possible to measure any corrosion current (I_{corr}), since the electrochemical cell is producing a zero net current (I_{net}), according to Eq. 2. So, half-reaction currents are equal magnitude but with opposite sign.

$$I_t = I_a = -I_c \tag{1}$$

$$I_{net} = I_a + I_c = 0 \tag{2}$$

where, I_a and I_c, are the anodic and cathodic currents respectively. And I_{corr}, is the corrosion current.

An external electrical excitation signal needs to be applied to breakdown this half-reaction currents equality, thus allowing electrochemical measurements (Eq. 3). This is because of the zero net current at the mixed potential. In this way polarization signals are used.

The system (electrochemical cell) is polarized, resulting on an effective net current produced (Fig. 6). Thus, electrochemical measurement are applied [5]:

$$I_t = I_a - I_c = \mathrm{f}(E) \tag{3}$$

The plotted relationship between applied voltage (potential), and the obtained electrical current, or vice versa is the polarization curve.

Potential values comprised between both anodic (E_a) and cathodic (E_c) half-reaction equilibrium potentials, have a direct relationship on the overall corrosion process, thus resulting in a current value (I_t), according to Eq. 3. Polarization curve and Evans diagram is depicted in Fig. 6.

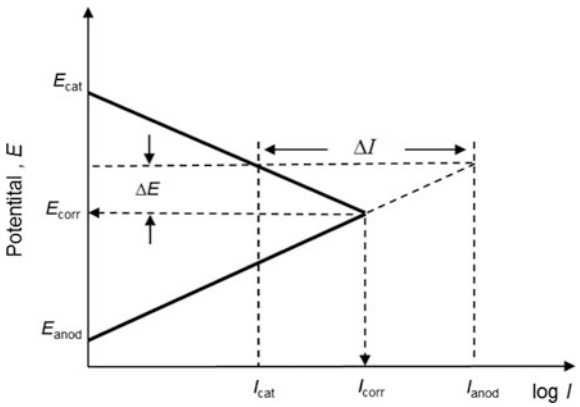

Fig. 6 Evans diagram for an electrochemical corrosion process. The application of a small polarization breaks the existing balance in the E_{corr} between I_a and I_c to enable the measure of ΔI, and to obtain the I_{corr}

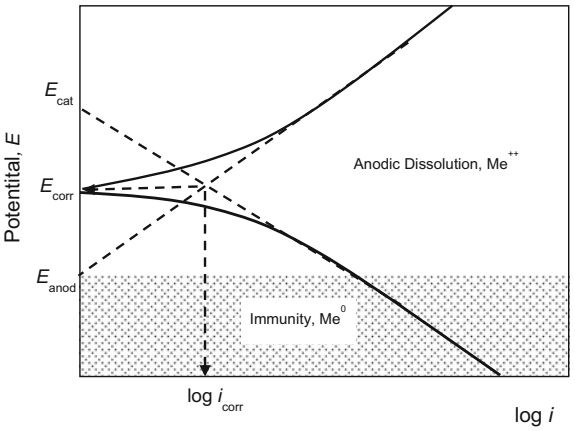

Fig. 7 Polarization plot, E versus log i. Tafel slopes for the anodic (β_a) and cathodic (β_c) half-reactions. The intersection point determines E_{corr} and i_{corr} values

A useful procedure to calculate E_{corr} and i_{corr} is the intersection method, where Tafel slopes for anodic and cathodic half-reaction are obtained using a semi-logarithmic data plot (Fig. 7), thus obtaining Tafel law, (Eq. 4):

$$\eta = \beta_a + \beta_c \log i \tag{4}$$

where, η is polarization current, β_a and β_c are the anodic and cathodic Tafel slopes, respectively, and i is current density.

For those Tafel slopes to be obtained, high polarizations need to be applied, thus producing an irreversible modification on the chemistry of the electrochemical interface metal/solution, also defined as electric double-layer. As a consequence, this method becomes destructive.

Polarization curves present a linear region nearby the corrosion potential (E_{corr}), i.e., for low polarization (η) values. An advantage of this fact is the use of the linear polarization resistance (LPR) method. Therefore, according to Stern and Geary, the slope at linear region is correlated to the corrosion rate. Thus, it is possible to establish a direct relationship between polarization resistance (R_p) and corrosion current density (i_{corr}), as it is shown in Eq. 5:

$$i_{corr} = \frac{\beta_a \beta_c}{2.303(\beta_a + \beta_c)} \frac{\Delta i}{\Delta E} = \frac{B}{R_p} \tag{5}$$

where (Δi) is current density response after an excitation potential signal (ΔE) is applied or vice versa, depending upon type of control, potentiostatic or galvanostatic.

B is defined as a constant calculated from Tafel slopes β_a and β_c. B value usually took values comprises between the range 13–52 mV [5]. In addition, i_{corr} is the corrosion current density (I_{corr}/cm^2), and R_p is polarization resistance.

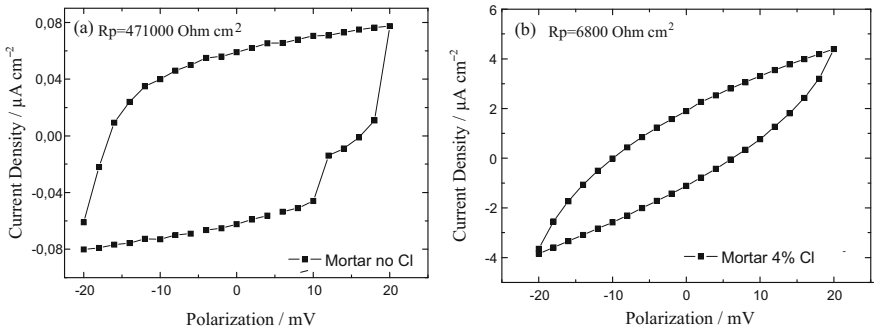

Fig. 8 **a** Steel in concrete without chlorides metal will corrode much less than, **b** steel in concrete with chlorides

The advantage of the linear polarization resistance (LPR) is that is non-destructive method. It also provides a simple and fast way to evaluate corrosion rate.

This LPR method is used to obtain R_p, as it is depicted in Fig. 8. As a consequence, high polarized systems will show a low polarization resistance (R_p) slope ($\Delta i/\Delta E$), so, in other words, corrosion resistance materials will present a high R_p, and a high hysteresis loop when plotting ($\Delta i/\Delta E$) in a cyclic, direct and reverse scan, mode.

2.2 Potentiostatic Pulse Technique Fundamentals

When the polarization of an electrode is obtained, either by a potentiostatic pulse, a galvanostatic pulse or an amount of current is interrupted, the system is represented by the EEC in Fig. 4, where the potential decay curve is exponential, immediately after the ohmic drop takes place, according to the Eq. 6:

$$\frac{\eta_t}{\eta_0} = e^{-t/CR_p} \tag{6}$$

where

η_0 maximum real polarization at the moment of current interruption, i.e., for time = 0

η_t polarization of working electrode (WE) at time t during relaxation after current interruption.

After the current interruption, the increase in the electrochemical double layer charge density is progressively consumed by the corrosion reaction, and taking logarithms of the above equation, yields to Eq. 7:

$$\ln \eta_0 - \ln \eta_t = \frac{t}{CR_p} \tag{7}$$

This expression offers two ways for calculating R_p and therefore the corrosion rate through the Stern-Geary expression [5], as shown in Eq. 8:

$$i_{corr} = B/R_p \tag{8}$$

One of the two procedures consists of determining the slope of the plot of *ln* η_t *versus t*, as has hitherto been performed [4–10]. The second procedure is based on the direct measurement of the time constant attributable to the corrosion process at the steel-concrete interface.

2.3 First Procedure: Estimation of R_p from the Slope of the Plot of t versus ln η_t

Given that η_0 is a constant value for each test, from Eq. 9, it is deduced that the plot of *t versus ln* η_t is a straight line from whose slope R_p may be deduced if the capacitance value (*C)* is known:

$$R_p = \frac{-\Delta t}{C(\Delta \ln \eta_t)} \tag{9}$$

Therefore, on the basis of real experience, it may be supposed without much error that the value of *C* is, for the system studied, between 10^{-4} and 10^{-5} F/cm^2, though much higher values may be determined for rebar that corrode in active state [10], perhaps due to the effect of the existence of voluminous corrosion products at the steel-concrete interface.

A disadvantage to be considered is that the overall process mixes several partial processes with different time constants. Previous experience allows this limitation to be overcome, since it is known that R_p is of the order of 10^4 Ω cm^2 for reinforcements that corrode in active state and around 10^5–10^6 Ω cm^2 for passive rebar. By selecting an intermediate capacitance value, *C*, e.g. 5×10^{-5} F/cm^2, it is possible to very approximately estimate the time constant of the corrosion process, $T = CR_p$, which is the magnitude of interest. Having determined *T*, the time interval (around *T*) is defined in which, in practice, the slope of the straight line for calculating R_p by Eq. 9 must be fitted. In the plot of *ln* η_t *versus t* it would be necessary to consider tenths of a second in the case of active structures and units or tens of seconds in the case of passive structures.

2.4 Second Procedure: Direct Determination of the Time Constant

For a time t = $T = CR_p$, Eq. 10 is reduced to:

$$\frac{\eta_t}{\eta_0} = e^{-1} = 0.37 \tag{10}$$

Thus, it is possible to determine the time constant of the corrosion process, $T = CR_p$, by measuring the time in which η_t is reduced to 37% of its initial value (Fig. 9).

As C is directly proportional to the surface area of the capacitor (electrochemical double layer) and R_p is inversely proportional, T is independent of this magnitude. Consequently, if the C value per unit of surface area is inserted in the preceding equations, the R_p of the rebar per unit of surface area will be calculated, without the total number or diameter of rebars being of importance.

As a result, the possible interference of other partial processes besides corrosion must be of little importance, or must occur in very different times to those used in the measurements, in order not to mask the potential decay due to the corrosion process.

The direct measurement of T to determine R_p applying galvanostatic pulses [1, 2]; though previously determining the interfacial capacitance from the charge injected, the potential shift achieved, and the surface area of the steel. The authors of the present work have shown that it is possible to estimate, with galvanostatic pulses, reliable values of R_p in RCSs without the need to know the surface area of the rebar, considering an approximate value of the capacitance.

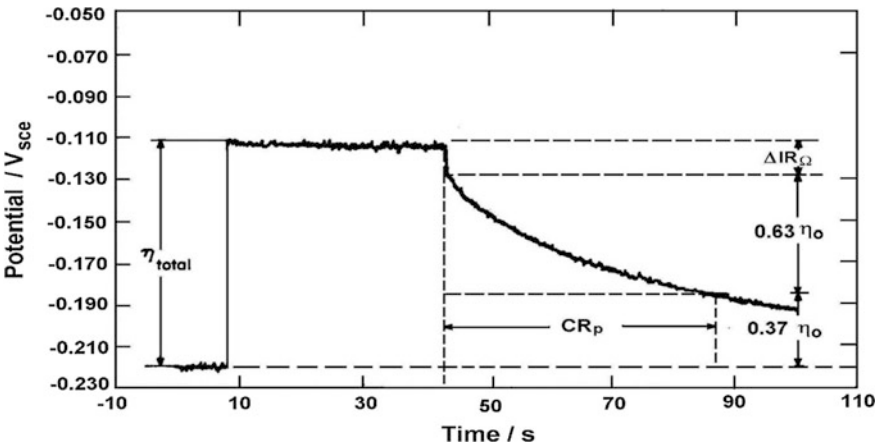

Fig. 9 Potentiostatic pulse technique, a non-destructive method to determine polarization resistance, R_p

2.5 EIS: An Alternating Current (AC) Technique

Electrochemical Impedance Spectroscopy (EIS), is an advantageous technique for on-site measurement of corrosion rate in Contemporary Built Heritage. The use of EIS, represents a non-destructive technique that allows to elucidate corrosion process mechanisms.

The EIS measurements determine the impedance magnitude (Z) of an electrochemical system, which allows to obtain polarization resistance values [12–15]. Therefore corrosion rate is determined for steel reinforcements in concrete in a non-destructive way.

The application of small potential (E) excitation signals, using alternating current over a wide frequency range (ω), allows to obtain the impedance value. The Z value is composed of a real (Z_{real}) and an imaginary (Z_{imag}) part, (Eq. 11). Graphical chart includes real part plotted on x-axis and negative imaginary part on y-axis, resulting on the so-called Nyquist plot. Each point on the plot will represent the impedance Z value for a given single frequency (Fig. 10).

$$Z = \frac{E}{I} = Z_0 e^{(i\emptyset)} = Z_0(\cos\emptyset + i\sin\emptyset) \tag{11}$$

On the Nyquist plot the impedance can be represented as a vector of length $|Z|$. The angle between this vector and the x-axis is the phase angle ∅.

Low frequency data are on the right side of the plot and higher frequencies are on the left. This is true for EIS data where impedance usually falls as frequency rises (this is not true of all circuits).

The Nyquist plot represents the results from the RC circuit [16, 17]. The obtained semicircle is characteristic of a single time constant. Electrochemical Impedance plots often contain several time constants. Often only a portion of one or more of their semicircles is seen.

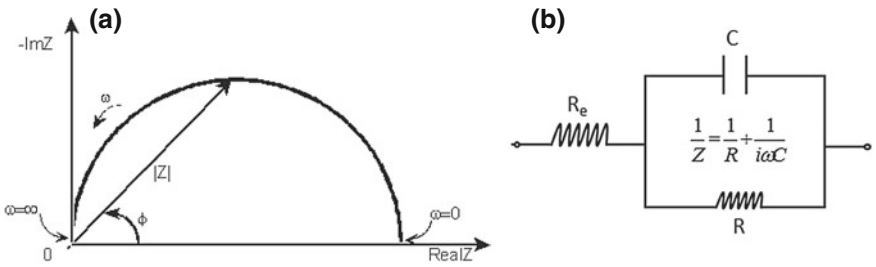

Fig. 10 **a** Nyquist diagram obtained using EIS, a non-destructive AC-electrochemical technique. **b** Ranldes electrical equivalent circuit (EEC), use to model electrochemical impedance response of the interface

The electrochemical double layer is formed because the presence of an interface. For steel in concrete, interfaces are the result of different nature composition system, in this case, contact area of steel reinforcements and concrete contitutes an interface, but also corrosion products will enable extra interfaces, between those and the steel and also in between corrosion products and the concrete itself [18]. Double-layers at interfaces behave as an electrical circuits, thus when an external potential is applied they get charged with time-delay between its input and output.

Electrochemical interfaces they work as capacitors, therefore when potential (V) signals are applied to a discharged capacitor, the capacitor will charge while if voltage is release, the capacitor discharges in the opposite direction. The accumulated charge (Q) on the capacitor is obtained by Eq. 12:

$$Q = V \cdot C \tag{12}$$

The time delay between charging either discharging process is known as the time constant (T) of the electric circuit for each single electrochemical system. The resultant time constant depends upon the reactive components either capacitive or inductive connected to it and is a measurement of the response time. This transient response time constant is obtained by Eq. 13:

$$T = R \cdot C \tag{13}$$

Considering transient response of the system, it appears to be crucial achieving and steady-state situation to study the steel-concrete system, in order to get robust and reproducible results. A common problem in EIS measurements and their analysis is drift in the system being measured. In practice, a steady state can be difficult to achieve (Fig. 11). The electrochemical cell can change through adsorption of solution impurities, growth of an oxide layer, build-up of reaction

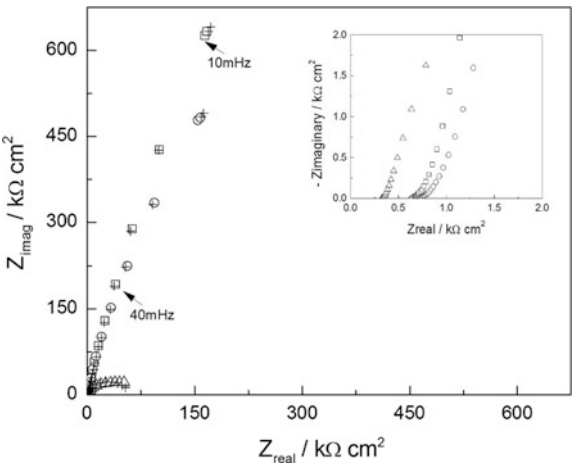

Fig. 11 Nyquist plot obtained using EIS technique for steel reinforced concrete

products in solution, coating degradation, temperature changes, diffusion processes, among others. EIS analysis tools may provide inaccurate results on a system, if measurements are performed on non-steady-state conditions.

In polarization processes on electrochemical systems, applied excitation potential (V_c), has a direct relationship with capacitor charge, $V_c = Q/C$. If transient response is considered, the potential across the electrochemical double layer, considered as a capacitor (V_c), presents a narrow dependence on the applied external potential (V_{ext}) at any instant in time during the charging period is given as (Eq. 14):

$$V_c = V_s\left(1 - e^{-t/CR_p}\right) \tag{14}$$

where

V_c is the voltage across the capacitor
V_s is the supply voltage
t is the elapsed time since the application of the supply voltage
CR_p is the *time constant* (T) of the RC charging circuit.

After a period equivalent to 4 time constants, (4 T) the capacitor in this RC charging circuit is virtually fully charged and the voltage across the capacitor is now approx. 98% of its maximum value, 0.98 × V_s. The time period taken for the capacitor to reach this 4 T point is known as the transient period.

After a time of 5T the capacitor is now fully charged and the voltage across the capacitor, (V_c) is equal to the supply voltage, (V_s). As the capacitor is fully charged no more current flows in the circuit. The time period after this 5 T point is known as the steady state.

This time constant represents the value depending on type of electrochemical process involved in the corrosion reaction. Therefore, determination of the time constant will allow elucidation of polarization resistance (R_p). According to Stern and Geary equation [5], that R_p will provide a corrosion rate value.

3 Corrosion Control in Built Heritage

By retarding either the anodic or cathodic reactions the rate of corrosion can be reduced, thus avoiding corrosion products to form on the metal surface (Fig. 12). This can be achieved in several ways.

Fig. 12 Corroded rebars showing the oxide scale

3.1 Conditioning the Metal

This can be sub-divided into two main groups: (a) Surface treatment and coating the metal, in order to interpose a corrosion resistant coating between metal and environment. The coating may consist of: another metal, e.g. zinc or tin coatings on steel, a protective coating derived from the metal itself, anodic coating or protective native oxide, organic coatings, such as resins, polymers, paints, enamel, oils and greases. The action of protective coatings is often more complex than simply providing a barrier between metal and environment [19]. Paints may contain a corrosion inhibitor. By galvanizing process, zinc coating in iron or steel confers cathodic protection. (b) Alloying the metal to produce a more corrosion resistant alloy, e.g. stainless steel, in which ordinary steel is alloyed with chromium and nickel. Stainless steel is protected by an invisibly thin, naturally formed film of chromium oxide Cr_2O_3.

3.2 Conditioning the Corrosive Environment

Influencing the cathodic reaction (oxygen reduction) from water systems in the pH range 6.5–8.5 provides a solution for corrosion to be absent. The removal of oxygen could be achieved by the use of strong reducing agents e.g. sulfite. However, for

open evaporative cooling systems this approach to corrosion prevention is not practical since fresh oxygen from the atmosphere will have continual access.

The use of corrosion inhibitors compounds is an effective and cost viable solution for corrosion control. Corrosion inhibitors are chemical additives, whose, when added to a corrosive environment, reduce the corrosion rate [20].

Corrosion inhibitors work in one of the following ways:

Anodic inhibitors, as the name implies an anodic inhibitor interferes with the anodic process, dissolution of metal.

$$Fe \rightarrow Fe^{2+} + 2e^{-} \tag{15}$$

If an anodic inhibitor is not present at a concentration level sufficient to block off all the anodic sites, localized attack such as pitting corrosion can become a serious problem due to the oxidizing nature of the inhibitor which raises the metal potential and encourages the anodic reaction (Eq. 15). Other examples of anodic inhibitors include orthophosphate, nitrite, ferricyanide and silicates.

Cathodic inhibitors, the major cathodic reaction in corrosion processes is the reduction of oxygen, (Eq. 16).

$$^{1}/_{2}O_2 + H_2O + 2e^{-} \rightarrow 2OH^{-} \tag{16}$$

There are other cathodic reactions and additives that suppress these reactions called cathodic inhibitors. They function by reducing the available area for the cathodic reaction. This is often achieved by precipitating an insoluble species onto the cathodic sites. Zinc ions are used as cathodic inhibitors because of the precipitation of $Zn(OH)_2$ at cathodic sites as a consequence of the localized high pH.

Mixed inhibitors, because of the danger of pitting when using anodic inhibitors alone, it became common practice to incorporate a cathodic inhibitor into formulated performance was obtained by a combination of inhibitors interfering both anodic and cathodic reactions [21]. This corrosion inhibition process is generally referred to a ‘synergism’ and demonstrates the synergistic action which exists between zinc and chromate ions.

Other classification refers to adsorption type corrosion inhibitors. Many organic corrosion inhibitors work by an adsorption mechanism. The resultant film of chemisorbed inhibitor is then responsible for protection either by physically blocking the surface from the corrosion environment or by retarding the electrochemical processes. The main functional groups capable of forming chemisorbed bonds with metal surfaces are amino ($–NH_2$), carboxyl (–COOH), and phosphonate ($–PO_3H_2$) although other functional groups or atoms can form co-ordinate bonds with metal surfaces.

3.3 Electrochemical Control

Since corrosion is an electrochemical process its progress may be studied by measuring the changes which occur in metal potential with time or with applied electrical currents. Conversely, the rate of corrosion reactions may be controlled by passing anodic or cathodic currents into the metal. If, for example, electrons are passed into the metal and reach the metal/electrolyte interface (a cathodic current) the anodic reaction will be stifled while the cathodic reaction rate increases. This process is called cathodic protection and can only be applied if there is a suitable conducting medium such as earth or water through which a current can flow to the metal to be protected in most soils or natural waters corrosion of steel is prevented if the potential of the metal surface is lowered by 300 or 400 mV. Cathodic protection may be achieved by using a DC power supply (impressed current) or by obtaining electrons from the anodic dissolution of a metal low in the galvanic series such as aluminum, zinc or magnesium (sacrificial anodes). Similar protection is obtained when steel is coated with a layer of zinc. Even at scratches or cut edges where some bare metal is exposed the zinc is able to pass protective current through the thin layer of surface moisture. In certain chemical environments it is sometimes possible to achieve anodic protection, passing a current which takes electrons out of the metal and raises its potential. Initially this stimulates anodic corrosion, but in favorable circumstances this will be followed by the formation of a protective oxidized passive surface film.

Acknowledgements Authors gratefully acknowledge The University of Akron for funding support.

References

1. Bastidas DM et al (2007) A quantitative study of concrete-embedded steel corrosion using potentiostatic pulses. Corrosion 63:1094–1100
2. González JA (2007) F.N. Speller Award lecture: prediction of reinforced concrete structure durability by electrochemical techniques. Corrosion 63:811–818
3. Pourbaix M (1974) Atlas of electrochemical equilibria in aqueous solutions, 2nd English edn. National Association of Corrosion Engineers, Houston, TX, USA
4. ASTM G59–97 (2014) Standard test method for conducting potentiodynamic polarization resistance measurements. ASTM International, West Conshohocken, PA, USA
5. Stern M, Geary AL (1957) Electrochemical polarization I. A theoretical analysis of the shape of polarization curves. J Electrochem Soc 104:56–63
6. Wagner C, Traud W (1938) The analysis of corrosion procedures through the interaction of electrochemical partial procedures and on the potential difference of mixed electrodes. Z Elektroch 44:391–402
7. Evans UR (1946) Metallic corrosion, passivation and protection. In: Arnold E (ed). London, UK

8. Birbilis N, Cherry BW, Forsyth M, Nairn KM (2001) A consideration of the limitation of polarization resistance method to determine corrosion status of concrete reinforcement. Proc Conf Eng Mater, 277–282
9. Scully JR (2000) Polarization resistance method for determination of instantaneous corrosion rates. Corrosion 56:199–218
10. Bastidas DM, Medina E (2013) Armaduras de acero inoxidable "Stainless steel reinforcements". Cedinox (ed). Madrid, Spain
11. Bastidas DM et al (2008) Electrochemical rehabilitation methods for reinforced concrete structures: advantages and pitfalls. Corros Eng Sci Technol 43:248–255
12. Cano E, Lafuente D, Bastidas DM (2010) Use of EIS for the evaluation of the protective properties of coatings for metallic cultural heritage: a review. J Solid State Electrochem 14:381–391
13. Feliu V, González JA, Feliu S (2007) Corrosion estimates from the transient response to a potential step. Corros Sci 49:3242–3255
14. Feliu V, González JA, Feliu S (2004) Algorithm for extracting corrosion parameters from the response of the steel-concrete system to a current pulse. J Electrochem Soc 151:B134–B140
15. González JA, Miranda JM, Feliu S (2004) Considerations on reproducibility of potential and corrosion rate measurements in reinforced concrete. Corros Sci 46:2467–2485
16. Feliu V, González JA, Andrade C, Feliu S (1998) Equivalent circuit for modelling the steel-concrete interface. I. Experimental evidence and theoretical predictions. Corros Sci 40:975–993
17. Feliu V, González JA, Andrade C, Feliu S (1998) Equivalent circuit for modelling the steel-concrete interface. II. Complications in applying the Stern-Geary equation to corrosion rate determinations. Corros Sci 40:995–1006
18. González JA, Feliu S, Rodríguez P (1997) Threshold steel corrosion rates for durability problems in reinforced structures. Corrosion 53:65–71
19. Bastidas DM et al (2015) Corrosion inhibition mechanism of phosphates for early-age reinforced mortar in the presence of chlorides. Cem Concr Comp 61:1–6
20. Bastidas DM et al (2010) A prediction study of hydroxyapatite entrapment ability in concrete. Constr Build Mater 24:2646–2649
21. Bastidas DM et al (2013) Comparative study of three sodium phosphates as corrosion inhibitors for steel reinforcements. Cem Concr Comp 43:31–38

Chapter 2
Electrochemical Techniques for in situ Corrosion Evaluation of Cultural Heritage

Emilio Cano and Blanca Ramírez Barat

1 Introduction to Electrochemical Techniques

1.1 Electrochemical Techniques

Corrosion is the main cause of deterioration of metallic cultural heritage. With the exception of those made in noble metals, any metal object in contact with its environment will corrode by an electrochemical reaction in which in the metal (M) oxidizes, giving off one or more electrons to another species in the surroundings (Fig. 1). Although it is an inevitable process, conservation science can help to restrain the velocity of the degradation and reduce the undesirable consequences through identification of the degradation causes (diagnosis), finding methods to slow down the degradation (treatment) and prediction of the evolution over time (prognosis). For this purpose conservation science requires a comprehensive approach. A global knowledge about the object is essential for the conservators to design the most appropriate conservation programme for each object. The analysis of meaning and values of the object, general condition, composition and structure through visual inspection, documentary resources and analytical techniques (XRF, Raman, XRD, SEM-EDX, LIBS, etc.) are nowadays part of the conservator's routine work. But when dealing with metals, there is another question that has to be addressed, the corrosion process. Being corrosion an electrochemical process, electrochemical techniques provide a suitable tool for this purpose.

Electrochemical techniques are based in three parameters: potential (E), current (I) and time (t). The combination of these parameters gives a broad range of

E. Cano (✉) · B. Ramírez Barat
Centro Nacional de Investigaciones Metalúrgicas (CENIM), Corrosion and Protection of Metallic Materials for Cultural Heritage and Construction Research Group (COPAC), Consejo Superior de Investigaciones Científicas (CSIC), Ave. Gregorio del Amo 8, 28040 Madrid, Spain
e-mail: ecano@cenim.csic.es

D. M. Bastidas and E. Cano (eds.), *Advanced Characterization Techniques, Diagnostic Tools and Evaluation Methods in Heritage Science*,
https://doi.org/10.1007/978-3-319-75316-4_2

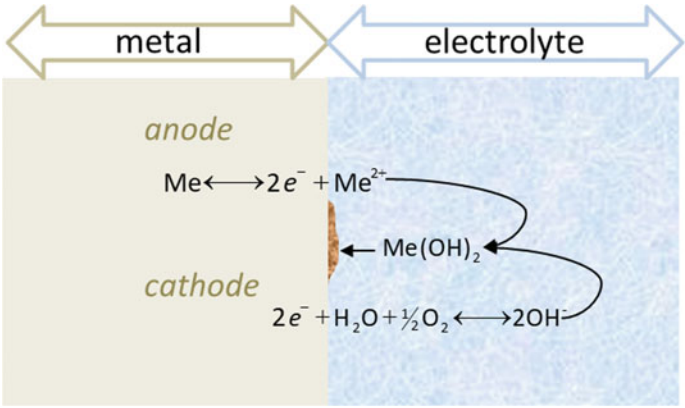

Fig. 1 Typical corrosion mechanism of metals, in aerated neutral solution. The metal is oxidized and dissolved into the electrolyte, while the oxygen contained in it is reduced to hydroxyl ions, which precipitate with the metal ion as a hydroxide

techniques with different applications in analytics and diagnostic: polarization resistance (Rp), polarization curves (Tafel), voltametry, potentiostatic and galvanostatic techniques, electrochemical noise (ECN), electrochemical impedance spectroscopy (EIS), etc. These techniques are widely used in research laboratories and industry for corrosion studies and evaluation of protection systems. Among them, EIS is the main technique used for corrosion and protection studies since the 80s. In addition to providing quantitative information of corrosion rates and information about the mechanisms, they offer very high sensibility and require relatively simple and inexpensive equipment.

In the field of metallic cultural heritage studies, despite these advantages, electrochemical techniques are best known by metal conservators-restorers as a tool for restoration treatments ("electrolytic cleaning") and their use for corrosion and protection studies in metallic cultural heritage is more recent and far from being a routine method.

1.2 EIS Fundamentals

EIS is based on the application of a small AC voltage (E) signal (usually 10 mV) to the system under study, and measuring the AC current (I) response for a certain frequency range (typically 10^{-3}–10^{5} Hz). From the relation E/I, the impedance is obtained as a function of frequency.

$$Signal: E(t) = E_0 \text{sen}(\omega t) \rightarrow Response: I(t) = I_0 \text{sen}(\omega t + \varphi)$$

$$Z(t) = \frac{E(t)}{I(t)} = Z_0 \frac{\text{sen}(\omega t)}{\text{sen}(\omega t + \varphi)}$$

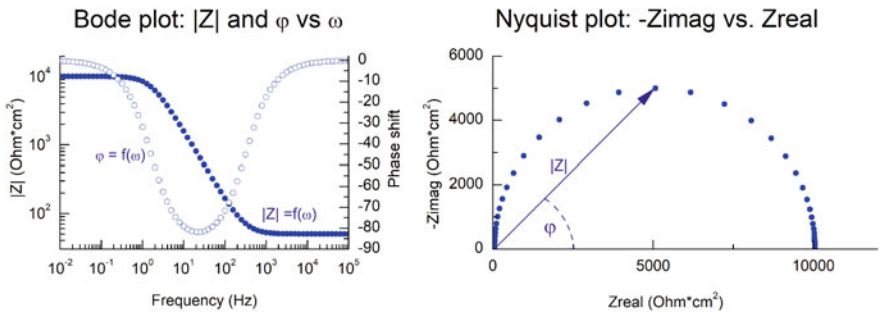

Fig. 2 Typical representation of EIS spectra

EIS spectra can be represented in different ways, being Bode and Nyquist plots the more common (Fig. 2). Bode plots represent the impedance modulus, |Z| or Z_0, and the phase shift, φ, versus the frequency in a logarithmic scale, and is particularly appropriate to represent large variations in the Z values. A Nyquist plot is a representation of the impedance vector, with the imaginary part on the y-axis and the real part on the x-axis. This plot is preferred to present more clearly certain features such as diffusion effects.

1.3 Interpretation of EIS

EIS is a very powerful technique that provides a lot of information on the electrochemical processes in the surface of the metal. However, extracting this information from experimental results is not a trivial task. Some simplistic interpretations, based on parameters such as the impedance modulus at low frequencies are commonly used and can be sufficient for comparison purposes in known systems [1]. This value is equivalent to the sum of the contribution to total impedance of all aforementioned elements and processes, thus it can be taken as a general estimation of the resistance of the system against corrosion.

In order to obtain in-depth information, EIS spectra are frequently interpreted using equivalent circuits which try to reproduce the electrical behavior of the system. In those circuits, parallel and series combinations of passive electrical elements such as capacitors and resistances are used to describe the different physical elements and processes in the system under study. Other elements specific for electrochemical systems, such as Constant Phase Elements (CPE) or Warburg impedance, are frequently employed. CPE are used in cases such as non-uniform coatings, surface roughness or inhomogeneous distributions of the current/potentials, which produce an electrochemical response departing from the behavior of an ideal capacitor. Warburg impedance is an element that models the impedance associated to diffusion (i.e. mass transfer) processes and is commonly

used when the diffusion of species through the pores of the coating or corrosion products controls the corrosion rate.

While many circuits can be fitted to the experimental data, extracting useful information requires selecting a circuit which is physically meaningful. A typical example is presented in Fig. 3 for a coating-metal system. R_e represents the electrolyte resistance, while a capacitor, C_{coat}, in parallel with a resistance, R_{coat}, model the capacitance and resistance of the protective coating in an ideal situation. If the coating is damaged or not completely protective then the circuit changes, and as the electrolyte reaches the metal surface through the pores and corrosion takes place, a new R-C pair appears. The corrosion process can be represented by a capacitor for the double layer capacitance, C_{dl}, in parallel with the charge transfer resistance, R_{ct}. In this case, C_{coat} is still the coating capacitance, R_{po} models the resistance or ionically conducting path across the coating ("pores" or defects).

Each of these elements as well as its position in the circuit shows a characteristic feature in the EIS spectra. Figure 4 shows four common equivalent circuits and their characteristic appearance both in the Bode and Nyquist plot.

Figure 4a, b present at typical EIS spectra of the systems depicted in Fig. 3. Figure 4c present a defective coating response, similar to 4b, in which the capacitors are replaced by CPE, producing a characteristic depress of the semicircles in

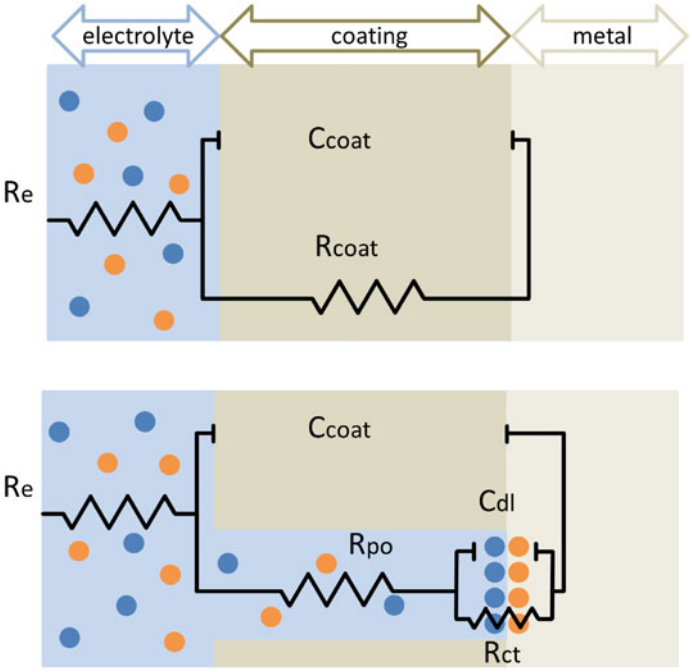

Fig. 3 Scheme of typical equivalent circuits in a coating-metal system

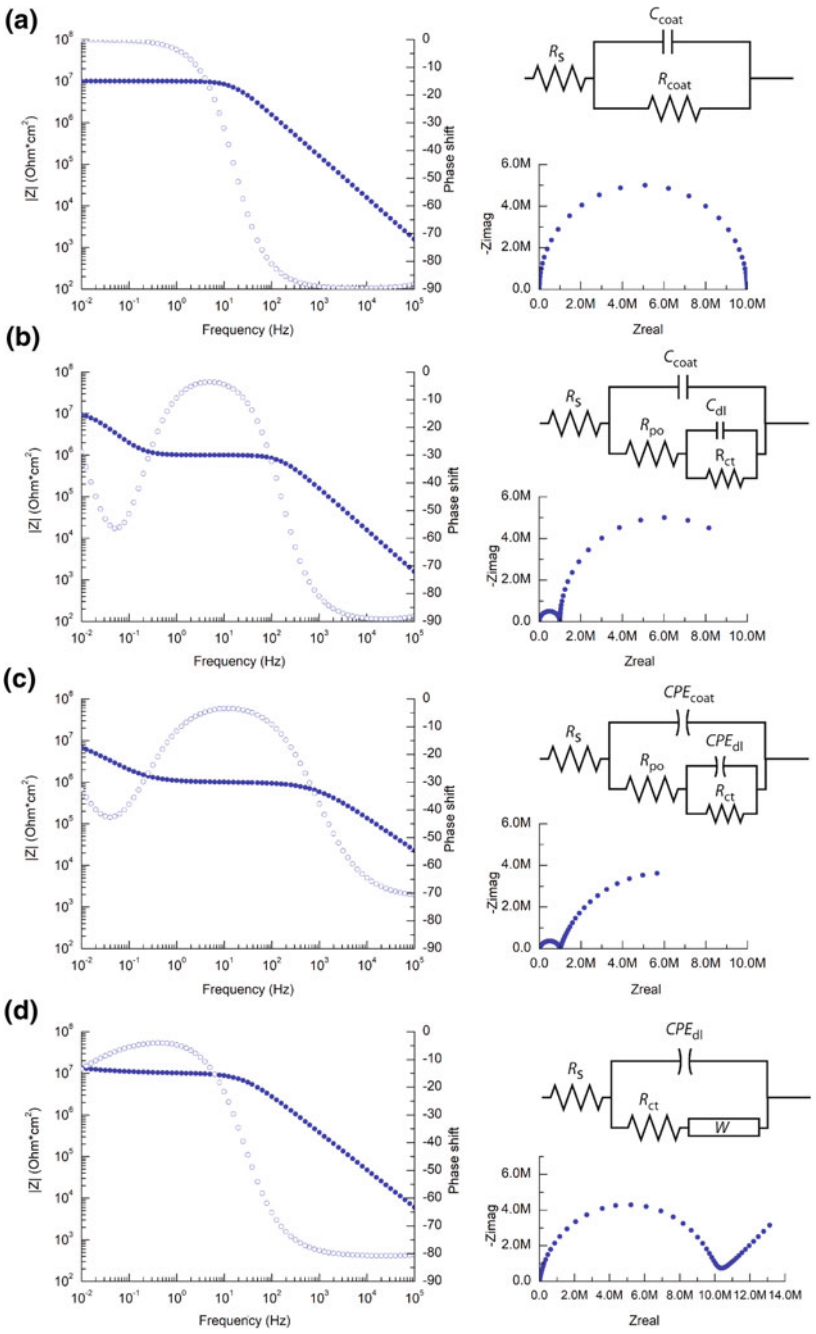

Fig. 4 Bode and Nyquist plots of different equivalent circuits

the Nyquist plot. A typical circuit modelling diffusive process is shown in Fig. 4d producing a distinctive 45° tail in the low-frequency region of the Nyquist plot.

2 Experimental Setup

2.1 Electrochemical Cell

EIS experiments for corrosion studies are normally carried out with a classical 3-electrode electrochemical cell, with a reference electrode (RE) as reference for electrochemical potential, a counter electrode (CE) which is an inert electrode to close the circuit, and the working electrode (WE) being the material under study. The most common RE are SCE or Ag/AgCl, while the CE is made of a bar, wire or mesh of an inert material (platinum, graphite, stainless steel…).

According to the object of study, traditional cells usually adopt two different configurations: immersion cell and flat cell. In the immersion cell the object is placed inside the cell, submerged in the electrolyte; while the flat cell is fixed to the (flat) surface of the metal, exposing only a limited area of the WE to the electrolyte. In these cells, different aqueous electrolytes can be used in order to simulate real environment conditions. The most common ones for cultural heritage studies are NaCl 0.1 M, Harrison electrolyte (0.35% $(NH_4)_2SO_4$ + 0.05% NaCl), mineral water [2], K_2SO_4 0.25 M [3] and acetic acid [4]. Although for laboratory tests the selection of the electrolyte relies on the nature of metal/environment interaction under study, when working on real heritage objects, it is mandatory to use mild electrolytes, in order to avoid any damage to the surface. For this purpose, mineral water or mild artificial rain are adequate choices [5].

Immersion cell and flat cells have been used in laboratory studies to evaluate waxes, oils and coatings [3, 6, 7] for metallic heritage protection on flat samples, usually artificially produced coupons that try to mimic the surface of actual artifacts. Nevertheless, these conventional setups are not suitable for large objects or in situ measurements on the irregular surfaces of sculptures and monuments.

2.2 Electrochemical Techniques in situ

To overcome the difficulties in field measurements three basic approaches have been proposed: trying to fix a traditional-like cell to the monument surface [8], retaining the liquid electrolyte absorbed in a cloth or sponge [2, 9] or using a solid gel electrolyte [10, 11]. Some designs have given acceptable results and are being further developed while others have been soon abandoned.

The first portable cell specifically tailored to electrochemical measurements on metallic heritage was designed by Paola Letardi [2]. She proposed a contact cell

Fig. 5 Contact cell designed by P. Letardi

constructed with two concentric AISI316 stainless steel electrodes, which act as CE and RE, embedded in a PTFE cylinder. The electrolyte is supported by a cloth attached to the basis of the cylinder. To avoid drying, it is connected to a small electrolyte reservoir (Fig. 5). This cell has shown to be an effective device for EIS measurements, and has been used in different studies [12–15]. Nevertheless it still has the inconvenience of handling the liquid electrolyte, and the rigidity of the cell limits its adaption to surfaces.

Researchers from the Politecnico di Torino have been working in the design of a complete portable system for in situ measurements [8]. Although their main contribution is in the design of low-cost instruments for corrosion studies, they have also explored different cell setups both with liquid and solid electrolytes, including commercial electrocardiogram (ECG) electrodes [16, 17]. The use of gel electrodes such as those for ECG represents an interesting solution to overcome the inconveniences of handling liquid electrolytes in field measurements. Unfortunately, it is not that simple and commercial ECG electrodes have shown different problems, introducing distortions in measurements due to low conductivity and inhomogeneity in the gel thickness [16]. Clare and coworkers have explored further possibilities of this approach by developing/optimizing the gel formulation. These gel electrodes are based on AMPS/PAA (2-acrylamido-2-methyl-propanesulfonic acid/polyacrylic acid) copolymers [10, 18], equilibrated with different electrolytes. Besides modifications in the gel formulation, Clare and coworkers propose the use of a double cell setup, separating the RE and CE from the WE contact. This would allow electrochemical measurements without the need of physical contact with the metal surface under the coating. Nevertheless, this cell has also two main drawbacks: the limited options for the electrolyte, as it is determined by the gel; and possible problems in current distribution.

2.3 Gel Polymer Electrolyte (G-PE) Cell

As an alternative to previously described systems we propose the use of a traditional electrolyte gelled with agar [19]. A small amount of agar is dissolved in a liquid electrolyte, poured inside the cell and left to cool. When the agar solidifies, the cell cap is removed leaving a protruding gel cylinder which is placed in contact with the surface under study. The effect of using an agar gelled electrolyte has been carefully studied [11], showing that there is an increase electrolyte conductivity, and a slightly increase in the anodic reaction rate (when used in concentrations above 3%). Despite these effects, agar does not affect the corrosion mechanisms, thus can be used for comparative studies.

Figure 6 shows the construction and use of the G-PE cell. The cell follows the conventional three-electrode design. The reference electrode and the counter electrode are fixed in a two-piece plastic mold. An AISI316 stainless steel wire is used as a pseudo-reference electrode, and the CE is made of an AISI316 stainless steel mesh. Different RE and CE electrodes and cell geometries have been tested to optimize the cell design and minimize possible artifacts from the setup [20, 21].

This cell provides several advantages for in situ EIS measurements. The use of a solid electrolyte allows measuring in any position, and the flexibility of the gel can adapt to surface irregularities. Besides, agar is a cheap and easy to handle material, and allows using a wide range of aqueous solutions as electrolyte. Finally, although a pseudo-reference electrode may be more convenient for field measurements, a real reference electrode can be used [21].

This cell has been validated in laboratory studies to assess the loss of protective properties of coatings for bronze. Figure 7 shows an example of the EIS spectra of three traditional coatings used in conservation of metallic heritage applied on bronze coupons, Incralac, Paraloid B72 and Cosmolloid H80, and how changes in their protective properties can be measured using EIS and the G-PE cell after a brief outdoor exposure [22].

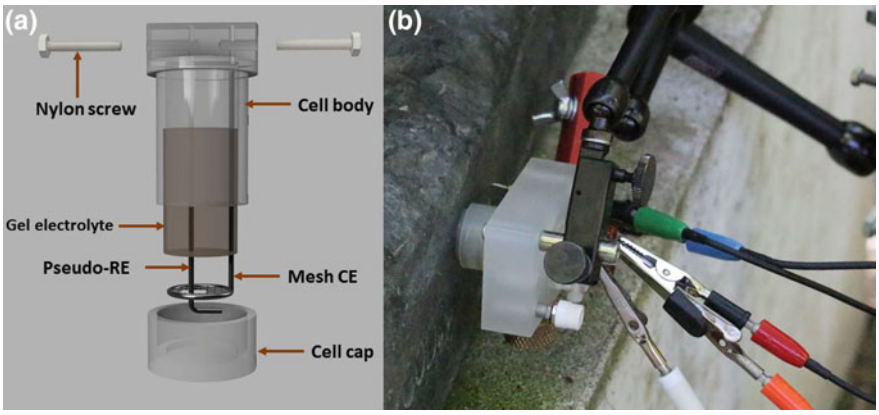

Fig. 6 G-PE cell design and in situ application

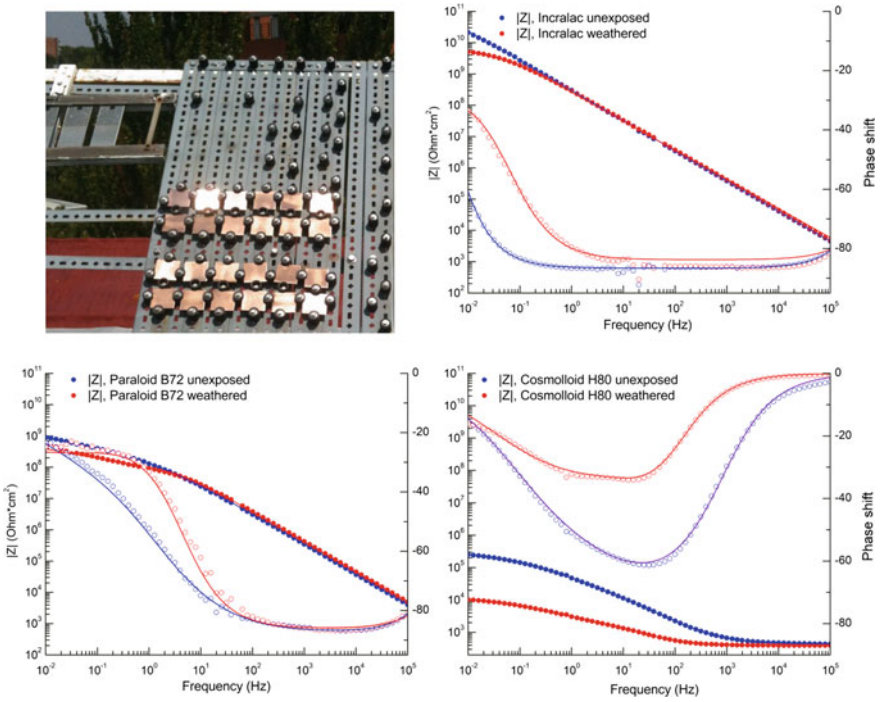

Fig. 7 EIS spectra of Incralac, Paraloid B72 and Cosmolloid H80 over bronze coupons, after preparation (blue) and a short atmospheric exposure (red) [22]

Coating degradation has also been measured on outdoor bronze sculpture. The conservation treatment of the bronze sphinxes at the National Archaeological Museum has been followed in situ by means of the G-PE cell [23]. The corrosion resistance of two areas of one of the sphinxes, one with a green patina (GP) and one with a dark patina (DP) was measured (Fig. 8) and compared before and after the treatment, and the evolution of the Incralac coating which was applied, followed over time.

The G-PE has also shown to be very useful to the study of weathering (Cor-Ten) steel surfaces, which are can be highly textured and porous. Differences in corrosion resistance of artificial patinas have been evaluated using this cell [24], showing that chemical treatments applied by artists to accelerate the *patination* of weathering steel reduce the corrosion resistance. Field studies have also shown that it is possible to appreciate significant differences in different areas of the same sculpture, which is of relevance for the establishment of an adequate conservation protocol [25–27].

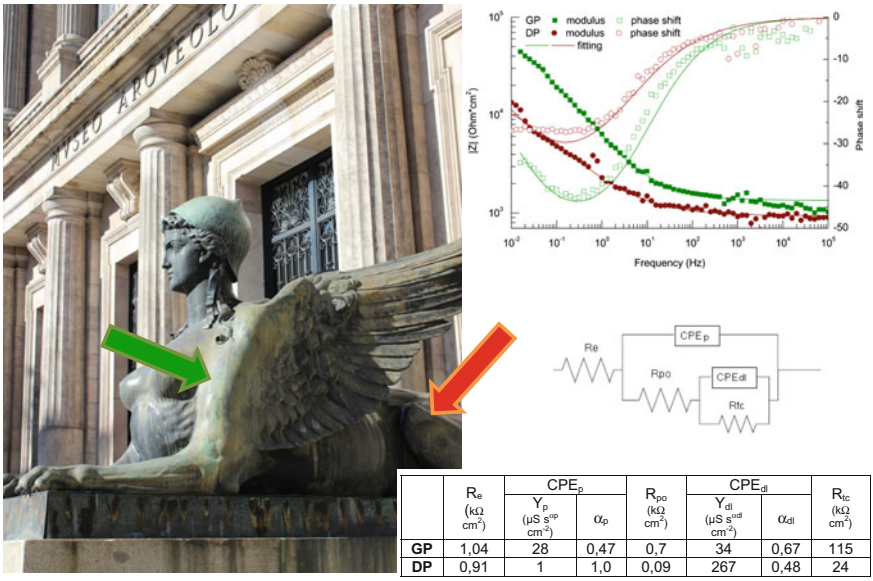

	R_e ($k\Omega\ cm^2$)	CPE_p		R_{po} ($k\Omega\ cm^2$)	CPE_{dl}		R_{tc} ($k\Omega\ cm^2$)
		Y_p ($\mu S\ s^{np}\ cm^{-2}$)	α_p		Y_{dl} ($\mu S\ s^{\alpha dl}\ cm^{-2}$)	α_{dl}	
GP	1,04	28	0,47	0,7	34	0,67	115
DP	0,91	1	1,0	0,09	267	0,48	24

Fig. 8 EIS study of a bronze sphinx at the National Archaeological Museum of Spain. The EIS spectra of the selected green and dark areas of the patina showed that the green patina was about five times more protective than the dark one

3 Conclusions

Electrochemical techniques in general, and specially EIS, can provide quantitative and qualitative information on the corrosion processes responsible for the degradation of the metallic cultural heritage and the protective properties of coatings and other systems employed in the conservation treatments.

In many cases, these studies need to be carried out in situ, on the surface of the real artifacts. Several approaches have been proposed by heritage scientist to tackle the practical issues of these in situ measurements. A gel-polymer electrolyte electrochemical cell (G-PE), specifically tailored for cultural heritage, has been developed by our research group. This cell allows in situ electrochemical tests on metallic cultural heritage, where the use of traditional cells is not possible. It has been proved to provide relevant information for the conservation assessment, giving good results both in laboratory samples and field measurements.

Acknowledgements This work has been funded by EU project "Integrated Platform for the European Research Infrastructure on Cultural Heritage" (IPERION-CH, Ref. H2020-INFRAIA-2014–2015, GRANT no. 654028), by project HAR2014-54893-R from the Ministerio de Economía, Industria y Competitividad (MINECO, Spain), and by Programme GEOMATERIALES 2-CM (S2013/MIT_2914) from the Community of Madrid. Authors also acknowledge the support by the Spanish Network TechnoHeritage, the Museo Arqueológico Nacional and Museo de Escultura de Leganés.

References

1. Cano E, Lafuente D, Bastidas DM (2010) Use of EIS for the evaluation of the protective properties of coatings for metallic cultural heritage: a review. J Solid State Electrochem 14:381–391
2. Letardi P, Beccaria A, Marabelli M, D'Ercoli G (1998) Application of electrochemical impedance measurements as a tool for the characterization of the conservation and protection state of bronze works of art. In: Ashton J, Hallam D (eds) Metal 98. International conference on metal conservation James & James, Draguignan-Figanières (France), pp 303–308
3. Hallam D, Thurrowgood A, Otieno-Alego V, Creagh D (2004) An EIS method for assessing thin oil films used in museums. In: Ashton J, Hallam D (eds) Metal 04: proceedings of the international conference on metals conservation, Canberra, Australia, pp 388–399
4. Dowsett M, Adriaens A, Schotte B, Jones G, Bouchenoire L (2007) Real time spectroelectrochemical growth and corrosion resistance monitoring of lead carboxylate coatings in an environmental cell (eCell). In: Degrigny C, van Langh R, Joosten I, Ankersmit B (eds) Metal 07: interim meeting of the ICOM-CC Metal WG, vol 3. Rijksmuseum, Amsterdam, Netherlands, pp 26–31
5. Letardi P (2013) Electrochemical measurements in the conservation of metallic heritage artefacts: an overview. In: Dillmann P, Watkinson D, Angelini E, Adriaens A (eds) Corrosion and conservation of cultural heritage metallic artefacts, EFC Series. Woodhead Publishing, Sawston, pp 126–148
6. Price C, Hallam D, Heath G, Creagh D, Ashton J (1995) An electrochemical study of waxes for bronze sculpture. In: MacLeod ID, Pennec SL, Robbiola L (eds) Metal 95. International conference on metal conservation. James & James, Semur-en-Auxois (France), pp 233–241
7. Cano E, Bastidas DM, Argyropoulos V, Fajardo S, Siatou A, Bastidas JM, Degrigny C (2010) Electrochemical characterization of organic coatings for protection of historic steel artefacts. J Solid State Electrochem 14:453–463
8. Angelini E, Carullo A, Corbellini S, Ferraris F, Gallone V, Grassini S, Parvis M, Vallan A (2006) Handheld-impedance-measurement system with seven-decade capability and potentiostatic function. IEEE Trans Instrum Meas 55:436–441
9. Elsener B, Alter M, Lombardo T, Ledergerber M, Wörle M, Cocco F, Fantauzzi M, Palomba S, Rossi A (2016) A non-destructive in-situ approach to monitor corrosion inside historical brass wind instruments. Microchem J 124:757–764
10. Clare TL, England A, Swartz N, Hosbein K (2013) Onsite electrochemical monitoring method for early detection of coating failure. In: Hyslop E, Gonzalez V, Troalen L, Wilson L (eds) Metal 2013: proceedings of the interim meeting of the ICOM-CC metal working group, Edinburgh, pp 89–94
11. Ramirez Barat B, Cano E (2015) The use of agar gelled electrolyte for in situ electrochemical measurements on metallic cultural heritage. Electrochimica Acta 182:751–762
12. Gulotta D, Mariani B, Guerrini E, Trasatti S, Letardi P, Rosetti L, Toniolo L, Goidanich S (2017) Mi Fuma il Cervello self-portrait series of Alighiero Boetti: evaluation of a conservation and maintenance strategy based on sacrificial coatings. Heritage Science, 5:19
13. Letardi P (2004) Laboratory and field tests on patinas and protective coating systems for outdoor bronze monuments. In: Ashton J, Hallam D (eds) Metal 04: proceedings of the international conference on metals conservation, Canberra, Australia, pp 379–387
14. Letardi P, Salvadori B, Galeotti M, Cagnini A, Porcinai S, Barbone AS, Sansonetti A (2016) An in situ multi-analytical approach in the restoration of bronze artefacts. Microchem J 125:151–158
15. Sansonetti A, Colella M, Letardi P, Salvadori B, Striova J (2015) Laser cleaning of a nineteenth-century bronze sculpture: In situ multi-analytical evaluation. Stud Conserv 60: S28–S33
16. Corbellini S, Parvis M, Grassini S (2012) Noninvasive solution for electrochemical impedance spectroscopy on metallic works of art. IEEE Trans Instrum Meas 61:1193–1200

17. Grassini S, Angelini E, Parvis M, Bouchar M, Dillmann P, Neff D (2013) An in situ corrosion study of Middle Ages wrought iron bar chains in the Amiens Cathedral. Appl Phys A Mater Sci Process 113:971–979
18. England AH, Clare TL (2014) Synthesis and characterization of flexible hydrogel electrodes for electrochemical impedance measurements of protective coatings on metal sculptures. Electroanalysis 26:1059–1067
19. Cano E, Crespo A, Lafuente D, Ramirez Barat B (2014) A novel gel polymer electrolyte cell for in-situ application of corrosion electrochemical techniques. Electrochem Commun 41:16–19
20. Letardi P, Ramirez Barat B, Cano E (2017) Analysis of the influence of the electrochemical cell setup for corrosion measurements on metallic cultural heritage. In: European Corrosion Congress - EUROCORR, Prague
21. Ramirez Barat B, Cano E, Letardi P (2018) Advances in the design of a gel-cell electrochemical sensor for corrosion measurements on metallic cultural heritage. Sens Actuators B Chem 261:572–580
22. Ramirez Barat B, Cano Díaz E (2015) In situ assessment of protective coatings for metallic cultural heritage using electrochemical impedance spectroscopy. Ge-Conservacion 2015:6–13
23. Ramirez Barat B, Crespo A, García E, Díaz S, Cano E (2017) An EIS study of the conservation treatment of the bronze sphinxes at the Museo Arqueológico Nacional (Madrid). J Cult Heritage 24:93–99
24. Ramirez Barat B, Palomar T, Garcia B, de la Fuente D, Cano E (2016) Composition and protective properties of weathering steel artificial patinas for the conservation of contemporary outdoor sculpture. In: 9th interim meeting of the ICOM-CC metals working group. METAL2016, New Delhi, India
25. Crespo A, Ramirez Barat B, Cano E (2016) Artificial patinas in contemporary weathering steel sculpture. In: 5th International Conference YOuth in COnservation of CUltural Heritage —YOCOCU 2016, Madrid
26. Crespo A, Ramirez Barat B, Diaz I, Cano E (2017) Assessment of the protective properties of patinas on contemporary sculpture made out of weathering steel. In: J Bridgland (ed) ICOM-CC 18th Triennial conference copenhagen
27. Ramirez Barat B, Crespo A, Cano E (2017) In situ evaluation of outdoor sculpture with a gel polymer electrolyte cell. In: Mosquera MJ, Almoraima ML (eds) Conserving Cultural Heritage. CRC Press/Balkema, London, pp 83–86

Chapter 3
Multispectral IR Reflectography for Painting Analysis

Raffaella Fontana, Marco Barucci, Alice Dal Fovo, Enrico Pampaloni, Marco Raffaelli and Jana Striova

1 InfraRed Reflectography (IRR)

1.1 Fundamentals of IRR

InfraRed Reflectography (IRR) is a well-established diagnostic technique for the analysis of paintings that consists in irradiating the painting with an IR source and in detecting the back-scattered radiation in a wide spectral band with a suitable device [1, 2]. Thanks to the transparency properties of most pigments to the infrared radiation, it allows the visualization of features underneath the painting's surface (Fig. 1), such as the underdrawing (a preliminary sketch made by the painter on a preparation ground, prior to painting), the *pentimenti* (an underlying image in a painting providing evidence of revision by the artist), subsequent retouchings or repaintings (generally speaking, foreign materials added at a later stage for modifying the artwork's painting or structure), restoration intervention (the process of re-establishing the artwork legibility through selective removal of patina, consolidation of ancient materials and eventual reconstruction of missing pieces). The visibility of the underlying features depends on the paint layers' thickness and chemical composition, as well as on the chemical composition of the materials that form both the underdrawing and the preparation. If the preparation layer is characterized by a high reflectivity in the IR spectral range (a typical case is chalk-and-gypsum-based preparation) and the underdrawing is carbon-based, the visibility of the preparatory sketch is evident, whereas it decreases in case of iron-gallic inks or sanguine. Paints' transparency generally increases with the wavelength of the radiation used, reaching its maximum for most pigments around 1.7 micron.

R. Fontana (✉) · M. Barucci · A. Dal Fovo · E. Pampaloni · M. Raffaelli · J. Striova
CNR-INO, National Institute of Optics - National Research Council,
Heritage Science Group, Largo E. Fermi 6, 50125 Florence, Italy
e-mail: raffaella.fontana@ino.it

D. M. Bastidas and E. Cano (eds.), *Advanced Characterization Techniques, Diagnostic Tools and Evaluation Methods in Heritage Science*,
https://doi.org/10.1007/978-3-319-75316-4_3

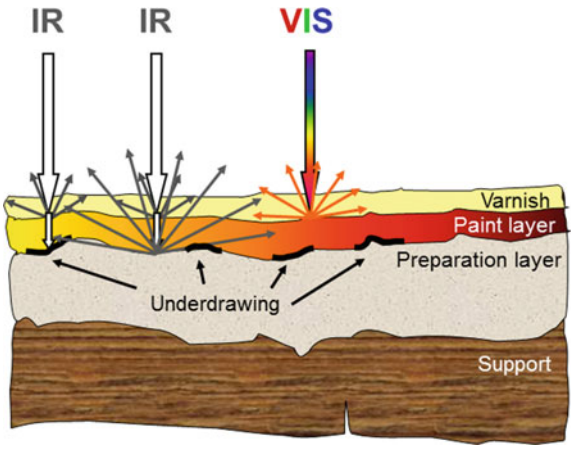

Fig. 1 Interaction scheme of visible and infrared radiation with a painting, sketched as a multilayer system

1.2 Traditional Devices for IRR

IR reflectography dates back to the '60s, and is based upon the fundamental work of Van Asperen de Boer [1, 2], who laid the theoretical and experimental bases for this technique, and introduced the use of PbS Vidicon cameras. Traditionally performed by means of image detectors like CCD or Vidicon cameras [3–7], IR reflectography has evolved with the first scanning device in the '90s [8]. The main advantages of imaging sensors are their ease of use, portability and fastness. On the other hand, output images are affected by geometrical distortion, due to the camera lens, requiring post processing. A rigorous calibration procedure is also necessary, to correct the non-uniform surface lighting [9, 10]. Vidicon has a good spectral sensitivity (up to 2.2 micron for PbO–PbS cameras) but its scarce light sensitivity demands for an intense illumination, which can induce a detrimental warming of the painting surface. Moreover, images are characterized by a very poor contrast due to the limited number (some tens) of grey levels, and are brighter in the centre and darker on the borders due to the non-uniform sensitivity of the detector's area. To obtain a high spatial resolution, the measured area must be very small (e.g. 10×10 cm^2 to have a resolution of 4 pixel/mm, needed to resolve the finest under-drawing lines). The reproduction of a large panel requires, thus, the collection of several images (more than 100 for 1 m^2) that are successively combined in a mosaic. Because of the above mentioned intrinsic characteristics, the resulting reflectogram generally appears tiled, in many cases even after equalization [11]. The use of low-cost CCD detectors (Si based) does not meaningfully improve the quality of the reflectogram: they have higher intensity resolution and more uniform response than Vidicon. Nevertheless, they have a sensitivity limited to 1.1 micron, as a consequence the acquired images have a very scarce informative content. Special highly-priced CCD devices (InGaAs or PtSi arrays) can strongly improve the visibility of the underlying features, due to the extended spectral coverage.

However, a great number of images must still be collected to reproduce a large painting with high spatial resolution. The mosaic realisation requests long calibration and clean-up operation of the acquired images, owing to the non-uniform lighting condition and the misalignment/distortion of collected images.

1.3 Scanning Device for IRR

High-resolution scanning reflectography was developed at the National Institute of Optics (INO, the actual INO-CNR), in Florence, at the beginning of the '90s. At that time, an innovative scanning device for imaging in the infrared spectral range was built, able to acquire a reflectogram with spectral sensitivity and tonal dynamics up-to-now unobtainable by any of the techniques traditionally used for IRR [8]. Besides that, single point detection together with simultaneous motion of in-built light sources, minimizes surface heating and bypasses the problem of uniform illumination. In the late '90s, its performances were improved and the scanner could simultaneously acquire the IR reflectogram and three R, G, B images that properly combined produced the colour image of a painting, which can be perfectly superimposed one on the other [12]. The point-by-point comparison between the reflectogram and the colour image of the painting, along with digital processing of the recorded images, such as IR false colour imaging [13], opened new possibilities in the IRR analysis.

2 Scanning Multispectral InfraRed Reflectography (SMIRR)

2.1 Concepts of SMIRR

Multispectral imaging is widely used in remote sensing applications, such as satellite or radar imaging, mainly for agriculture, forestry and weather mapping. It has recently gained importance in the field of artworks' conservation, in particular in the IR spectral region, having proved useful in analysing ancient paintings because of the varied reflectance of pigments over this spectral region.

Traditional reflectography, performed by acquiring the IR image in a single large band (wide-band modality) corresponding to the spectral range of the device, is improved by the multiband option, which allows the choice of the most effective wavelength for the specific case. Multispectral imaging in the IR allows the simultaneous collection of both spectral and spatial information enlarging, thus, the perspectives of IRR to new applications for the study of artists' materials. It consists in irradiating the painting surface with a broadband source and collecting the backscattered radiation within narrow spectral IR bands [14, 15].

2.2 Current Devices for Multispectral IRR

A variety of IR multispectral devices have been implemented, based on different imaging detectors with either filtering or dispersing element (Fig. 2) for waveband selection [16–21]. The output is a set of monochromatic images stacked as a sequence of acquisitions.

Systems based on imaging sensor suffer from pixel-to-pixel biases, lens distortion, non-uniform illumination and require proper calibration/correction procedures. Detector size limits the spatial resolution because of mosaicking. As previously said, multispectral devices currently used in conservation have limited spectral range, mainly due to the high cost of the available technology to cover an extended IR spectral range. Moreover, such systems are affected by systematic errors such as spectral channels blurring, chromatic aberration due to the objective lens, which affects the reliability of spectral data and require optical calibration. When filters are tuned by mechanical devices, e.g. rotating wheels, the spectral image set is difficult to register [22–24].

2.3 Scanner for Multispectral IRR

The upgrade of the wide-band scanner to the multispectral modality was carried out by the INO's Cultural Heritage Group in five years of the European project EuArtech (Access, Research and Technology for the Conservation of the European Cultural Heritage, 2004–2009) [25]. This scanning device (Fig. 3) was revolutionary in the field of infrared reflectography because it allowed to simultaneously acquire a set of 14 high resolution images at different wavelengths in the spectral IR region from 800 to 2300 nm [26–29]. Over such an extended spectral range chromatic aberration causes defocussing among the spectral images: a catoptric lens was then used to obtain a set of monochromatic images perfectly focused and superimposing. The instrument core is still single point detection performed by a purposely-designed fiber bundle whose ends are properly filtered. In the recent years, the scanner underwent further improvements consisting in the addition of

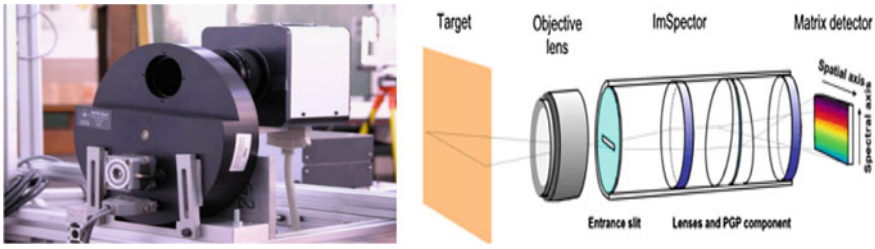

Fig. 2 Multispectral device based on (left) filter wheel and (right) dispersive system

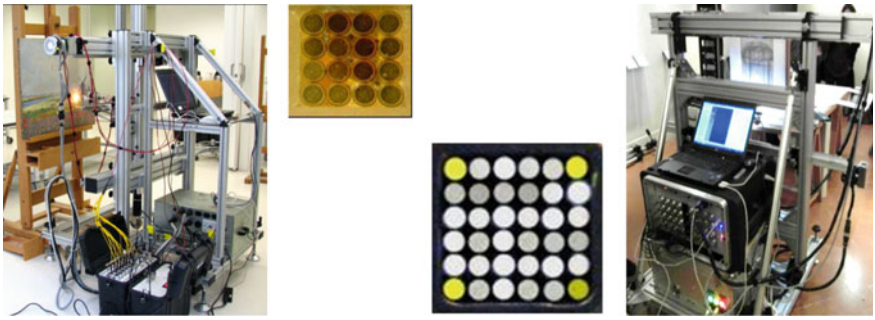

Fig. 3 Multispectral scanner for IR reflectography: version with (left) 16-fiber and (right) 36-fiber bundle; (middle) corresponding bundle sections, as seen at the optical microscope

both an autofocus system to keep the optical head at focus while scanning, and the R, G, B channels to provide the colour image perfectly superimposing with the reflectograms. In its last version [30], the instrument acquires 16 bands in the visible and 16 bands in the IR spectral range, this latter extended up to 2500 nm.

An XY scanning system moves an optical head that both illuminates the painting and collects the backscattered radiation carried to the detectors by means of a fiber bundle. The lighting system is composed of two low-voltage halogen lamps and two white LEDs (5° beam divergence, according to CIE suggestions for the 45°/0° configuration) and the irradiated area is about 5 cm^2 at the working distance of about 12 cm. The collecting optics is a catoptric system (depending on the scanner version, made of two faced spherical or two off-axis parabolic mirrors) working in a 2f–2f configuration to have a unitary magnification factor. The radiation scattered from the measured point on the painting is imaged on the fiber bundle, made of 16 or 36 fibers depending on the instrument version, assembled in square array (core/clad diameter 200/250 μm). The detection unit is composed of 3 Si and 13 InGaAs photodiodes (16-fiber bundle) or 19 Si and 13 InGaAs photodiodes (36-fiber bundle). Each detector is equipped with an interferential filter whose FWHM ranges from 50 to 100 micron in the IR and from 20 to 30 in the VIS range. The device allows continuous measurement of an area up to 1 m^2 with a sampling step of 250 micron, lasting about 3 h at the maximum acquisition rate of 2 kHz. In the acquisition phase our scanner is time-consuming compared with devices based on imaging sensors, but this time loss is recovered a posteriori because image data do not require any post-processing, being aberration-free and hardware registered.

Channels equalization was performed with certified standards with known reflectance. Raw 16-bit IR images are reconstructed point-by-point by associating to each pixel on the image plane the spectral reflectance factor $R(\lambda)$. The latter is computed based on both the intensity reflected by the sampled point on the painting surface I_{sample} and the in-scene reflectance standard I_{ref} with the formula:

$$R(\lambda) = \rho(\lambda)\frac{I_{sample} - I_{dark}}{I_{ref} - I_{dark}} \quad (1)$$

where $\rho(\lambda)$ is the certified value for the reflectance standard, I_{dark} is an image with closed optics and I_{ref} is acquired at the beginning of each scanning session.

3 Applications and Results

3.1 Multispectral Data Processing

The stack of spectral images provides information in both the spectral and spatial domain (Fig. 4): the reflectance at each point of the multispectral image cube provides the spectrum of the pixel (IR spectrometry), whereas the slices correspond to images at different wavelength (multi-IR reflectography).

The monochromatic images can be analysed separately, scrolling the λ-planes to study the transparency properties of the different coloured areas, as well as jointly, applying mathematical algorithms to enhance the visualization of features varying with wavelength. In particular, pairs of single-wavelength images were jointly processed to compute pixel-by-pixel subtraction and ratio to highlight changes in the reflectance of pigments from one wavelength to another. Standard IR false colour as well as colour composite images were elaborated with either single band or difference/ratio images in both trichromatic RGB and tetra-chromatic CMYK spaces to highlight the presence of retouching/integrations and to visualize the information from more than one channel simultaneously. Statistical methods such

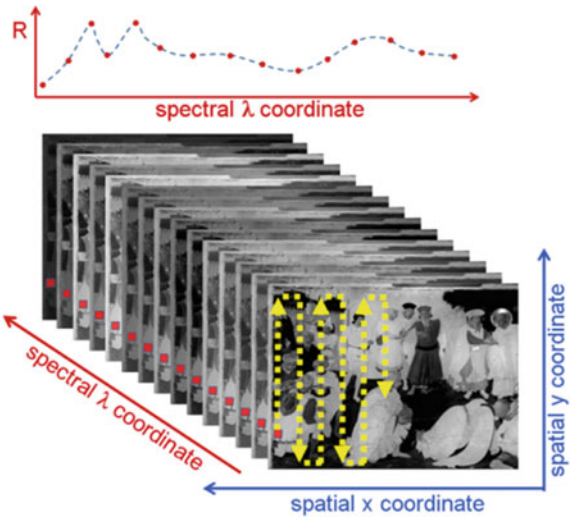

Fig. 4 Scheme of spectral and spatial data output from multispectral measurement

as Principal Component Analysis (PCA) and Non-negative Matrix Factorization (NMF) were also applied either to concentrate significant features into a few representative images or to enhance the information content. It is worth noting that any operation with different bands is possible directly with the raw data thanks to the superimposing property and aberration-free characteristics of our images that do not require either registration or correction. This approach has proven to be easy to use as basic image processing can be performed also with commercial software. Moreover, maintaining a visual correspondence with the painting eases the interpretation of the results.

3.2 *Examples of Multispectral Applications and Analysis*

Many measurement campaigns on artworks were carried out both at the INO's Optical Metrology Laboratory hosted at the Opificio delle Pietre Dure (OPD) in Florence, one of the largest restoration facilities in Europe, and at Italian and foreign museums all over Europe. In fact, the scanner is part of the MOLAB (MObile LABoratory), a facility that can be accessed by the scientific and the conservation community, after evaluation from a peer review panel, in the framework of the national E-RIHS.it [31] and IPERION CH EU-projects [32]. The results presented herein are intended to give an overview of both the applications of multispectral IR reflectography, with emphasis on the advantages over conventional reflectography, and the usefulness of the different analyses to evidence the potential of the multispectral approach.

Multispectral imaging may enable the analysis of features not detectable in the wide-band reflectography: according to the case study, it allows the choice of the most effective IR bands to enhance the presence of retouches/repaintings or, more generally, areas of painting materials different from the original. Moreover, the transparency properties of the pigments with wavelength can be analysed, together with the visibility of the drawing below them.

The potential of the multispectral approach is evidenced in Fig. 5 where the painting *Madonna with Child* by Cimabue is presented. Wide-band reflectography is compared with a few spectral images at different wavelengths. The two light spots on the Child's forehead, probably retouches, are clearly visible both in the wide-band reflectography and in the spectral images up to 1300 nm, whereas increasing wavelength beyond 1700 nm reveals details otherwise not visible such as the golden leaf that is marked out as a well-defined white area above the eye.

Depending on the case study, entering IR, i.e. increasing wavelength, can be most revealing or least revealing. The paintings in Figs. 6 and 7 are testimony of these two instances, respectively. For increasing λ, the Madonna's mantle in the painting by Giovanni di Paolo (Fig. 6) displays details not otherwise visible, whereas the *Adorazione dei pastori* by Beato Angelico (Fig. 7) shows nearly no difference.

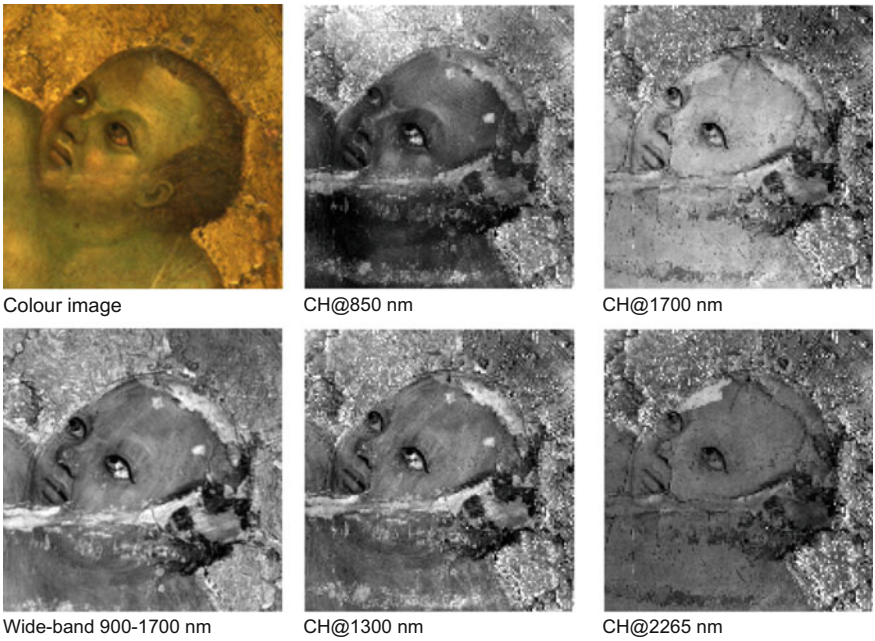

Fig. 5 *Madonna with Child* (Cimabue), detail of the Child's head. The wide-band reflectogram obtained with the very first scanner prototype is compared with the multispectral scanner's output at different wavelengths (CH@ = channel centered at)

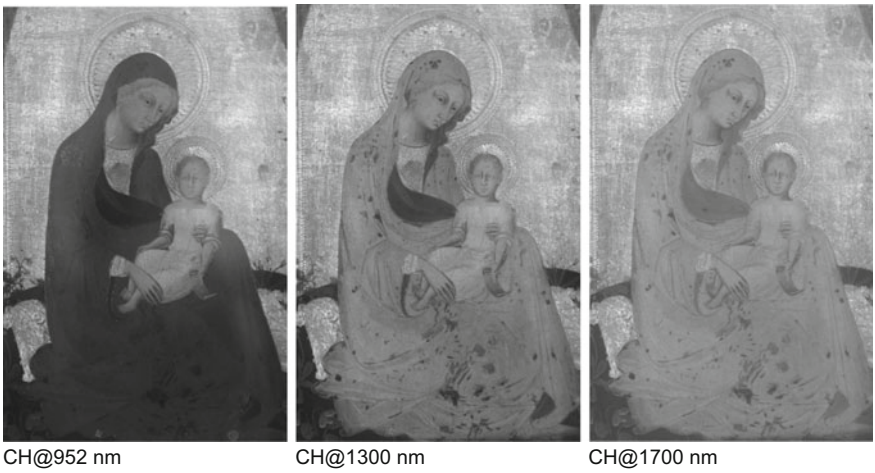

Fig. 6 Reflectograms (CH@ = channel centered at) of the *Madonna with Child* by Giovanni di Paolo, Harvard Center for Renaissance Studies, Villa I Tatti, Florence (IT)

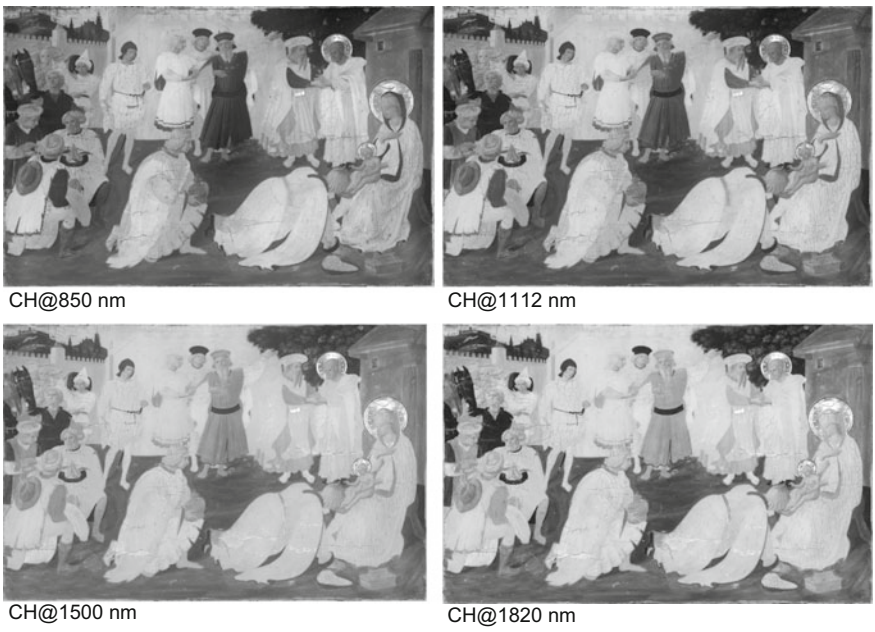

Fig. 7 Reflectograms (CH@ = channel centered at) of the Beato Angelico's *Adorazione dei pastori*, Tabernacolo dei Linaioli, Museo di San Marco, Florence (IT)

Evidence of the importance of the extended spectral range with respect to the current multispectral devices is given in Fig. 8. An architectural moulding, hidden under the dark background, becomes discernible at 1300 nm and it is clearly distinguished from 1700 nm, but the spolvero technique becomes evident at 2235 nm. None of these features would be detectable with standard devices such as CCD camera, with spectral sensitivity up to 1050–1100 nm (Fig. 9).

False colour representation with either single channels or difference/ratio images was used to differentiate areas that are then visualized in an effective way (Fig. 10).

PCA was profitably applied to a panel painting by Cosmè Tura: score images were extracted and analysed separately as well as jointly. The first score image T1 contains the same information as the wide-band reflectography. The following three score images T2, T3, T4, combined in a false colour representation, improve the detection of details as shown in Fig. 11.

As mentioned above, spectral segmentation allows the acquisition of pixel-by-pixel reflectance information that is closely related to the visual appearance of the reflectograms at the different wavelengths. In Fig. 12 an example of the study of pigment transparency is shown. In order to examine the features varying with wavelengths (pigment transparency and underdrawing visibility), the spectrum of cobalt blue, as measured with both FORS and our VIS-IR scanner, is presented together with the monochromatic images corresponding to the most representative wavelengths.

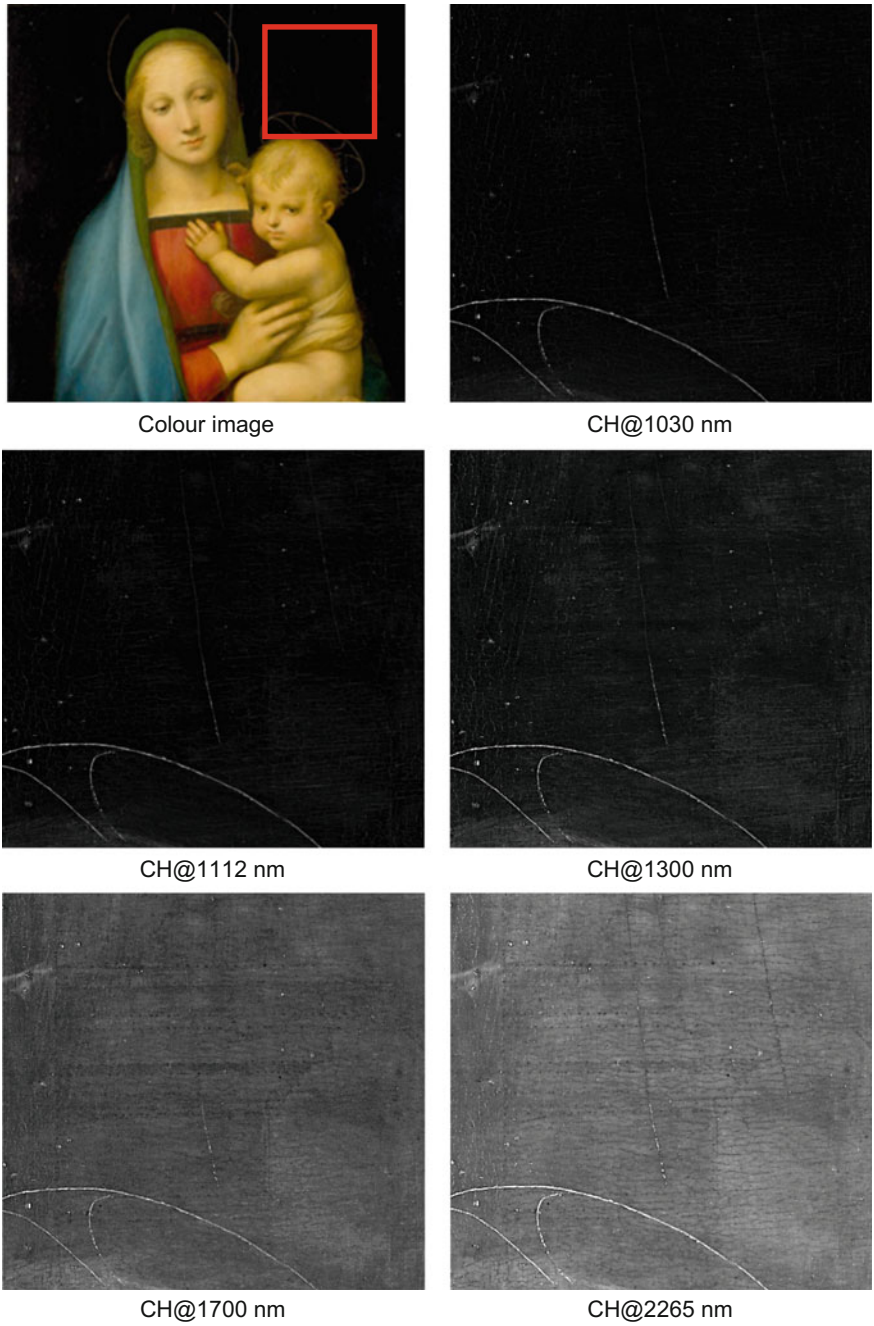

Fig. 8 Colour and reflectographic images (CH@ = channel centered at) of Raffaello's *Madonna del Granduca*, Galleria Palatina, Florence (IT)

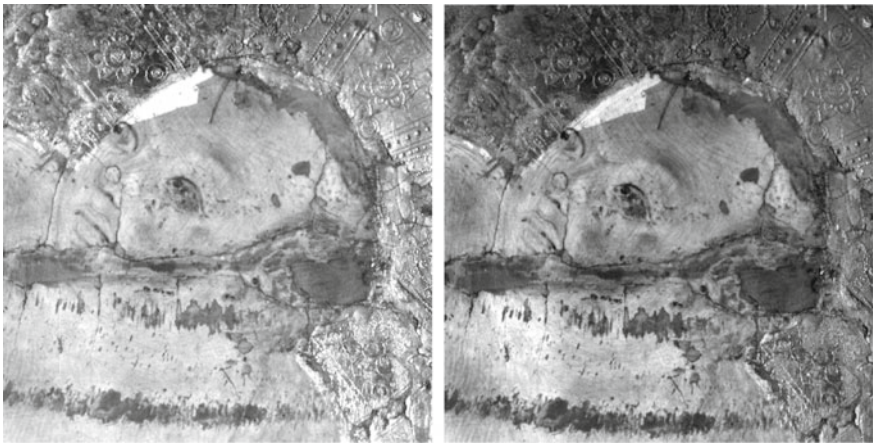

Fig. 9 Difference and ratio of the reflectographic images acquired on the *Madonna with Child* (Cimabue) painting (CH@ = channel centered at), detail of the Child's head. Florence (IT)

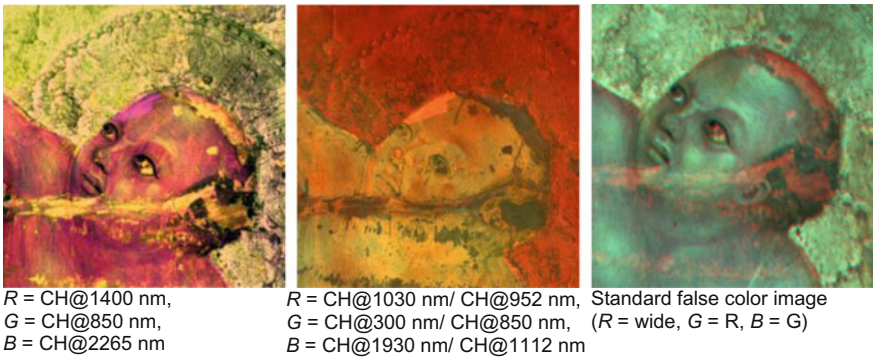

Fig. 10 Colour composite images with (left) IR bands; (middle) ratio images; (right) standard IR-false colour image of a detail of the Child's head (Madonna with Child by Cimabue, Florence, IT). (CH@ = channel centered at)

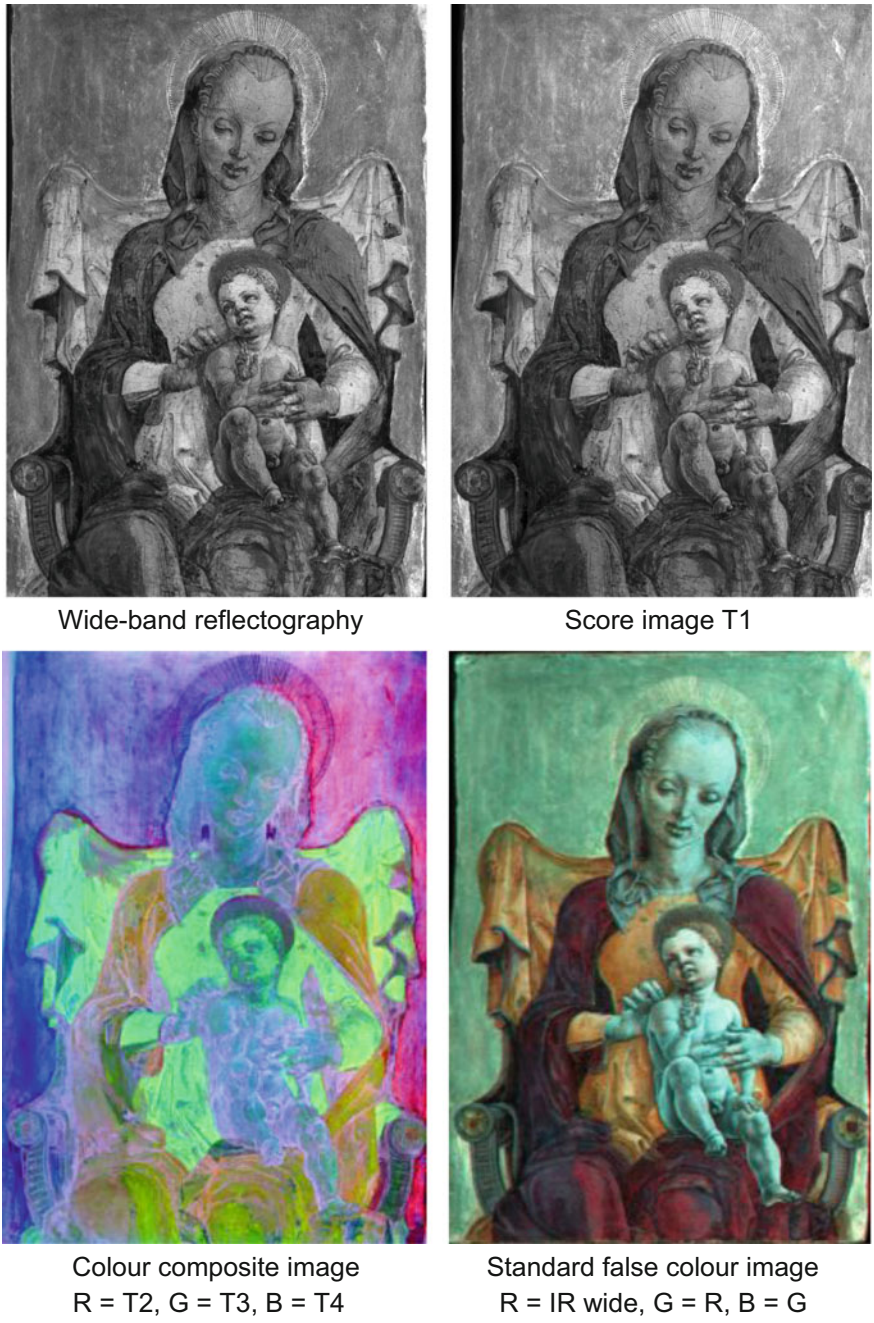

Fig. 11 Virgin with child by Cosmè Tura, Galleria dell'Accademia Carrara, Bergamo

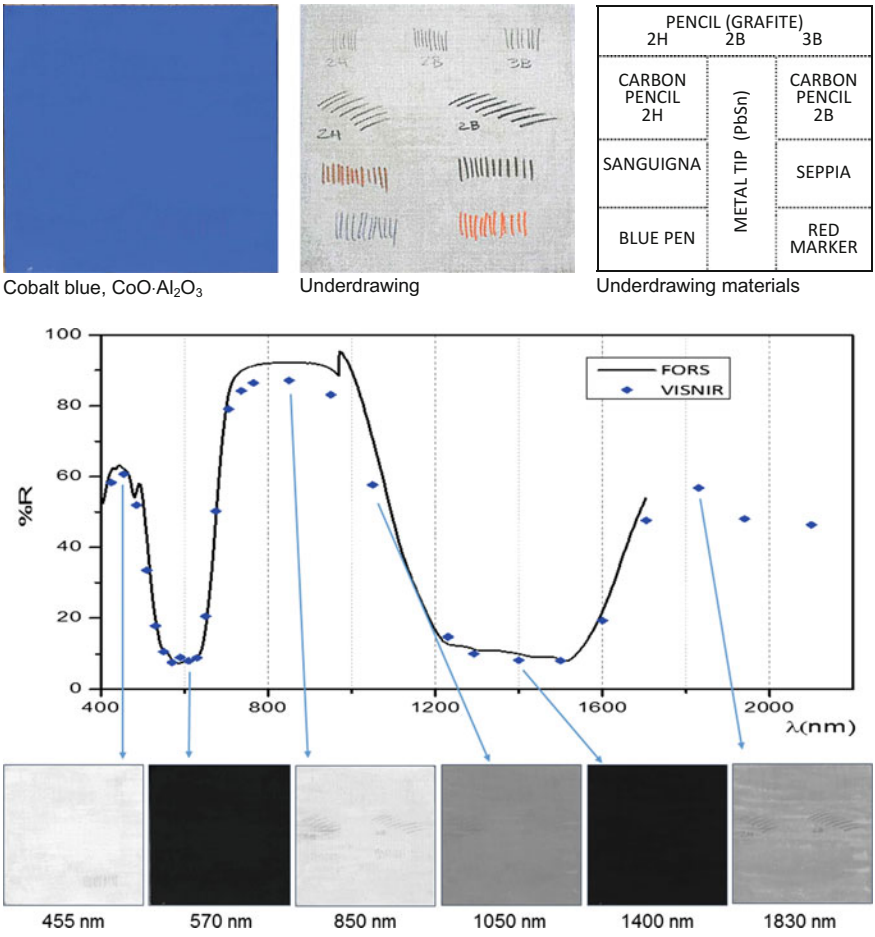

Fig. 12 (top) Sample of cobalt blue laid on underdrawings of different materials, (middle) corresponding spectrum as measured by multispectral VIS-IR scanner (blue diamonds) and FORS (black full line) and (bottom) related spectral images

4 Conclusions

Scanning multispectral infrared reflectography is presented herein. The output of the technology is a stack of monochromatic images, one for each selected wavelength, which can be analysed separately as well as jointly. Advantages over the traditional wide-band reflectography are presented by showing a few examples of applications on ancient paintings. The innovative multispectral scanner developed by the Cultural Heritage Group of INO-CNR allows for a straightforward processing of the spectral planes, without any image correction.

Acknowledgements The authors would like to thank Dr. Cecilia Frosinini and Roberto Bellucci for the fruitful discussions necessary for a proper interpretation of the results. We would also thank Marta Florez Igual for preparing the cobalt blue sample presented herein.

This research has been co-financed by H2020 IPERION CH project (contract number: 654028).

References

1. van Asperen de Boer JRJ (1968) Infrared reflectography: a method for the examination of paintings. Appl Opt, 7(9):1711–1714
2. Van Asperen de Boer JRJ (1969) Reflectography of paintings using an infra-red vidicon television system. Stud Conserv, 14:96–118
3. Walmsley E, Fletcher C, Delaney J (1992) Evaluation of system performance of nearinfrared imaging devices. Stud Conserv 37:120–131
4. Saunders D, Billinge R, Cupitt J, Atkinson N, Liang H (2006) A new camera for high resolution infrared imaging of works of art. Stud Conserv 51:277–290
5. Consolandi L, Bertani D (2007) A prototype for high resolution infrared reflectography of paintings. Infrared Phys Technol 49(3):239–242
6. Falco CM (2009) Invited article: high resolution digital camera for infrared reflectography. Rev Sci Instrum, 80, 071301, 1–9
7. Walmsley E, Metzger C, Delaney JK, Fletcher C (1994) Improved visualization of underdrawings with solid-state detectors operating in the infrared. Stud Conserv 39:217–231
8. Bertani D, Cetica M, Poggi P, Puccioni G, Buzzegoli E, Kunzelman D, Cecchi S (1990) A scanning device for infrared reflectography. Stud Conserv 35:113–117
9. Gargano M, Ludwig N, Poldi G (2007) A new methodology for comparing IR reflectographic systems. Infrared Phys Technol 49(3):249–253
10. Daffara C, Gambino MC, Pezzati L (2008) Performance analysis of imaging systems for NIR reflectography. In: Proceedings of the 2nd international topical meeting on optical sensing and artificial vision (OSAV 2008), St. Petersburg, Russia, May 12–15, 2008; International Commission for Optics: Boca Raton, FL, pp 307–314
11. Saunders D, Cupitt J (1993) Image processing at the national gallery: the VASARI project. Nat Gallery Bull 14:72–85
12. Fontana R, Gambino MC, Greco M, Marras L, Materazzi M, Pampaloni E, Pezzati L, Poggi P (2003) New high resolution IR-colour reflectography scanner for painting diagnosis. Proc SPIE 5146:108–115
13. Moon T, Schilling MR et al (1992) A note on the use of false-color infrared photography in conservation. Stud Conserv 37:42–52
14. Mansfield JR, Attas M, Majzels C, Cloutis E, Collins C, Mantsch HH (2002) Near infrared spectroscopic reflectance imaging: a new tool in art conservation. Vib Spectrosc 28:59–66
15. Delaney JK, Zeibel JG, Thoury M, Littleton R, Morales KM, Palmer M, de la Rie ER (2009) Visible and infrared reflectance imaging spectroscopy of paintings: pigment mapping and improved infrared reflectography. Proc SPIE 7391(739103):1–8
16. Fischer C, Kakoulli I (2006) Multispectral and hyperspectral imaging technologies in conservation: current research and potential applications. Rev Conserv 7:3–16
17. Baronti S, Casini A, Lotti F, Porcinai S (1998) Multispectral imaging system for the mapping of pigments in works of art by use of principal-component analysis. Appl Opt 37(8): 1299–1309
18. Casini A, Lotti F, Picollo M, Stefani L, Buzzegoli E (1999) Image spectroscopy mapping technique for non-invasive analysis of paintings. Stud Conserv 44:39–48

19. Delaney JK, Walmsley E, Berrie BH, Fletcher CF (2005) Multispectral imaging of paintings in the infrared to detect and map blue pigments. In Scientific examination of art: modern techniques in conservation and analysis; National Academies Press, Washington, DC, pp 120–136
20. Balas C, Papadakis V, Papadakis N, Papadakis A, Vazgiouraki E, Themelis G (2003) A novel hyper-spectral imaging apparatus for the non-destructive analysis of objects of artistic and historic value. J Cult Herit 4(1):330–337
21. Liang H, Saunders D, Cupitt J (2005) A new multispectral imaging system for examining paintings. J Imaging Sci Technol 49(6):551–562
22. Mansouri A, Marzani FS, Hardeberg JY, Gouton P (2005) Optical calibration of a multispectral imaging system based on interference filters. Opt Eng, 44(2), 27004, 1–12
23. Gat N (2000) Imaging spectroscopy using tunable filters: a review. Proc SPIE 4056:50–64
24. Corsini M, Bartolini F, Cappellini V (2001) Mosaicing for high resolution acquisition of paintings. In: Proceedings of the 7th international conference on virtual systems and multimedia (VSM'01), Berkley, CA, 25–27 Oct 2001; IEEE Computer Society, Washington, DC, pp 39–48
25. EU-ARTECH. Access research and technology for the conservation of the European cultural heritage, European Project 2004–2009, Contract no. RII3-CT-2004-506171, www.eu-artech.org
26. Fontana F, Bencini D, Carcagni P, Greco M, Mastroianni M, Materazzi M, Pampaloni E, Pezzati L (2007) Multi-spectral IR reflectography. Proc SPIE 6618(661816):1–12
27. Bonifazzi C, Carcagni P, Fontana F, Greco M, Mastroianni M, Materazzi M, Pampaloni E, Pezzati L, Bencini D (2008) A scanning device for VIS-NIR multispectral imaging of paintings. J Opt A Pure Appl Opt, 10, 064011, 1–9
28. Daffara C, Pampaloni E, Pezzati L, Barucci M, Fontana R (2010) Scanning multispectral IR reflectography SMIRR: an advanced tool for art diagnostics. Acc Chem Res 43(6):847–856
29. Daffara C, Fontana R (2011) Multispectral infrared reflectography to differentiate features in paintings. Microsc Microanal 17(05):691–695
30. Fontana R, Barucci M, Pampaloni E, Striova J, Pezzati L (2014) From Leonardo to Raffaello: insights by Vis-IR reflectography. In: Interpretation of fine art's analyses in diverse contexts, Acta Artis Academica, pp 15–26
31. http://www.e-rihs.it
32. http://www.iperionch.eu/

Chapter 4
Optical Coherence Tomography (OCT) for Examination of Artworks

Magdalena Iwanicka, Marcin Sylwestrzak and Piotr Targowski

1 Introduction and Apparatus

1.1 Fundamentals of OCT Technique

Optical coherence tomography (OCT) is an optical interferometric technique originating from diagnostic medicine at which it is a well-established method [1, 2]. Relatively early after its invention OCT was used for the examination of artworks: this application is reported in the literature since 2004 [3]. It uses light of very low temporal coherence (broad spectrum) in order to provide high in-depth resolution and simultaneously of high spatial coherence to ensure high sensitivity. There are many configurations in use: in the most common one a Michelson interferometer is utilised with a broadband infrared light split between an object beam and a reference beam. The narrow object beam penetrates the examined artwork and is reflected or scattered at its internal features. After returning to the instrument it is superimposed with the reference beam, and thus the interference signal is obtained. It may be detected spectrally (Fourier domain systems with the constant length of the reference arm of the interferometer) or temporarily at the single detector (time domain system with the variable length of the reference arm). A list of applications of optical coherence tomography to the investigation of various cultural heritage objects can be found elsewhere [3–5].

For examination of the objects presented in this study we have used the system designed and built especially for the examination of cultural heritage objects under 7FP Charisma project at N. Copernicus University in Torun, Poland. It is a Fourier

M. Iwanicka (✉)
Faculty of Fine Arts, Nicolaus Copernicus University, Torun, Poland
e-mail: magiwani@gmail.com

M. Sylwestrzak · P. Targowski
Faculty of Physics, Astronomy and Informatics, Nicolaus Copernicus University, Torun, Poland

D. M. Bastidas and E. Cano (eds.), *Advanced Characterization Techniques, Diagnostic Tools and Evaluation Methods in Heritage Science*,
https://doi.org/10.1007/978-3-319-75316-4_4

domain OCT instrument with a spectrograph used as a detector. As a light source the instrument utilises superluminescent multi-diode emitting in band 770–970 nm providing the beam intensity up to 800 μW at object. This irradiation level is considered non-invasive even for light-sensitive materials. In practice, the ability to differentiate thin layers is denoted by the axial (in-depth) resolution, which equals ca 2.2 μm (in material of refractive index equal to about 1.5). Lateral resolution (the ability to differentiate between structures occurring close to each other in lateral plane) is about 13 μm. These features make our instrument especially well-suited for the examination of thin-layered structures, such as easel paintings. The axial imaging range is 1.7 mm and sensitivity 98 dB. The distance to the examined object from the most protruding element of the device is 43 mm and the structural information from the area up to 17 × 17 mm^2 may be acquired in one measurement. Data collection time for one 2D cross-section (B-scan) is 0.15 s. Two standard video cameras enable the precise documentation of the position of examined area at the object.

Nowadays, the requirement for non-invasiveness of examination techniques (not interfering with the substance of the artwork in any way) is an important issue in conservation science. There have been no systematic studies on this matter regarding OCT, although it may be assumed that the intensity of the probing beam proclaimed safe for the human retina (according to the American National Standards Institute regulations [6]) may be considered safe for any kind of artwork.

Additionally, OCT provides better representativeness of results (in comparison to traditional, invasive sampling methods) due to the fast data collection and no need for any special object preparation (Fig. 1). Usually sampling is permitted only to spots where some damage has occurred previously or, in case of easel paintings, areas of lesser visual importance. OCT provides structural information from the spots which cannot be sampled, and, in cases when sampling is still required, helps to limit it to few representative spots.

Unfortunately, the diversity of objects being within a circle of interest is in case of OCT limited by the properties of the materials constituting the artwork. The major limitation of what may be examined with OCT lies in the transparency of subsurface structures of the object [7, 8] to infrared radiation. This drawback practically excludes some areas of objects or even whole groups of objects. For example, within the same painting one may find areas with paint layers permeable for OCT radiation and enabling deeper imaging, whereas in other spots only the transparent varnish layer is discernible in the tomogram. It has to be noted, however, that some objects that are in principle not permeable for infrared, had been to certain extend examined with success; such examples are stones [9, 10] and wall paintings [11].

Additionally, raising sensitivity of modern Fourier domain instruments results in gradual increasing of the number of accessible objects.

Fig. 1 An in-situ examination of Raphael's *La Muta* in 2014 at Opficio delle Piere Dure in Florence, Italy with the portable OCT tomograph constructed at Nicolaus Copernicus University in Toruń

1.2 Interpretation of the Tomograms

The OCT results are usually presented as cross-sectional views, although some other post processing of the data enables revealing additional features of the object.

The structure of the examined object is shown in a false colour scale: warm colours correspond to high scatter/reflection of the probing light, whereas cold colours mark areas with low scatter. Transparent media (e.g. clear varnishes, glass or air above the surface of the examined object) or areas located beyond the range of penetration are shown dark. The 'strongest' line is usually the air-artwork interface with semi-transparent layers underneath.

It is important to note that the distances along the probing beam are seen in OCT as optical ones. Therefore, to measure true axial distances within the structures in the object (e.g. the layers' thicknesses) one has to divide a distance obtained with the scale bar by the refractive index of the material (for most painting materials ca 1.5). Additionally, since the OCT scans tend to cover a relatively large area (up to 15 mm^2), the axial (in-depth) scale is elongated comparing to the lateral one.

1.3 Additional Post-processing of OCT Data

If series of 150 adjacent scans is collected over an area, they comprise a 3-D cube of data points, which can be further processed with the technique called *gate imaging* described in detail elsewhere [12]. In brief: the slice of voxels of a given thickness (*gate width*) can be extracted from the data cube at a given depth (*gate depth*), always parallel to the surface of the painting and thus independently of its tilt. The 'slice' is averaged and presented in the false colour scale in a form of a 2-D *en face* image (map). This mode of data presentation is in many cases of a great help, e.g. for imaging of the retouchings and overpaintings [12], showing the pattern of internal cracks, delaminations or other structures located within a thick layer of varnish [13, 14]. In some cases, the parameters of canvas (thread count) may be recovered from its imprint in the paint layer [12], which can be especially useful for the paintings which had been lined or transferred in their past and therefore there is no direct access to the original canvas. The imaging of underpaintings is also possible with the quality of the image superior to the standard IR reflectography [15].

2 Exemplary Results of Examination of Artworks

2.1 Objects of Craftsmanship

In many decorative techniques semi-transparent paints or lacquers were used to obtain three dimensional visual effects. For instance, Japanese *nashiji* technique (imitated in 18th–19th c. Europe under the name of *aventurine lacquer*, or *mor-aqqash* in Islamic art) is based on embedding metal (usually gold) flakes in-between two layers of lacquers [16, 17]. OCT gives direct insight into the technology of making of such an object (Fig. 2).

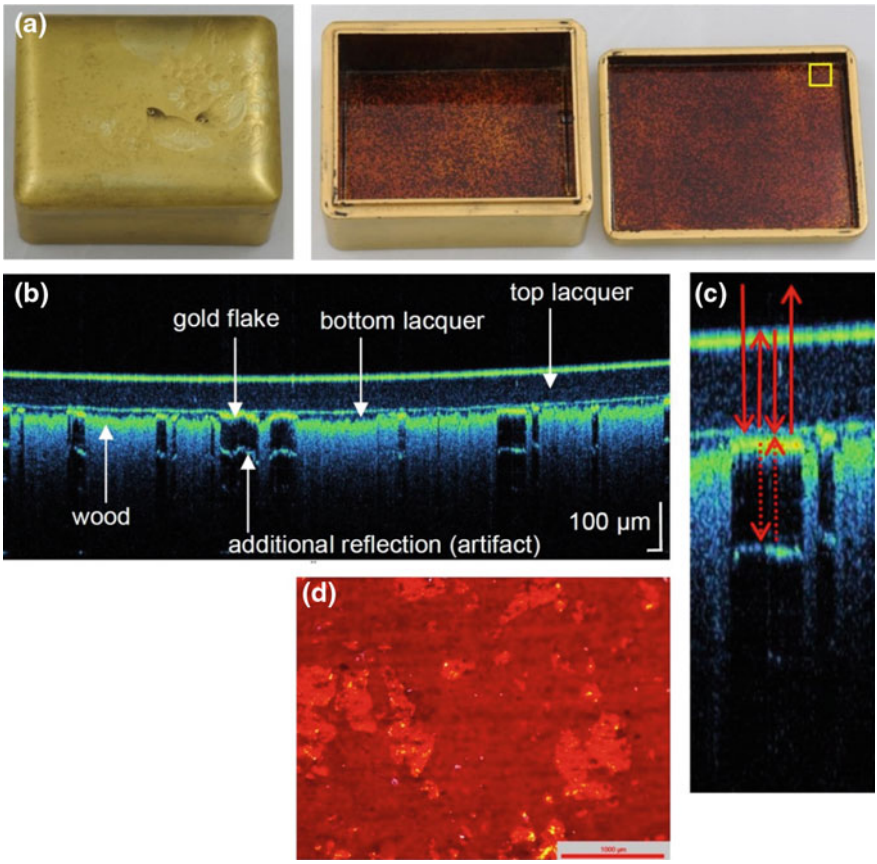

Fig. 2 **a** Gilded wooden box decorated with depictions of quails and herbs, Japan, 19th/20th c., District Museum in Torun, inv. MT/DW/392. Inside of the box and the lid is decorated in nashiji technique. **b** OCT tomogram and **c** tomogram fragment, from the lid (see text for explanation). **d** microscopic image of the inside of the lid

Top layer of lacquer is easily recognizable and its thickness (under 100 µm) and magnificent homogeneity may be assessed. Bottom lacquer layer (onto which the gold flakes had been sprinkled) despite of being relatively thin (ca 15 µm) makes a smooth surface over the roughness of wood. Wooden support is non-transparent to OCT imaging, however since it scatters the probing light, time of returning of the signal to the OCT instrument varies, which creates the effect of 'fading' of OCT signal in the tomogram. Gold flakes are basically also non-transparent to the infrared radiation, however since they reflect the probing beam strongly instead of scattering it, due to multiple reflection of light between the gold and the surface of the upper lacquer an artificial 'interface' is visible beneath the gold flake (Fig. 2c).

Apart from providing knowledge on the technology and layers' build-up OCT can be a useful tool for fast assessing of the artwork's state of preservation.

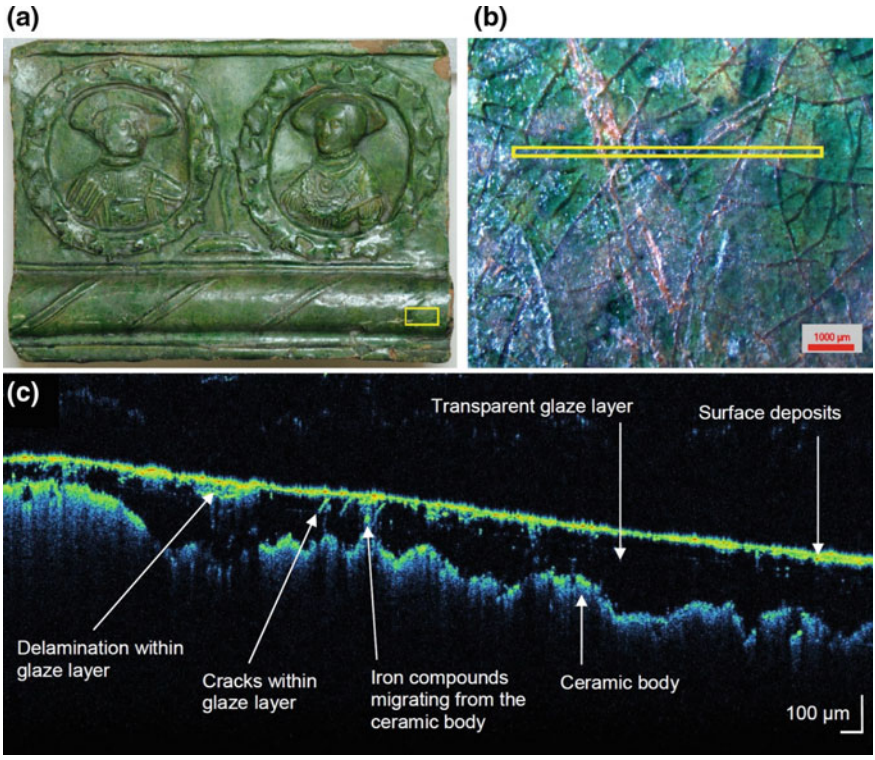

Fig. 3 **a** Ceramic tile, engobe, lead-based, copper-tinted glaze, Torun, 16th c.?, District Museum in Torun, inv. MT/ZK/1065, yellow rectangle marks the location of the microscopic image. **b** Microscopic image of the scanned area, yellow line marks location of the presented tomogram. **c** OCT tomogram

Revealing of many destruction phenomena within the subsurface layers is possible provided that the materials are semi-transparent to near infrared radiation. Transparent and semi-transparent glazes on ceramic objects (Fig. 3c) may be investigated in terms of its thickness and production faults (like air bubbles). Also time-related cracks and delaminations are easily recognised due to the large leap of refractive index between air and lead glass which constitutes the glaze. Semi-transparent dirt deposits on the surface (right-hand side of the tomogram in Fig. 3c) scatter and partially absorb the OCT beam, but, in this case, do not hinder the visibility of the ceramic body underneath the glaze. It is worth to note that OCT can be of use in planning conservation-restoration of such artefacts, through both identification of fragile spots and direct monitoring of the cleaning treatments [18].

More subtle phenomena like, for instance, migration of iron compounds from the ceramic body to the bulk of the glaze (through fine cracks) can be understood thanks to the precise localisation of the examined spot, direct comparison of the tomogram with a microscopic photograph, and, last, but not least, taking into

consideration the history of the object. In this case, the investigated tile was found among many other similar items on the archaeological site of the Teutonic Order Castle in Toruń during the excavation works in 1958–66. The castle ruins had been used as a wasteyard for the whole old city area since the middle 15th c., when the castle was demolished, up to late 19th century, the ceramic objects were therefore subjected to contact with water, earth and mineral depositions.

2.2 Easel Paintings

Since most pigments are non-transparent to infrared radiation when applied in thick layers, practical applicability of OCT to conservation of paintings lies in the imaging of superficial secondary layers rather than in resolving the painting technique of the artist. Information on the build-up of varnish layers (which are usually secondary and often multiple in number) and/or overpaint layers added during some past renovations is crucial for planning of modern restoration treatment.

In some cases optical coherence tomography may also help in authentication of the painting, usually as a complementary tool for some spectroscopic analyses. An interesting example of such an approach is resolving of the sequence of layers in the 17th c. Dutch still life painting, signed J. Walscapele (Fig. 4a). The painting had been in the past subjected to many renovation/restoration treatments. Their effects were obscured by the already aged, yellowed and deteriorated varnish of strong UV-induced fluorescence (Fig. 4b). However, macro-XRF scanning revealed the presence of pigments not used earlier than 19th c.: of zinc and barium white in all the highlights (Figs. 4c and 5e) as well as chromium green (in the area of the tablecloth). Apart from the abovementioned areas the other pigments identified were typical for the 17th c.: calcium based ground, lead white, vermillion, copper based green, ochres and umbers [19].

OCT data were collected in 20 areas which were showing the presence of zinc/chromium. In most of the examined spots a highly scattering, yet infrared-permeable layer was found between the varnishes. It seemed highly probable that it was a 19th c. overpainting. To confirm this hypothesis the microsample (Fig. 4d, e) was collected from the lower edge of the composition (from a perimeter of a paint-loss) as a reference for interpretation of the OCT data. The observation of the cross-section in visible light and under ultraviolet illumination (Fig. 4d, e) confirmed that the secondary paint layer, in this case—dark green (marked 6 in Fig. 4d, e, f) is located between the varnishes.

Also it is a good example of how some layers differ in the photograph and OCT. Two varnish layers on top (7 in Fig. 4d, e, f) are well discernible in OCT (in all examined spots), whereas they are barely visible at the edge of the sample. Such problems may stem from various causes. First of all, OCT is sensitive to leap of refraction index between the layers as well as the presence of dirt, which acts as a light-scattering agent; in such cases the layers are well discernible in OCT tomograms. However, if they are too thin (under ca 3 microns) they will not be seen as

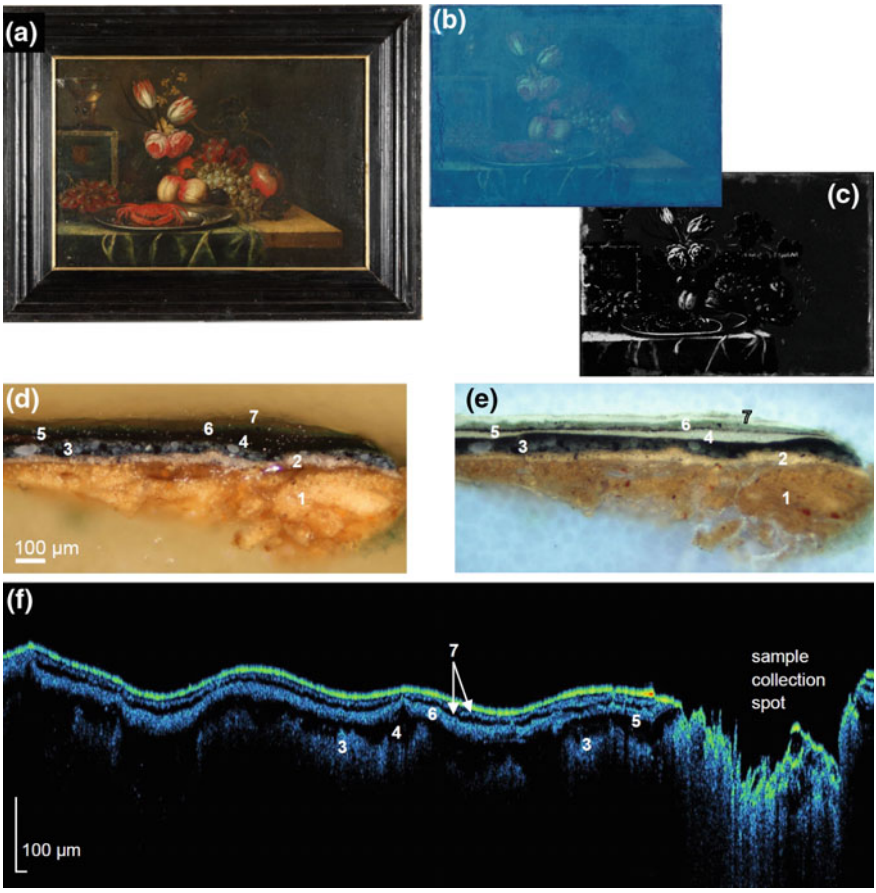

Fig. 4 *Still life with a crab*, Jacob van Walscapelle, 17th c., oil on canvas, 41 × 59 cm, Museum of Warmia and Mazury in Olsztyn. **a** Visible light; **b** UV-induced fluorescence; **c** macro-XRF scan (M6, Bruker Corporation) of the whole picture showing distribution of zinc; **d**, **e** microphotographs of a cross-section of a sample collected from the area of a green tablecloth near the lower edge of the painting: visible light (**d**) and UV-induced fluorescence (**e**), magnification 100×. Description of layers: (1) ground layer, (2) underpaint, (3) blue paint layer, (4) primary varnish, (5) superficial dirt, (6) green paint layer (secondary); (7) two varnish layers. **f** OCT tomogram from the perimeter of sample collection spot, the numbers correspond to the layers identified in the sample (Fig. 4d, e)

separate ones. On the other hand, also the technique of preparation of cross-samples has some drawbacks—e.g. some varnishes are easily dissolvable in embedding resin or, if they are brittle and therefore susceptible to delamination during sampling and embedding.

It is also important to note that although the information provided by the OCT data is restricted to superficial layers and doesn't show true colours, the single scan

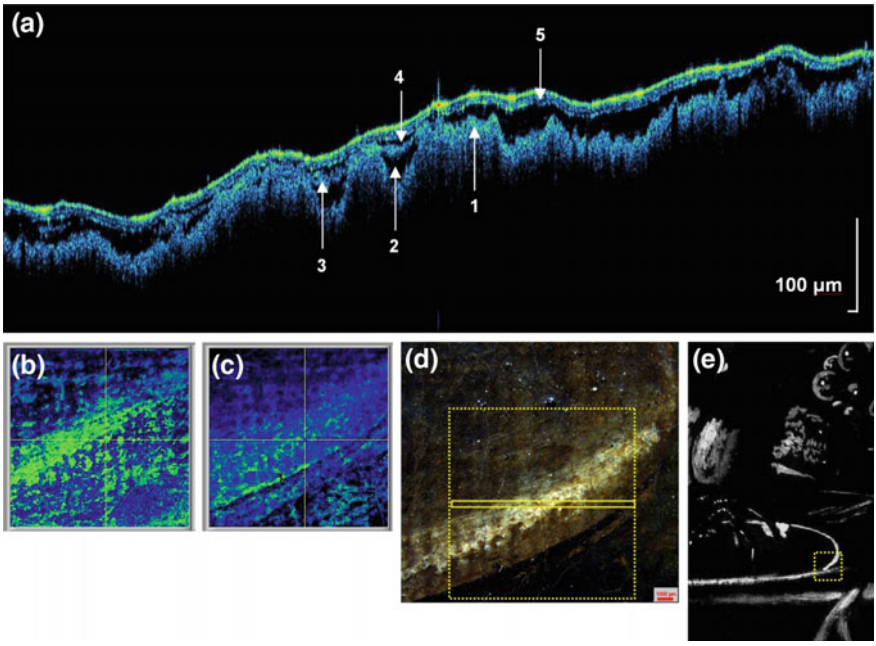

Fig. 5 *Still life with a crab*, Jacob van Walscapelle. **a** OCT tomogram from the area of the rim of the silver plate. Description of layers: (1) primary paint layer, (2) varnish, (3) zinc-rich (secondary) paint layer, (4) varnish, (5) two varnish layers; **b**, **c** coherence gate images—**b**: 19 µm gate depth, 7 µm gate width, **c**: 66 µm gate depth, 7 µm gate width; **d** macrophotography of the examined area, with dashed square marking the scanned area and yellow line marking the location of the tomogram; **e** macro-XRF scan (fragment) showing distribution of zinc, dashed square marks the scanned area

covers much larger area than the sample and therefore the OCT results are more representative.

A common approach is to use the information obtained through minimal sampling to interpret the results of multiple non-invasive analyses. In case of the Walscapelle painting it proved feasible since the good state of preservation of the painting in its central part had excluded further sampling. However, the OCT data collected in zinc-rich areas of highlights (Fig. 5) enabled to precisely locate the zinc-containing layer (3 in Fig. 5a, bright green colour in Fig. 5b) within the whole painting's structure: it is lying between the varnish layers. This conclusion was additionally confirmed by the gate imaging technique (Fig. 5b, c). The highlight on the rim of the silver plate (Fig. 5d) consists of a paint layer lying 19 µm beneath the surface of the painting (Fig. 5b), on top of varnish layer. At the depth of the primary paint layer, 66 µm under the surface (Fig. 5c) there is no paint layer in this shape. To conclude, in the case of *Still life with a crab* the synergistic use of structure analysis (by OCT) and surface-mapping (by means of macro-XRF) enabled resolving both the range, amount and time of renovations of the painting.

3 Conclusions

Optical coherence tomography (OCT) is a non-invasive technique of structural analysis of objects partially transparent to infrared radiation. In this chapter we have presented the results of its successful use for establishing sequence and thickness of transparent or semi-transparent layers as well as deterioration phenomena and secondary coatings in varnished wooden object of craftsmanship, glazed ceramic tile and an easel painting. In the latter case, thanks to the *gate imaging* data post-processing, visualisation of the pattern of overpaintings located within the object's structure was possible.

The other reported applications for cultural heritage objects involved examination of wall paintings [11], paintings on glass support [20], stained glass [21], semi-precious stones such as jade [22, 23] and amber.

Another important application of OCT lies in its potential to monitor the conservation process: removing of secondary layers [24] as well as the consolidation treatment [25] may be observed and evaluated in fast and convenient manner.

Acknowledgements The authors would like to thank Mrs. Alina Targowska and Mrs. Romualda Uziembło from the District Museum in Toruń as well as Mrs. Iwona Kluk from the Museum of Warmia and Mazury in Olsztyn for providing objects for examination.

This research has been co-financed by H2020 IPERION CH project (contract number: 654028) and conducted with use of the research infrastructure of Interdisciplinary Centre for Modern Technology of N. Copernicus University in Toruń, Poland, financed by Regional Operational Programme for Kujawsko-Pomorskie Voivodship (Project No.: RPKP.05.04.00-04-001/10).

References

1. Drexler W, Fujimoto JG (eds) (2015) Optical coherence tomography: technology and applications, 2nd edn. Springer, Berlin, Heidelberg, New York
2. Wojtkowski M (2010) High-speed optical coherence tomography: basics and applications. Appl Opt 49:D30–D61
3. Complete list of papers on application of OCT to examination of artwork may be found at http://www.oct4art.eu: Optical coherence tomography for examination of works of art, Accessed 15 Nov 2018
4. Targowski P, Iwanicka M (2012) Optical coherence tomography: its role in the non-invasive structural examination and conservation of cultural heritage objects - a review. Appl Phys A 106:265–277
5. Targowski P et al (2015) OCT for examination of artwork. In: Drexler W, Fujimoto G (eds) Optical coherence tomography. Technology and applications, Springer, Cham, Heidelberg, New York, Dordrecht, London, pp 2473–2495
6. American National Standard for Safe Use of Lasers: ANSI Z 136.1 - 2007, Orlando: Laser Institute of America, 2007
7. Liang H et al (2013) Optimum spectral window for imaging of art with optical coherence tomography. Appl Phys B 111:589–602

8. Szkulmowska A et al (2007) Applicability of optical coherence tomography at 1.55 μm to the examination of oil paintings. In: Nimmrichter J, Kautek W, Schreiner M (eds) Lasers in the conservation of artworks. LACONA VI proceedings, Vienna, Austria, 21–25 Sept 2005, Springer, Berlin, Heidelberg, New York, pp 487–492
9. Bemand E et al (2011) OCT and NMR for non-invasive in-situ monitoring of the vulnerability of rock art monuments. Proc SPIE, 8084, 80840H-1-40H-8
10. Bemand E, Liang H (2013) Optical coherence tomography for vulnerability assessment of sandstone. Appl Opt 52:3387–3393
11. Striova J et al (2016) Optical devices provide unprecedented insights into the laser cleaning of calcium oxalate layers. Microchem J 124:331–337
12. Targowski P et al (2013) OCT structural examination of Madonna dei Fusi by Leonardo da Vinci. Proc SPIE 8790:87900N
13. Adler DC et al (2007) Comparison of three-dimensional optical coherence tomography and high resolution photography for art conservation studies. Opt Express 15:15972–15986
14. Iwanicka M et al (2016) On the application of optical coherence tomography as a complimentary tool in an analysis of the 13th century Byzantine Bessarion Reliquary. Microchem J 125:75–84
15. Liang H et al (2005) En-face optical coherence tomography–a novel application of non-invasive imaging to art conservation. Opt Express 13:6133–6144
16. Japanese art and design: a glossary, http://www.vam.ac.uk/content/articles/j/japanese-art-and-design-a-glossary/. Accessed 15 Nov 2018
17. Muzeum für Lackkunst - The ABC of Lacquer, http://www.museum-fuer-lackkunst.de/en/abc_of_lacquer. Accessed 15 Nov 2018
18. Iwanicka M et al (2017) The potential of OCT for assessing laser assisted removal of deposits from ceramic tiles. In: Targowski P, Walczak M, Pauli P (eds) Lasers in the conservation of artworks XI. Proceedings of the international conference LACONA XI, 20–23 Sept 2016. NCU Press, Torun, PL, pp 105–114
19. Iwanicka M et al (2016) Combined use of optical coherence tomography and macro-XRF imaging for non-invasive evaluation of past alterations in 17th c. Dutch painting. In: Proceedings of 2nd international conference on art & archaeology 2016: art and archaeology strengthened by measurement techniques, 11–14 Dec 2016, Jerusalem, Israel. https://art2016.isas.co.il/wp-content/uploads/sites/10/2017/03/Session-I-Minerals-Pigments-Dyes-3-Iwanicka.pdf. Acessed 15 Nov 2018
20. Iwanicka M et al (2011) Through-glass structural examination of Hinterglasmalerei by optical coherence tomography. In: Radvan R, Asmus JF, Castillejo M, Pouli P, Nevin A (eds) Lasers in the conservation of artworks VIII. Proceedings of the international conference on lasers in the conservation of artworks (Lacona VIII), 21–25 Sept 2009. CRC Press, Taylor & Francis Group, Sibiu, Romania, London, pp 209–214
21. Kunicki-Goldfinger J et al (2009) Characterization of glass surface morphology by optical coherence tomography. Stud Conserv 54:117–128
22. Liang H et al (2008) Optical coherence tomography in archaeological and conservation science - a new emerging field. Proc SPIE, 7139, 713915-1-15-9
23. Yang M-L et al (2012) Using optical coherence tomography to characterize the crack morphology of Ceramic Glaze and Jade. In: Liu G (ed) InTech: Selected topics in optical coherence tomography, Rjeka, Shanghai
24. Iwanicka M et al (2013) Application of optical coherence tomography (OCT) for monitoring of some conservation treatments. In: Saunders D, Strlič M, Korenberg C, Luxford N, Birkhölzer K (eds) Lasers in the conservation of artworks IX. Proceedings of the international conference on lasers in the conservation of artworks (Lacona IX), 7–10 Sept 2011. Archetype Publications Ltd., London, UK, pp 11–25
25. Iwanicka M et al (2011) Application of optical coherence tomography (OCT) for real time monitoring of consolidation of the paint layer in Hinterglasmalerei objects. Proc SPIE, 8084, 80840G

Chapter 5
Concepts and Applications of the NMR-MOUSE

Bernhard Blümich

1 Nuclear Magnetic Resonance and the NMR-MOUSE

Nuclear magnetic resonance (NMR) is a physical resonance phenomenon utilized to investigate molecular properties of matter by irradiating atomic nuclei in magnetic fields with radio waves [1–3]. The interaction of the atomic nuclei with the magnetic field and the radio waves report about the environment of the nuclei. The nuclei are surrounded by orbiting electrons, which constitute the atoms and the chemical bonds between atoms forming molecules. Because molecules are never at rest, their motion impacts the interaction of the nuclei with the magnetic fields probed by NMR. The NMR phenomenon is put to use in many fields of science and engineering. Most notable are NMR spectroscopy for chemical analysis of molecular structures, magnetic resonance imaging (MRI) for medical diagnostics, and NMR relaxometry for testing of solid materials and fluid-filled porous media. The NMR-MOUSE (MObile Universal Surface Explorer) is a compact and portable MRI sensor for non-destructive materials testing, which measures the information of one pixel of a magnetic resonance image at a time following the principles of NMR relaxometry [4]. Among others it is of growing interest for analyzing objects of cultural heritage [3, 5–8].

1.1 Fundamentals of NMR

Eighteen grams of water contain one mole or 602,214,129,270,000,000,000,000 molecules. Although one can drink this amount in about one second, it takes

B. Blümich (✉)
Institut für Technische und Makromolekulare Chemie, RWTH Aachen University, Worringerweg 2, D-52056 Aachen, Germany
e-mail: bluemich@itmc.rwth-aachen.de

D. M. Bastidas and E. Cano (eds.), *Advanced Characterization Techniques, Diagnostic Tools and Evaluation Methods in Heritage Science*,
https://doi.org/10.1007/978-3-319-75316-4_5

roughly 20,000 times the age of the universe to count to this number. Thus water molecules are incredibly small. Each water molecule consists of two hydrogen atoms and one oxygen atom, and each of these atoms consists of electrons and an atomic nucleus. For such small particles the laws of classical mechanics that describe the motion of the planets and most objects of our daily life no longer apply. Instead the laws of quantum mechanics do. For a large number of elementary particles, they converge to the laws of classical mechanics.

According to the laws of quantum mechanics, many atomic nuclei appear to spin about their axes like a bicycle wheel, which when spinning stabilizes the bicycle in the gravitational field of the earth and keeps the rider from falling off. Spinning atomic nuclei are magnetic and they experience a force in a magnetic field similar to that of a wheel spinning in a gravitational field to the effect that the spinning axis rotates around the direction of the magnetic field. This rotation of the spinning axis is called precession.

The nuclei most frequently observed in cultural heritage studies are the protons, the nuclei of the hydrogen atoms. They are most abundant in the universe and give the strongest NMR signal. Typically, a percentage fraction of a mole of nuclei, for example, 10^{20} nuclei are studied by NMR. Their quantum-mechanical magnetizations sum up to a classical, macroscopic magnetization vector, which also precesses around the direction of the magnetic field ones it has been moved away from it with a radio-frequency (rf) pulse. The precession frequency $\omega = 2\pi\nu$ is measured in NMR. It is proportional to the strength B of the magnetic field,

$$\omega = \gamma B, \tag{1}$$

where the gyromagnetic ratio γ is a constant specific to the type of nucleus.

From classical mechanics one would expect that the magnetizations from all quantum-mechanical magnets in the sample would add constructively to form the macroscopic magnetization. But due to their quantum-mechanical nature, most of them add destructively and only a small fraction of the order of 10^{-5} of all protons give rise to the macroscopic magnetization at a field strength of 1 T. This is why NMR requires much more sample than optical spectroscopies to generate observable signal. But this fraction increases with field strength, so that most NMR spectrometers for chemical analysis use strong magnetic fields up to 23.5 T generated with large, superconducting magnets. High-field NMR instruments, however, are delicate, need special laboratories and trained personnel to operate. Compact NMR instruments like the NMR-MOUSE, on the other hand, use permanent magnets, have lower field strengths between 0.2 and 1.5 T, are robust, small and mobile, and much simpler to use [3–6]. The NMR-MOUSE operates near 0.5 T, about the same field strength as the first generation clinical MRI machines. At this field the precession frequency is near 20 MHz.

In NMR the precessing magnetization is measured following either of the three general ways of probing resonance. These are forced oscillations, free oscillations and noise excitation. For example, forced oscillations are invoked on a string instrument like a violin, which is played with a bow or on a wind instrument.

Free oscillations are invoked on a string instruments that is played with impulses like a guitar or a piano. White noise is usually avoided with musical instruments, because the coherent oscillations can be retrieved only by processing excitation and response in a cross- or auto-correlator. This seems cumbersome and difficult but is common practice in Fourier infrared spectroscopy, where the spectrum is the Fourier transform of an interferogram, which is the same as the autocorrelation function of the radiation transmitted through the sample. Forced and free oscillations are far more simple to understand at least to those somewhat familiar with musical instruments. When comparing sheet music for violin and piano it becomes immediately clear, that the piano is a more versatile instrument than the violin, because several tones can be played at one time compared to one or at best two with the violin. This wealth in diversity is the reason why resonance today is probed in NMR with free oscillations requiring impulses for excitation. Whereas most applications of NMR are found in diagnostic imaging and NMR spectroscopy for structure analysis of proteins [1, 2], a small but growing number of studies concern topics related to cultural heritage [9, 10].

The impulse response of a string is a vibration which decays with time. The eye sees the vibrating string and the ear hears the sound with the pitch determined by the frequency of vibration (Fig. 1a). The connection between what the eye sees and the ear hears, i.e. the connection between the time-domain oscillation $s(t)$ and frequency distribution or spectrum $S(\omega)$ is given in mathematical terms by the Fourier transformation, which decomposes the signal into a sum or integral of rotating waves $\exp\{i\omega t\}$,

$$s(t) = \int S(\omega) \exp(i\omega t)\, d\omega. \tag{2}$$

The spectrum $S(\omega)$ can be retrieved from the observed impulse response $s(t)$ by inverse Fourier transformation. For the oscillations in $s(t)$ to be observable, the magnetic field, which the nuclei see must be the same in each volume element of the sample because the magnet field strength is proportional to the precession frequency (Eq. 1). For example, if the signal is to be observable for 0.1 s, then the precession frequencies should not differ by more than 10 Hz across the sample volume of interest, which corresponds to a relative precision of 0.5×10^{-6} at 20 MHz and according to Eq. (1) defines the minimum field homogeneity of the magnet required to record NMR spectra.

Such field homogeneity is hard to achieve with permanent magnets where the sample is placed inside in the center of the magnet. It is even harder to achieve if the object to be investigated is placed in the stray-field outside the magnet. The latter situation is encountered in studies with the NMR-MOUSE. In inhomogeneous magnetic fields, an impulse response is observed from each volume element with a slightly different frequency. As a result, the sum of all impulse responses rapidly interferes to zero and often cannot be observed at all. But with a second impulse rapidly following the first one and twice as strong, the signal can be recalled in an echo and repeatedly so with a string of impulses (Fig. 1b). Such a spectroscopic

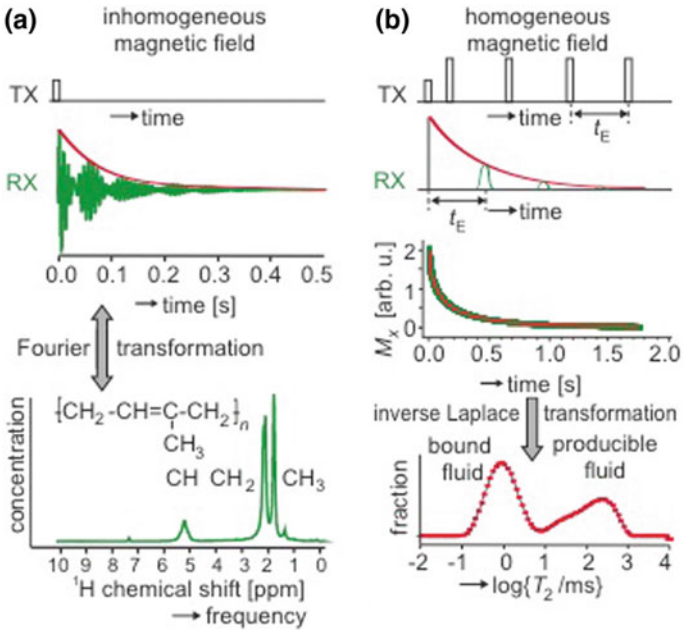

Fig. 1 NMR signals and transformations. TX denotes the transmitter sending the excitation impulses and RX the receiver recording the response signal $s(t)$. **a** Homogeneous magnetic field. Radio-frequency impulse (top), impulse response (middle) of a natural rubber solution, and corresponding Fourier transform or spectrum (bottom). **b** Inhomogeneous magnetic field. Sequence of radio-frequency impulses that generates a train of echoes (top), echo decay envelope schematic and experimental from water saturating tuff stone (middle), and distribution of relaxation times (bottom) obtained with an algorithm reminiscent of an inverse Laplace transformation

echo is not quite the same as an acoustic echo, which returns "hello" somewhat fainter when shouting "hello" into the mountains. The spectroscopic echo relates to time inversion and returns "olleh" and then "hello" when repeated again, etc. Also the amplitude of each spectroscopic echo becomes fainter, and the envelope that connects all echo maxima (Fig. 1b. middle) approximates the signal decay observed in a homogeneous magnetic field (Fig. 1a, middle). The method of observing a signal decay stroboscopicaly in an inhomogeneous magnetic field by a train of echoes is known by the initials CPMG of its inventors Carr, Purcell, Meiboom and Gill [1–3]. There are many advanced methods for measuring relaxation times, diffusion coefficients, distributions and correlation maps of these parameters [3], but the CPMG sequence is the most basic and most often used measuring scheme.

Although the information about the precession frequency is lost in an inhomogeneous field, the information about the signal decay is not. Knowledge of the precession frequency is important to the chemist, because it provides unique information about molecular structures of molecules in solution (Fig. 1a, bottom). Knowledge of the signal decay is important to the material scientist, because it

provides unique information about material properties. For example, a rapid decay on the order of 0.1 ms and less is typical for protons in rigid solids, longer decays are observed for soft solids and viscous liquids. Simple soft materials are often characterized by a single exponential decay with relaxation time T_2, complex and rigid materials show non-exponential decays. A non-exponential decays $s(t)$ can be approximated by a sum or integral of exponential decays,

$$s(t) = \int S(1/T_2)\exp\{-t/T_2\}\ \mathrm{d}(1/T_2), \tag{3}$$

where $S(1/T_2)$ is the distribution of relaxation rates $1/T_2$. Note, that on a logarithmic rate scale, the distribution of relaxation rates converts into a distribution of relaxation times by just a change of sign. This distribution can be retrieved from the observed echo envelope $s(t)$ by algorithms which are reminiscent of the inverse Laplace transformation (Fig. 1b, bottom). But other than inverse Fourier transformation, inverse Laplace-like algorithms are unstable in the presence of measurement noise, so that numerical algorithms introduce a regularization parameter which stabilizes the inversion. In many cases the use of an inversion algorithm is replaced by fitting the observed signal with a sum of two or three exponential functions,

$$s(t) = \sum_{1}^{3} S_i \exp\{-t/T_{2i}\}. \tag{4}$$

The fit parameters are the relative spin concentrations $S_i/s(0)$ and the relaxation times T_{2i}, which can be assigned, for example, to wax and water in the mortar of a wall.

The NMR relaxation time T_2 is known as the transverse relaxation time because it relates to the decay of magnetization transverse to the direction of the magnetic field. There is another relaxation time T_1, the longitudinal relaxation time. It is the time an unmagnetized sample takes to build up nuclear magnetic polarization parallel to the magnetic field once it is exposed to the field. The relaxation rates $1/T_i$ of fluids saturating the pores of porous media like rock or cement are determined by the relaxation rate $1/T_{i,\ \mathrm{bulk}}$, the surface relaxivity ρ_i, the surface to-volume-ratio S/V of the pore and the product of the self-diffusion coefficient D of the pore fluid with the internal magnetic field gradient G_{int} in the pore and the echo time t_{E} (Fig. 1b, middle). The echo time is the time between the maxima of two successive echoes in a multi-echo train. The internal field gradient results from differences in magnetic susceptibility between pore fluid and matrix material,

$$1/T_1 = 1/T_{1,\mathrm{bulk}} + \rho_1 S/V, \tag{5}$$

$$1/T_2 = 1/T_{2,\mathrm{bulk}} + \rho_2 S/V + (\gamma\, G\, t_E)^2 D. \tag{6}$$

If measured in an inhomogeneous applied field, the gradient G is the sum of both, the internal gradient G_{int} in the pore and the gradient of the applied field. Since the pore-diameter is proportional to S/V, these relationships are often

Fig. 2 The NMR-MOUSE. **a** Drawing of the sensor mounted on a displacement table for measuring depth profiles through vertical layer structures such as mortar layers covering walls. The radio-frequency (rf) coil transmits the excitation impulses and receives the signal. **b** Setup of the sensor measuring a depth profile of the natural moisture content through a painted, wet wall in the chapel of St. Mary in Chaalis

explored to approximate the pore-size distribution by the relaxation-time distribution, whereby the bulk relaxation rates and the diffusion in internal field gradients are neglected. For example, water in porous stone often gives rise to two peaks (Fig. 1b, bottom), one at short relaxation times for bound water trapped in small pores and one at longer relaxation times for water that can be exchanged by drying and wetting. In cultural heritage studies, differences in pore-size distributions can result from weathering, stone conservation treatments, as well as grain-size variations in building materials (Fig. 2).

1.2 The NMR-MOUSE

In most NMR studies, the sample rests inside the magnet, where a homogeneous magnetic field can most easily be generated. Then, however, the diameter of the magnet bore limits the sample size. Alternatively, the sample can be placed in the stray-field outside the magnet. There the sample size is not limited, but the magnetic field is usually strongly inhomogeneous. The field inhomogeneity can be tolerated if material properties are of interest which can be derived from relaxation decays. In fact, stray-field NMR is a method of non-destructive materials testing, in particular in terms of component amplitudes and relaxation times of multi-exponential decays, whereby the relaxation times $T_{2\text{eff}}$ measured in the strongly inhomogeneous field of the NMR-MOUSE are similar to the relaxation times T_2 measured in homogeneous field. Moreover, with a radio-frequency impulse only a narrow range of frequencies can be probed, which falls within the inverse duration of the excitation impulse. This translates into collecting signal with stray-field sensors, which derive from a narrow slice within the object under investigation. The NMR-MOUSE has been

designed in such a way, that this so-called sensitive slice is very flat and at a fixed distance from the surface of the sensor. Depending on the particular version of the NMR-MOUSE, the slice is 5, 10, or 25 mm away from the sensor surface, and its diameter is 10, 10, and 40 mm, respectively, with the slice thickness adjustable between 0.01 and 0.1 mm. Depth profiles covering the range from the slice distance to zero can be measured through objects by mounting the NMR-MOUSE on a computer-controlled sliding table, placing the sensor close to the object and retracting it step by step between measurements. At each position the relaxation decay is measured with a CPMG sequence, and a parameter derived from the relaxation decay is plotted versus position of the sensitive slice, in this way defining the depth profile. This parameter can be, for example, the signal amplitude, the relaxation time, a component amplitude or relaxation time (cf. Eq. 4), or a peak integral in the distribution of relaxation times. Amplitudes report concentrations, and relaxation times report material properties, for example elasticity. For noisy signals, often a weight parameter w is displayed as the profile amplitude. This parameter is the ratio of the integrals from the initial and the final parts of the relaxation decay. It is a relaxation-weighted spin density defining contrast similar to the one encountered in many medical magnetic resonance images. Depending on the position of the divide between both parts, the contrast can be optimized.

2 Selected Applications of the NMR-MOUSE

2.1 Mummies and Bones

Depending on the culture, mummies may be wrapped in textiles so that the NMR signal of mummies at a given measurement depth derives from textiles, skin, or bone. Bone consists of compact bone and of spongy bone with a cellular structure (Fig. 3c). Objectives to study mummies and bones with the NMR-MOUSE are to determine the thickness of the different textile and tissue layers, and to determine the proton density of the bone and its variation with depth.

Bone is a rigid composite material mostly from organic collagen, inorganic hydroxylapatite ($Ca_{10}(PO_4)_6(OH)_2$) and water. The bone density determined by ^1H NMR is organic bone density, while the bone density determined by X-ray analysis is inorganic bone density. The proton density of untreated bone indicates the state of preservation of the organic collagen matrix. Depending on the deterioration processes, organic and inorganic bone densities are not proportional to each other. Proton densities higher than in reference materials indicate the presence of other hydrogen-containing substrates such as water or conservation agents as observed, for example, in the glacier mummy Ötzi [11] and in the tibia of Charlemagne [3], respectively.

The transverse magnetization from the dry tissue of historic bone and mummies decays rapidly, and the short CPMG echo trains are analyzed with monoexponetial

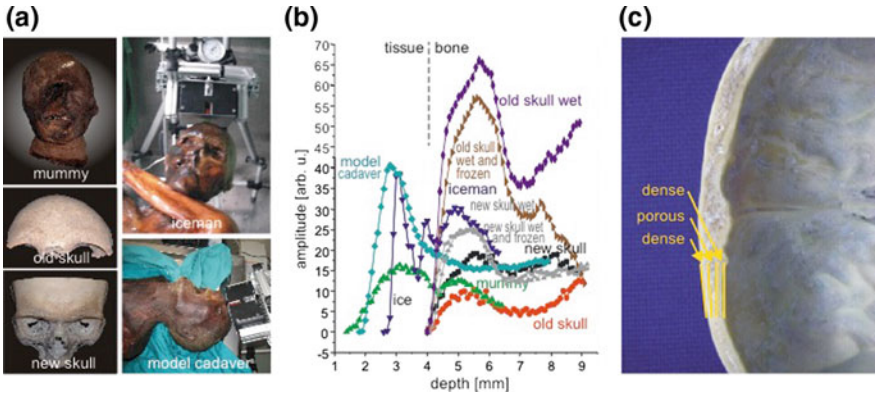

Fig. 3 Depth profiles through human foreheads. **a** Photographs showing the Egyptian mummy head, an about 1000-year-old skull excavated from the Dahlheim monastery (courtesy of Frank Rühli), a recent skull from the anatomical collection of the University of Zürich, the 5300-year-old glacier mummy Ötzi (Archeological Museum Bozen), and a model cadaver dried down to the weight of Ötzi. **b** Comparison of NMR depth profiles. **c** Bone structure of the skull. Porous bone in the center is framed by dense bone on the inside and the outside

fits or processed by calculating the relaxation-weighted spin density w from partial integrals over the echo train. Because bone is rarely flat and often heterogeneous, the signal amplitude corresponds to organic bone density only if the sensitive volume of the sensor is fully inside the bone material.

Bone degradation has been investigated in a comparative study (Fig. 3a) of signal-amplitude depth profiles (Fig. 3b) through the forehead of the Neolithic glacier mummy Ötzi in the Archeological Museum of Bozen [3, 11]. The iceman was murdered about 3250 BC near Tisenjoch in the Tyrolian Alps where his body was covered with snow and remained frozen since then until he was found in 1991. The ice-covered body is kept frozen in the museum at about −6.5 °C and 97% humidity. The depth profile through the iceman's forehead shows the layer of ice, a signal from skin and deeper down the signal from bone. Within the bone the signal first peaks and then decreases following the expected bone density variation in the forehead (Fig. 3c). Depth profiles from a well-preserved skull and a degraded skull confirm this variation of bone density. The corresponding depth profile through the forehead of a recently mummified cadaver does not show it probably because the tissue layer covering the skull bone is too thick and bone signal is not detected. On the other hand, the profile of an Egyptian mummy head shows the tissue wrapping and then the beginning of the signal from bone.

The bone signal from the iceman is somewhat higher than that of the recent skull. This is explained by liquid water in the iceman's skull based on a comparison of depth profiles through dry, wet, as well as wetted and subsequently frozen bone from the new skull and the old skull. The profiles from the new skull section wetted and subsequently frozen at −30 °C overlap and are only slightly higher than the

profile from the dry new skull. The overlap of both profiles indicates, that the water in the skull is in fact not frozen due to freezing-point depression from it's confinement to small pores. The dry profile of the old skull is significantly lower than that of the new skull, indicating lower bone density. But upon soaking it is much higher than that of the wet new skull due to water residing in the enlarged pores formed by the degradation of the bone. Moreover, the profile amplitude of the wet old skull lowers at negative Celsius temperature, because the water in the enlarged pores freezes and the signal from the solid ice decays within the deadtime of the sensor. The profile amplitude of the iceman being only slightly higher than that of the wet/frozen new skull suggest that the water in the forehead of the iceman is not frozen, and that the skull of the iceman is very well preserved.

2.2 Easel Paintings

Most easel paintings are produced on wood or canvas. Before painting, these materials are furnished with covers of other materials such as textiles and primer to provide mechanical strength and prepare the surface for painting. Paint layers consisting of pigments and binder are applied one after the other, and the final work of art is varnished to preserve it and give it a shiny finish.

Compared to other nondestructive techniques for the analysis of thin layers such as optical coherence tomography, multi-spectral imaging, and tera-Hertz spectroscopy, the depth resolution of the NMR-MOUSE is limited to about 0.01 mm [12] but the depth range can go up to 25 mm. On the other hand, the sensitive spot is a wide slice with a diameter about 10 mm. Thus the signal comes from a flat slice 1000 times thinner than wide. This requires critical alignment of the sensor parallel to the layers to be resolved. Moreover, the layers need to contain hydrogen nuclei.

The goals of studying easel paintings with the NMR-MOUSE are manifold [3, 5, 7, 8]. One goal is to characterize the softness or brittleness of the binder in terms of relaxation rates, which change with pigment type and concentration, aging, solvent exposure, storage conditions and conservation impact. Another goal is to learn about the stratigraphy of the wooden panel or canvas [12, 13]. For example, in the painting 'Adoration of the Magi' by Perugino on wood from 1470 AD reinforcing textile layers of different thickness' have been found in two positions (Fig. 4a), with the thicker one at the joint of two wooden boards. Different paint layers can only be identified in fortunate cases when the layers are sufficiently flat across the diameter of the sensitive slice. This is rarely the case with canvas paintings, because many paintings show craquelure, a network of fine cracks, which forms when the paint layers contract upon aging and the resulting flakes bend.

From a restorer's point of view, the solvent-paint interaction is of interest, in particular, the ingress of solvent when cleaning the painting and repairing damaged sections [14, 15]. In a comparative study of two 400-year-old paintings by the same

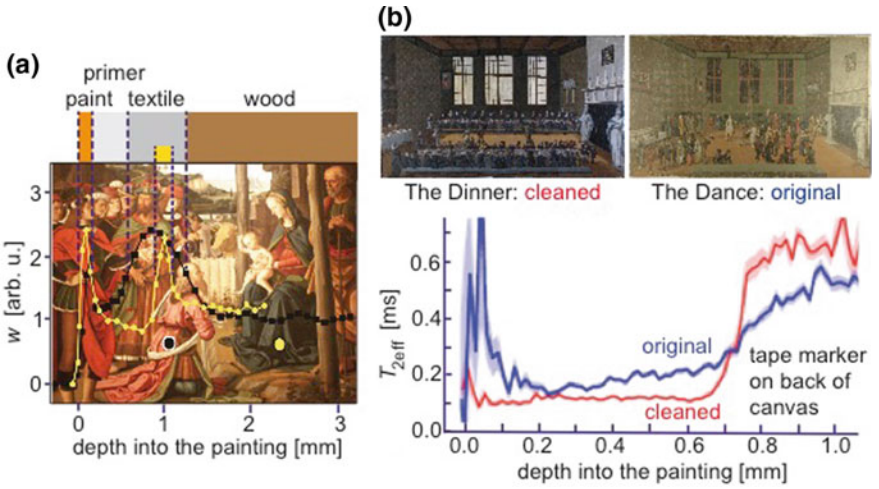

Fig. 4 Easel paintings. **a** 'Adoration of the Magi' by Perugino on wood from 1470 AD. The overlaid depth profiles collected at the two marked positions show the paint layers and the textile layers. The textile layers differ vastly in thickness. **b** The paintings 'The Dinner' and 'The Dance' from the 'Pipenpoyse Wedding' 1616, one restored and solvent cleaned, the other never restored (top) along with T_{2eff} depth profiles through the paint and canvas regions (bottom)

artist, one in its original state and the other one cleaned and restored it was found, that the T_{2eff} NMR relaxation times across the paint layer are low throughput for the restored painting, while they are higher in the lower than at the upper paint layers for the unrestored painting (Fig. 4b) [14]. Due to the fact, that low T_{2eff} indicates less mobile molecules ore more brittle material and higher T_{2eff} softer material, this observation can be explained by considering that paint binder is a multi-component mixture of molecules ranging in size from large to small. The small ones can evaporate and be washed out by solvents. The gradient in T_{2eff} across the thickness of the paint layer from the painting in its original state can be explained by evaporation of low molecular-weight molecules from the paint binder over the lifetime of 400 years of the painting. The low T_2 across the entire thickness of the cleaned painting suggests that the cleaning solvent has drained the small molecules from across the whole paint layer. This suggests, that the NMR-MOUSE is as suitable tool for optimizing solvent cleaning procedures for paintings [14, 15] and for studying drying and aging processes of paint [12]. Paint can age naturally over long times or be aged artificially in short times. To achieve the same result with artificial aging as with natural aging is extremely difficult so that NMR relaxation studies can help to examine the authenticity of a painting in question when compared to other verified paintings of the claimed artist from the same time.

2.3 Wall Paintings

Walls are painted either dry with paint containing pigments and binder or on fresh mortar using just pigments without binder. These techniques are referred to as secco and fresco, respectively. Both can be discriminated in NMR depth profiles when wetting the wall and observing the wetting and subsequent drying processes, because the binder in a secco forms a barrier to the water migration.

The pigments of a fresco are first embedded upon drawing in the calcium hydroxide forming in the reaction of lime with water. Subsequently the calcium hydroxide reacts with carbon dioxide to form calcium carbonate. To maintain a moist wall for painting for an extended period of a day's work, several thin mortar layers are applied with finer and finer grain size towards the surface. The first mortar layer is allowed to partially dry, and then further layers of the same or finer grain size follow. Each layer may vary not only in thickness, composition, and grain-size distribution, but also in the pressure applied to the uncured wet layer during plastering. Together, composition and pressure, determine the pore-space and water-absoption properties of the particular layer, and the details of the resultant layer structure are a fingerprint of the manufacturers skills and techniques.

The NMR-MOUSE provides unique information about the layer structure of frescoes by probing the moisture distribution and mobility across several layers. Moreover, preservation treatments from the past may be identified on the basis of abnormal signal strength from higher or lower hydrogen density. To measure the stratigraphy of the mortar layers from a fresco, the wall must be sufficiently wet to provide NMR signal. When not naturally wet, the wall needs to be sprayed with deionized water possibly after removing a wax layer applied in former conservation work [3, 5, 7]. From a depth profile, the thickness each resolved layer can be determined, and from the multi-echo decay envelope, component amplitudes and relaxation times can be determined either by fitting a sum of exponential functions or from the distribution of relaxation times obtained by inverse Laplace transformation. In many cases two peaks are observed in the distribution of relaxation times from water in porous media, the one at short relaxation times quantifying the amount of bound water and the one at long relaxation times the amount of free water that can be exchanged by wetting and drying. The total signal amplitude corresponding the integral of the complete relaxation-time distribution measures the total amount of water and, when scaled relative to the signal of bulk water, provides the volumetric moisture content. Correspondingly, peak integrals quantify the amounts of bound and free water (cf. Fig. 1b, bottom). Note, that when completely water saturated, the distribution of relaxation times pretty well maps the pore-size distribution unless the applied magnetic field has a strong gradient as in the case of the NMR-MOUSE. In this case, the pore size no longer scales linearly with the relaxation time [16].

Water transport through painted walls damages the painting because soluble salts are carried along, which crystallize at the surface as the water evaporates. Because the moisture flux is proportional to the moisture content, the *moisture content* is

usually taken as a first indicator for potential damage. Unless the air humidity is high, the moisture content of wet walls increases from the outside towards the inside as a result of the dynamic balance between water uptake by capillary water rise or some other source and evaporation through the wall surface [17, 18]. Such moisture-content profiles can be mapped directly and with high resolution by NMR signal-amplitude profiles. Yet the procedure is slow in contrast to other methods, none of which, however, can provide the high spatial resolution of the NMR-MOUSE. But such profiles are needed to base restoration procedures on sound engineering evidence of quantitative moisture flux, which can be obtained from modelling experimental NMR depth profiles of moisture content [19].

Moisture-content profiles are smooth as long as the wall is homogeneous. This is not so for Roman-style frescoes, which are painted on an intricate set of mortar layers with different grain sizes [19–21]. Moreover, they often have received conservation treatments with wax and other agents [20]. The stratigraphy of untreated frescoed walls in the Villa of the Papyri has been studied in Herculaneum (Fig. 5). The walls are kept at high moisture content from maintaining high air moisture in the room through evaporation of water from buckets placed on the floor to suppress water evaporation and the associated outcropping of salts from the frescoed walls (Fig. 5a). The depth profiles derived from CPMG trains reveal the mortar layer structures in terms of the moisture content, which is proportional to the signal average of the first few echoes (Fig. 5b) and in terms of the effective transverse relaxation time $T_{2\text{eff}}$ extracted from the multi-echo decays (Fig. 5c). The peaks in the amplitude profiles identify regions with high water content. The amplitude modulation with depth arises from differences in the pore spaces of the mortar layers. They are characteristic for way the wall was prepared for painting. Different craftsman or enterprises used different techniques, so that a comparative analysis of NMR depth profiles into frescoed walls opens a new window into the past of a particular fraction of the human society. It is striking that

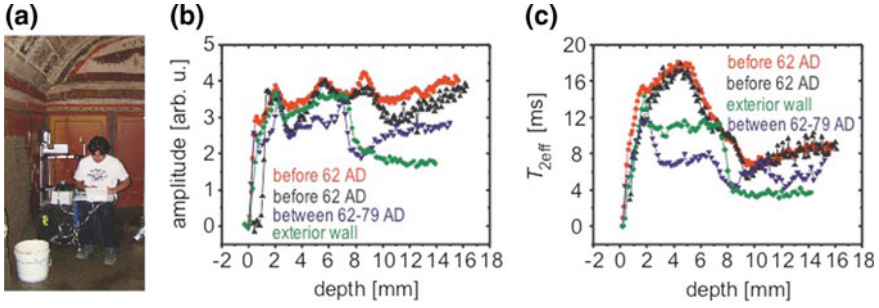

Fig. 5 Roman frescos [20]. **a** Set-up for depth profiling in the excavated room of the Villa of the Papyri in Herculaneum. **b** Moisture distribution across the mortar layers reporting the manufacturing technology and tricks of the trade from former times. **c** Distributions of relaxation times corresponding to the moisture profiles. Short relaxation times are usually characteristic for small pores, large ones for large pores

the amplitude profiles (Fig. 5b) are rather similar but that the two dating from before the earthquake in 62 AD are slightly wider than the other two, of which one is from a wall reconstructed after the earthquake and before the eruption of Mount Vesuvius in 79 AD. This suggests, that the other slightly narrower profile is also from a wall built after the earthquake.

3 Summary

Mobile NMR is not a standard analytical technique in the portfolio of art conservators and restorers because it is a comparatively young technology. From the many facets of NMR the imaging modality is of greatest interest for materials and cultural heritage studies. Mobile NMR with the NMR-MOUSE is essentially a form of one-dimensional imaging with contrast closely related to that in medical magnetic resonance imaging. The NMR-MOUSE differs from the MRI instruments used in hospitals in that it is small and portable, and its use differs in that the object rests outside the magnet and that the image is acquired pixel by pixel by physically moving a sensitive slice of the size of a small coin non-destructively through the object. The detected signal derives from hydrogen nuclei, so that hydrogen must be present in the object. Metallic or magnetic objects cannot be studied, because NMR employs magnetic fields and radio-frequency radiation.

Hydrogen nuclei are found in water and organic compounds contained in textiles, paper, leather and parchment, biological tissues, wood, wax, and many conservation agents. The NMR signal of fluids and soft matter is easiest to detect, because their CPMG decays are long, whereas the decays from hard matter like paper and varnish are short and may largely get lost during the deadtime of the instrument before they can be acquired. Therefore, porous media containing moisture can easily be analyzed by measuring the NMR signal of the fluid inside. This is the strategy when measuring depth profiles into frescoes or studying stone conservation treatments [16, 20, 22]. A similar situation is encountered when analyzing the drying of paint or solvent penetration in investigations of varnish-removal procedures for paintings or musical instruments. Wax, leather and parchment are examples of soft matter, which can well be studied by analysis of CPMG decays and more advanced two-dimensional Laplace-NMR methods [3]. The signals from wood, paper, dry paint and varnish are more demanding to measure because these materials contain only little free and bound water in addition to protons in the solid matrix material. So far the most rewarding studies with the NMR-MOUSE in the field of cultural heritage concern paint drying and solvent ingress relating to the optimization of restauration procedures for paintings, the analysis of stone and mortar to learn about their stratigraphy in the context of conservation and consolidation work, and the detection of conservation agents, wax and varnishes in frescoes, painted walls, and bones [3, 7, 8].

Acknowledgements The development of the NMR-MOUSE and related compact NMR instruments benefitted from continuing support of the European Community in the projects E!2214 - EUROCARE MOUSE, EU-ARTECH, and CHARISMA.

References

1. Ernst RR, Bodenhausen G, Wokaun A (1987) Principles of nuclear magnetic resonance in one and two dimensions. Clarendon Press, Oxford
2. Blümich B (2005) Essential NMR. Springer, Berlin
3. Blümich B, Haber-Pohlmeier S, Zia W (2014) Compact NMR spectroscopy. de Gruyter, Berlin
4. Eidmann G, Savelsberg R, Blümler P, Blümich B (1996) The NMR MOUSE: a mobile universal surface explorer. J Magn Reson A 122:104–109
5. Blümich B, Perlo J, Casanova F (2008) Mobile single-sided NMR. Prog Nucl Magn Reson Spectrosc 52:197–269
6. Casanova F, Perlo J, Blümich B (eds) (2011) Single-sided NMR. Springer, Berlin
7. Capitani D, Di Tullio V, Proietti N (2012) Nuclear magnetic resonance to characterize and monitor cultural heritage. Prog Nucl Magn Reson Spetrosc 64:29–69
8. Blümich B, Casanova F, Perlo J, Presciutti F, Anselmi C, Doherty B (2010) Noninvasive testing of art and Cultural Heritage by mobile NMR. Acc Chem Res 43:761–770
9. Capitani D, Proietti N (eds) (2015) Special issue: NMR in cultural heritage. Magn Reson Chem 53:1–77
10. Rehorn C, Blümich B (2018) Cultural heritage studies with mobile NMR. Angewandte Chemie International Edition 57(25):7304–7312
11. Rühli F, Böni T, Perlo J, Casanova F, Baias M, Egarter E, Blümich B (2007) Non-invasive spatial tissue discrimination in ancient mummies and bones in situ by portable nuclear magnetic resonance. J Cult Heritage 8:257–263
12. Presciutti F, Perlo J, Casanova F, Glöggler S, Miliani C, Blümich B, Brunetti BG, Sgamellotti A (2008) Noninvasive nuclear magnetic resonance profiling of painting layers. Appl Phys Lett 93, 033505-1-3
13. Casanova F, Perlo J, Blümich B (2006) Depth profiling by single-sided NMR. In: Stapf S, Han SI (ed) NMR imaging in chemical engineering, pp 107–123. Wiley, Weinheim
14. Fife GR, Stabik B, Kelley AE, King JN, Blümich B, Hoppenbrouwers R, Meldrum T (2015) Characterization of aging and solvent treatments of painted surfaces using single-sided NMR. Magn Reson Chem 53:58–63
15. Angelova LV, Ormsby B, Richardson E (2016) Diffusion of water from a range of conservation treatment gels into paint films studied by unilateral NMR. Microchem J 124:311–320
16. Sharma S, Casanova F, Wache W, Segre AL, Blümich B (2003) Analysis of historical porous building materials by the NMR-MOUSE. Magn Reson Imag 21:249–255
17. Proietti N, Capitani D, Lamanna R, Presciutti F, Rossi E, Segre AL (2005) Fresco paintings studied by unilateral NMR. J Magn Reson 177:111–117
18. Di Tullio V, Proietti N, Gobbino M, Capitani D, Olmi R, Priori S, Riminesi C, Giani E (2010) Non-destructive mapping of dampness and salts in degraded wall paintings in hypogeous buildings: the case of St. Clement at mass fresco in St. Clement Basilica, Rome. Anal Bioanal Chem 396:1885–1896

19. Oligschläger D, Waldow S, Haber A, Zia W, Blümich B (2016) Moisture dynamics in wall paintings monitored by single-sided NMR. Magn Reson Chem 53:48–57
20. Haber A, Blümich B, Souvorova D, Del Federico E (2011) Ancient Roman wall paintings mapped nondestructively by portable NMR. Anal Bioanal Chem 401:1441–1452
21. Fukunaga K, Meldrum T, Zia W, Ohno M, Fuchida T, Blümich B (2013) Nondestructive investigation of the internal structure of fresco paintings. IEEE Digit Heritage 1:81–88
22. Di Tullio V, Proietti N, Capitani D, Nicolini I, Mecchi AM (2011) NMR depth profiling as a non-invasive analytical tool to probe the penetration depth of hydrophobic treatments and inhomogeneities in treated porous stones. Anal Bioanal Chem 400:3151–3164

Chapter 6
Application of HPLC–DAD–QTOF to the Analysis of Natural and Synthetic Organic Pigments in Paint Layers

Enrique Parra

1 Introduction

Among the whole topics in the field of art materials, one of the most interesting and fascinating is that concerning with the study of dyestuffs and organic pigments because it revels the ancient connection between art and life science. If the analysis of inorganic pigments is nowadays an habitual practice thanks to well-established techniques such as SEM-EDX (Scanning Electron Microscopy—Energy dispersive X-ray spectroscopy), Raman and other spectroscopic methods, the characterization of organic lakes is near to be considered as a routine procedure. The main factors contributing to the difficulty of the task are the intrinsic chemical complexity of the matrix, the availability of very small fragments of pictorial film, the low concentration of the organic pigments in the paint layers and the chemical similarity of the analytes.

Lake pigments have yet been analyzed using RAMAN microspectrometry although total elucidation of unknowns and similar dyes still is far from the goal of characterizing a lot of cases in which chemical similarity and interference of the matrix don't allow it [1].

The analysis of pure layers of colored lakes (for example a thick layer of a red lake glaze) has been practiced and achieved since the last twenty years [2]. When the lake was altered or was not pure, e.g. when present in the form of isolated grains of organic pigment in a inorganic matrix, its identification was almost impossible due to the lack of sensitivity of the old equipments [3]. While the red lakes have been extensively studied since the beginning [4], yellow ones were barely investigated and rarely detected in paintings. Nowadays HPLC (high performance liquid chromatography) technique is living a revolution in this research field due to the

E. Parra (✉)
Instituto del Patrimonio Cultural de España, Secretaría de Estado de Cultura, C/Pintor el Greco 4, 28040 Madrid, Spain
e-mail: enrique.parra@mecd.es

D. M. Bastidas and E. Cano (eds.), *Advanced Characterization Techniques, Diagnostic Tools and Evaluation Methods in Heritage Science*,
https://doi.org/10.1007/978-3-319-75316-4_6

coupling of the new high sensitivity ultra-HPLC separation systems with powerful and extra sensitive and precise mass detectors. One of the highest performing among them is the Quadrupole—Time of Flight Mass Spectrometer (QTOF) [5]. Using this detector, together with DAD it is possible to detect substances in the range of atto-mol, making feasible the detection of red, brown, yellow and blue dyes in paint micro—samples even if in the form of glazes or as minor colored compound of organic-inorganic pigment mixtures [6]. In addition, several other compounds, including lipids, fatty acids, glycerides and di- and tri-terpenes, can be detected in the same analysis with a unique sample injection.

2 Materials and Methods

2.1 Experimental

Optical polarized light microscopy (PLM) analysis was performed on embedded samples, polished to get a cross section. Embedding resin was poly—ethyl-metacrylate Technovit 4004 (Kulzer). Micro—photographs were obtained using a Olympus BX-51 polarized light microscope, with reflected light, using visible or ultraviolet (UV) light. In this last case, autofluorescence of organic materials was used to obtain images to detect and delimitate the areas or layers of the cross section where animal glue, terpene resins, red lakes were present. Fourier transform infra—red spectroscopy (FTIR) analysis was performed on micro—sample's accessible surfaces (varnish and background layer mainly), using a Universal Attenuated Total Reflectance (UATR) accessory, without further preparation, and were recorded between 400 and 4000 cm^{-1} in a Bruker Tensor 27 spectrophotometer.

Scanning electron microscopy (SEM) with energy dispersive X-ray (EDX) elementary analysis was conducted with a Hitachi S340N Scanning Electron Microscope working with a EDX analyzer equipped with a Bruker Quantax X Flash SDD, with a spectral resolution of 125 eV Images where obtained working with a retro—dispersed electrons.

HPLC–DAD–QTOF analysis was performed on a Agilent 1200 HPLC system with autoinjector, equipped with a DAD detector and a Agilent 6530 QTOF detector. The conditions for HPLC–DAD–MS analysis were fixed as follows. Hydrolysis of the microsamples was achieved in 1.5 mL Eppendorf vials, adding to less than 100 µg sample, 100 µL of a mixture of water/methanol/hydrofluoric acid 4 M 1:1:2 (volume) [6]. After heating 10 min to 60 °C, vial was evaporated to dryness at 100 °C with nitrogen flushing. Extraction of the soluble organic compounds was performing by adding 200 µL of a mixture methanol/dimethylformamide 1:1, sonicating the closed vial without temperature controlling (always less than 50 °C) for 15 min. Later the closed vial was heated 110 °C during 20 min, the it was allowed to cool to room temperature, opened and evaporated to 20–30 µL at 100 °C, with nitrogen flushing. 1–2 µL was injected.

The chromatographic HPLC method is detailed now. Column Agilent Zorbax-C18 SB 1200 bar, 50 × 2.1 mm, particle size 1.8 mm, temperature 40 °C, flow 0.7 mL/min. Mobile phase was composed of (A) 0.1% (volume) aqueous formic acid and (B) pure acetonitrile, working with the following gradient: t = 0 min 90% A linear gradient to 100% acetonitrile at 25 min. This composition was held till 30 min. DAD detector swifts between 200 and 800 nm, monitorizing at λ = 275 nm, λ = 350 nm, λ = 550 nm and λ = 600 nm. QTOF detector worked in negative mode [Electrospray ESI (−)], gas temperature 300 °C, gas flow 8 L/min, nebulizer: 55 psi, sheath gas temp 400 °C, sheath gas flow 12 l/min, capilar voltage (−) 3500 V, fragmentor: 185 V. Acquisition was done in MS and MS/MS mode, with a mass range of 100–1700 m/z units. For indigoid dyestuffs MS detector worked also in positive mode [Electrospray ESI (+)] with the same conditions, but with a gas flow of 5 L/min.

2.2 Results and Discussion

All the chromatograms obtained with the above described methodology have been processed with the Agilent Mass Hunter software. Data processing involved the comparison of the UV–VIS and MS chromatograms in order to isolate the peaks related to coloured compounds, the extraction from the Total Ion Chromatograms (TIC) of all the single ion chromatograms (EIC—Extracted Ion Chromatogram) and finally the identification of compounds by comparison with a reference database and by study of the fragmentation pattern in the MS/MS spectra. The characterization of colored lakes started with the identification of those compounds notoriously assigned to the different species, i.e. carminic acid ($C_{22}H_{20}O_{13}$), kermesic acid ($C_{16}H_{10}O_8$) and flavokermesic acid ($C_{16}H_{10}O_7$) for the cochineal; brazilein ($C_{16}H_{12}O_5$), brazilin ($C_{16}H_{14}O_5$) and type C ($C_{13}H_8O_5$) for the brasilwood; alizarin ($C_{14}H_8O_4$), purpurin ($C_{14}H_8O_5$) and rubiadin ($C_{15}H_{10}O_4$) for the madder; laccaic acids (A–F) for Lac dye. In a second step the detailed study of the fragmentation patterns allowed the identification of the glycosides and other secondary compounds. All the masses detected and recognized as markers, but not yet identified, have been catalogued as unknown compounds. The identification of such minor compounds, not directly related to the previous ones, is being carried out.

The analyses of indigoid dyes revealed the limited efficiency of the developed method in the negative ionization of this specific class of compounds. In any case this not represented a big problem since the recognition of blue indigoid dyes (indigo and woad) is possible thanks to the characteristic UV visible spectra of their main compounds, indigotin and indirubin, which presents a typical absorption around 616 and 550 nm respectively. The more challenging results are been achieved with yellow and green lakes [7], with the full characterization of almost all the aglycons (mainly flavonoid dyes) and the related glycosides. In Fig. 1 are shown the UV–VIS and the Mass Chromatograms of a green lakes obtained from ripe buckthorn berries (*Rhamnus cathartica* L.), with the identifyed compounds on each of the peaks [8].

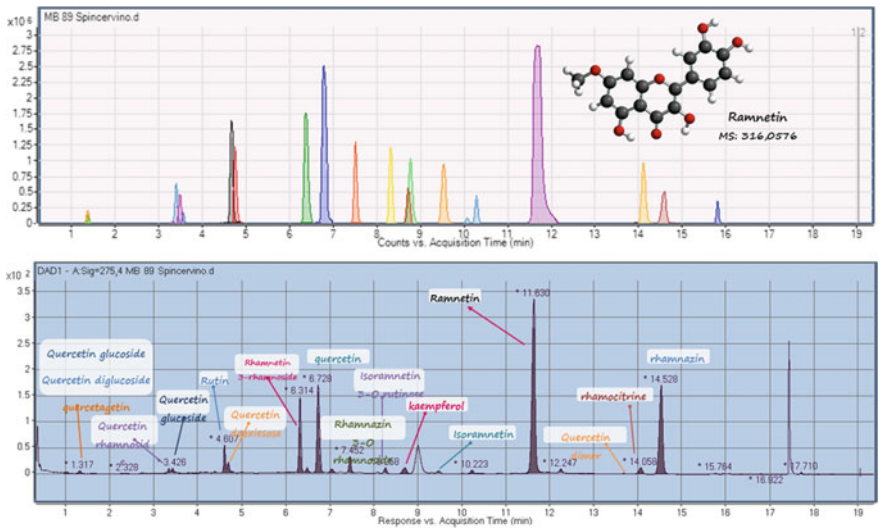

Fig. 1 LC–MS EIC (extracted ion current) and LC–UV–VIS (275 nm) chromatograms of the sample MB89 (*R. cathartica*)

The way of detecting and determine the source of a natural dyestuff lake pigment begins with the study of the cross section both by optical microscopy and SEM/EDX. The clues for selecting a sample for HPLC analysis are high transmission of polarized light, notorious visible fluorescence when lighted with UV light, and high carbon content in EDX, besides the occasional presence of mineral ions (i.e. aluminium, calcium, or sulphate, phosphate) being part of the inorganic support. In the case of synthetic dyes the method is applied in the same manner. For these case studies the database grows with every unknown elucidated. Here, the tools for the analysis of the unknown compound, once isolated by chromatography, are UV–VIS spectra, MS spectra with the value of accurate molecular mass (up to for decimal digits), and isotopic pattern of molecular ion. Both data allows obtaining the molecular formula within a short file of possibilities. These delimit the search, among all the possibilities of colour index [9], to a very limited group of molecules. At least, fragmentation in the MS/MS spectra may help to decide doubtful cases.

3 Natural Dyestuff Analysis. "San Francisco's Life" A Series of XVIII Paintings with Interesting Materials

This analytical technology was also applied to paint micro—samples taking out during the conservation process with the aim of characterize materials, mainly varnishes, dyestuffs and binders, over paints, and all the important data which affects the restoration procedures. The series of paintings represent San Francisco's

life (see as an example Fig. 2) are big size oil on canvas compositions (216 × 270 cm), done by Zacarías González Velázquez (Madrid, 1763—ibídem, 1834), for the decoration of S. Francisco el Grande Basel (Madrid). Pupil of Diego Salvador Maella, he was a Royal court's painter in 1755 and worked as Director of Painting at the Academy of Fine Arts of San Fernando since 1765. He is a recognized XVIII master painter working in wall paintings, some of the with fresco technique. He also painted big format oil paintings such as this set of canvas on the life and miracles of San Francisco. They were done to decorate the cloister of the convent of Madrid's Basilica at 1787. His style is fully inside the Neoclassicism.

Mineral or let us say, inorganic pigments, found in the original brushstrokes are the usual ones found at the end of XVIII century. It is the normal set of classical pigments added to several important contributions of XVIII century chemists to art materials palette. Talking first about the classic mineral pigments found, these are azurite, white lead, charcoal black, vermillion, copper green (verdigris or "*cardenillo*"), red and brown ochre. Some other, specific of XVIII century, are Prussian blue and Naples Yellow (lead antimoniate). The Prussian blue found with PLM was confirmed by IR spectroscopy, because of the presence of cyanide absorption at 2085 cm^{-1}. It is important to notice the observation, in PLM and SEM/EDX studies, of the presence of significant amounts of organic colored grains. This points to the possibility of the presence of organic lakes together with those mineral pigments described above. All these data made these samples so interesting for HPLC studies [10] (Figs. 3 and 4).

In order to check the performance and sensitivity of our chromatographic system, four micro—samples of different colors (blue, green, red and brown colors) were analyzed using the above described methodology in the experimental section. Samples were compared with a huge database created at this facility with a great variety of natural dyestuffs, in order to confirm the presence of coloring compounds, just to be able to assign the obtained result to a particular dyestuff, i.e. species of origin. Particularly, four coloring compounds were detected in the analysis of the selected samples. In dark red samples, carminic acid was detected (Fig. 5). It was not possible to detect and quantify other components of cochineal reds, like kermesic and flavokermesic acid. These last compounds can help us to distinguish among the different types of cochineal (i.e. Polish cochineal, American cochineal or the Armenian one) [11]. The low concentration of these kermesic acid derivative, always below the detection limit of the technique and the date of the paintings points to *Dactylopius coccus* or American cochineal. It was admixed with low quantities of vermillion, and whitish starch grains that can be identified in the cross section.

In blue and green color, traces of indigotine are detected. In the case of green colors the mixture is quite complex. We have a first mineral fraction with copper green, Naples yellow and Prussian blue rich in alumina. In addition, HPLC analysis revealed the composition of the organic colored fraction as indigotine, chrysoeriol and trace amounts of indirubine were clearly identified (Fig. 6). The presence of indigotine was not a surprise, because in these paintings seem to be associated with Prussian blue and it was yet found in blue layers. On the other side, chrysoeriol is a

Fig. 2 "S. Francisco in the presence of sultan". Zacarías González Velázquez

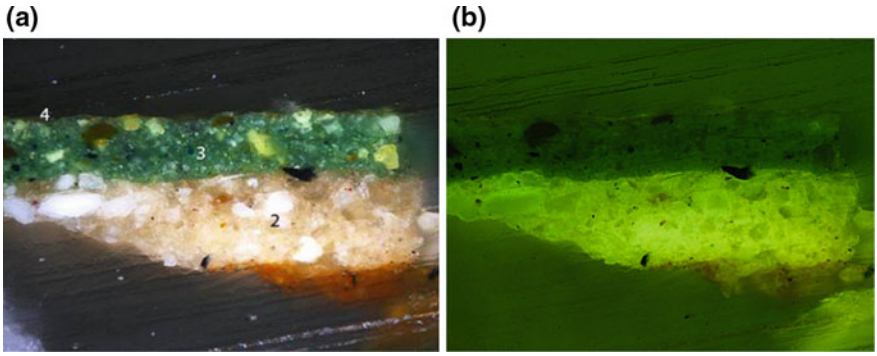

Fig. 3 **a** (left) Cross section of sample PFZ-P3, 300X. Layer 1 is a red imprimatur of red—ochre earths. Layer 2 is a second gray imprimatura. Green layer nr. 3, is a complex mixture of green earth, Naples yellow (lead antimoniate), Prussian blue and a yellow dyestuff. **b** (right) The same cross section under UV light (blue filter), 300X

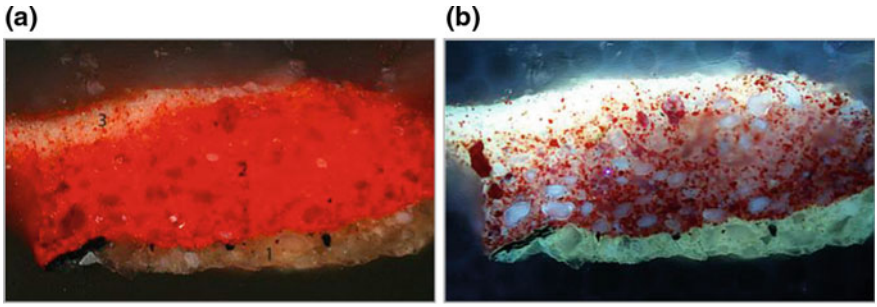

Fig. 4 **a** (left) Cross section of a intense red color mainly done with vermillion PFZ-P7, but also with a lot of starch grains accompanying. Visible reflected polarized light, 500X. Layer 1 is the grey imprimatura. Layer 2 a thick red layer, with vermillion (intense red mass) and starch (dark red areas). **b** (right) The same sample, under UV light (photography was taken with a visible filter), 500X Realize that vermilion is present in the form of intense red spots and grains, and that starch reveals as ovoid shaped white grains

natural methoxylated flavone (5, 7, 4′-trihydroxy-3′-methoxyflavone), present as a minor compound in several broom species. Only in *Cytisus scoparius,* a kind of broom coming from Scotland, chrysoeriol and its C-glycoside derivative are major compounds. In Spain, aliaga (*Genista hirsuta*) could have the same composition, it has been seldom used as dying material, but still is not fully investigated [9]. Broom, made mainly of available *Genista* sp., is a well known raw material used to the manufacture of green pigments, by mixing indigo or woad with a yellow lake made of broom's flowers [12]. Another possible explanation is that has to be checked is that it could by a minor component of local source for indigo *Isatis tinctoria*.

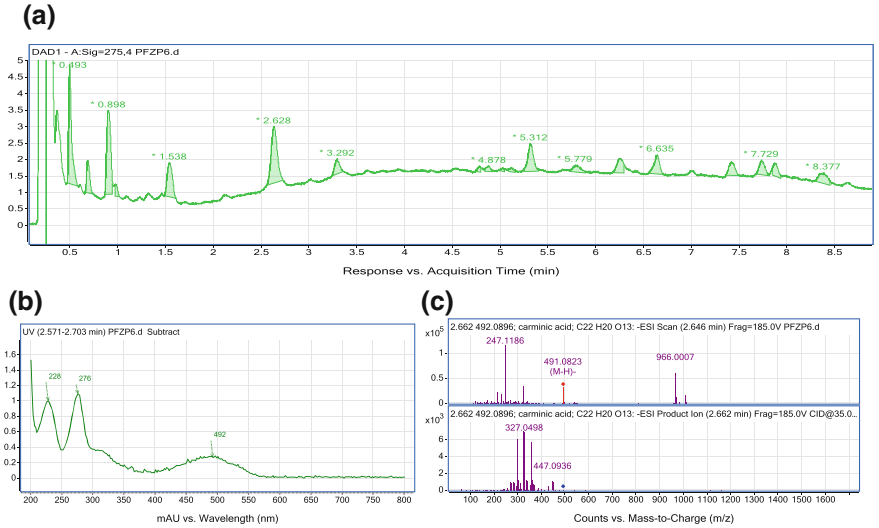

Fig. 5 HPLC analysis of a dark red sample, with vermilion and red lake, PFZ-P6. **a** (top) HPLC chromatogram, registered with the DAD detector at 275 nm. Peak at 2.6 min corresponds to carminic acid. **b** (bottom left) UV–VIS spectrum of carminic acid. **c** (bottom right) MS and MS/MS spectra of the scan at 2.6 min, which corresponds to carminic acid

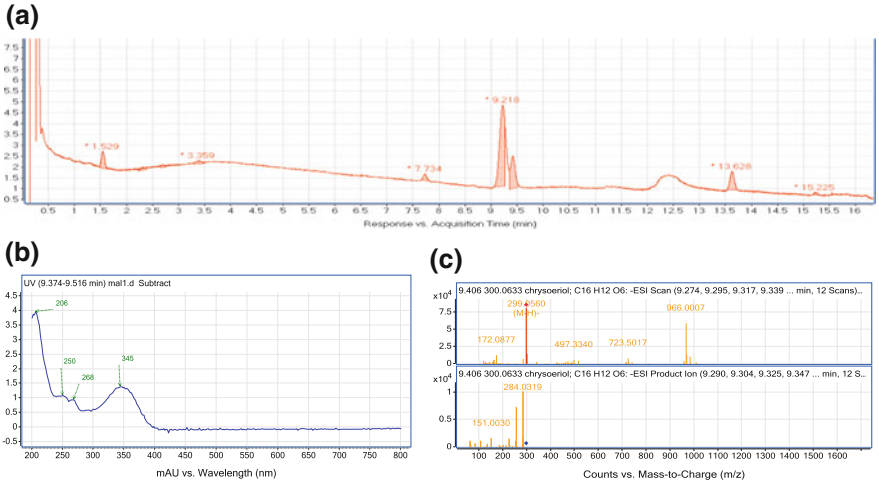

Fig. 6 HPLC analysis of green sample PFZ-P3. Compounds found are chysoeriol, indigotine and indirubine, **a** (top) HPLC chromatogram registered at 275 nm. Peak at 9.4 min corresponds to chrysoeriol, peak at 13.6 min to indigotine and at 15.2 to indirubine. **b** (bottom left) UV–VIS spectrum of chrysoeriol at 9.4 min. **c** (bottom right) MS and MS/MS spectra of scan at 9.4 min

4 Synthetic Dyestuff Analysis. Santa Lucía: A XVIIIth Century Sculpture Overpainted in XXth Century

The first case study is a XVIII century sculpture belonging to the Diocesan Museum of Córdoba's Collection. It is a polychromed wooden statue representing Saint Lucia with her iconografic features. The sample had been collected from a pale green layer in the back part of the saint's robe (see Fig. 7).

As shown in the cross section, the sample presents four superimposed layers: gypsum priming, a red earth layer, a lead white *imprimatura* and an opaque pale green layer. The green layer is composed of a mineral copper green pigment according to SEM imaging and EDX micro elementary analysis. It might be verdigris or altered blue verditer by means of SEM-EDX. Together with the Cu, elementary analysis detected also high contents of C, pointing to the presence of a considerable amount of organics. HPLC–DAD–MS analyses was done in order to characterize this organic compounds. The UV–VIS chromatogram revealed the presence of two blue organic compounds. Retention time, MS and MS/MS data revealed the presence of *methyl blue* (RT: 6.4 min; $C_{37}H_{29}N_3O_9S_3$), an early synthetic dye, and *indigotin* (RT: 13,9; $C_{16}H_{10}N_2O_2$), the main constituent on Indigo dye. As no traces of indirubin has been found in the sample, we concluded that it should be synthetic indigo, as indirubin is always present (as a minor compound) in natural blue dyestuffs derived from *Indigofera* or *Isatis* species. In the case of indigotin, the chromatogram has been recorded in positive polarity mode

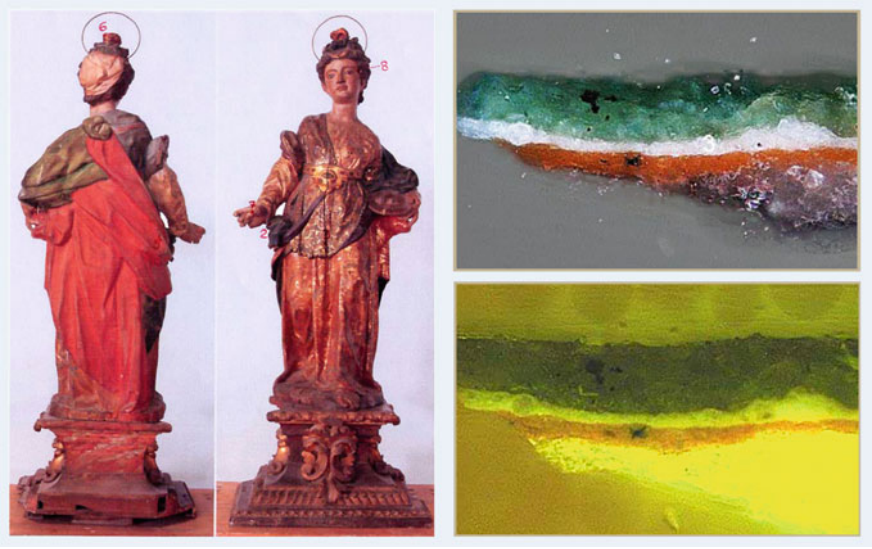

Fig. 7 (left) Saint Lucia, polychromed wood sculpture, XVI century; (right) cross section at 300X of sample SLC-1 (green color of the robe) in visible (UP) and UV light (down)

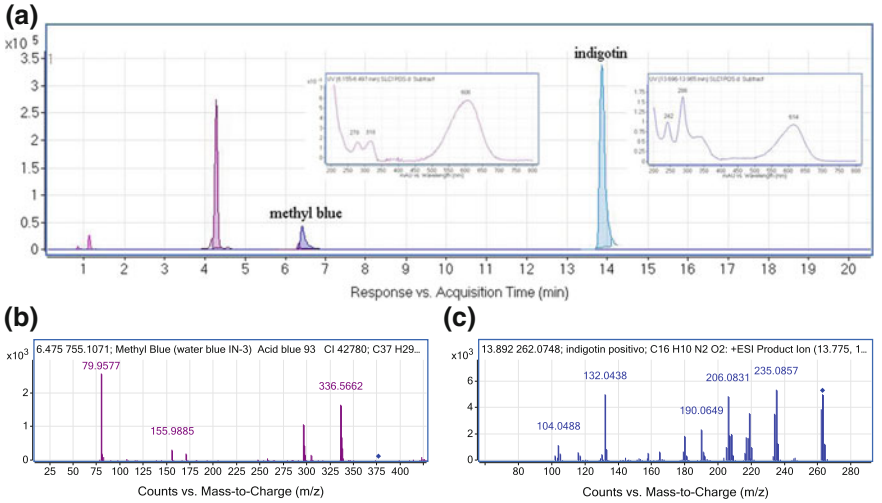

Fig. 8 HPLC–QTOF–MS chromatogram, UV–VIS spectra (up) and MS/MS spectra (down) of the compounds identified in sample SLC-1

of the mass detector, as indigoid dyes present a very low percentage of ionization in negative mode. Mass chromatogram, UV–VIS and MS/MS spectra of the two compounds are shown in Fig. 8. So, although the initial diagnostic for the bluish green was that it was fully original, based only on the elementary analysis EDX, organic analysis of the pigmentation leaded us to conclude that green layer was an overpaint or reintegration layer, done at the beginnings of XXth century or later. The presence of these two organic dyestuffs also explains the dusty and whitish aspect of the green color, as organic dyestuffs suffer a lot more of fading with visible and UV irradiation than minerals pigments do.

5 Synthetic Dyestuff Analysis. Contemporary Art. Paint on Canvas (Oil + Acrylic). Manuel Millares "Cuadro 63" (1959)

Contemporary art is one of the fields where dyestuff analysis can do important advances in the knowledge of organic components, essential for the work of art's appearance and conservation state. We bring here a case study in which a red synthetic organic pigment. "Cuadro 63" (Antonio Millares, 1959) is an abstract composition on canvas support. In it, oil technique coexists with acrylic and may be other synthetic binding media. Organic pigments were suspected to be present using SEM/EDX analysis, as carbon signal increase and no metal was detected during elementary analysis of cross sections. Also, as it may be seen in Fig. 9b the aspect

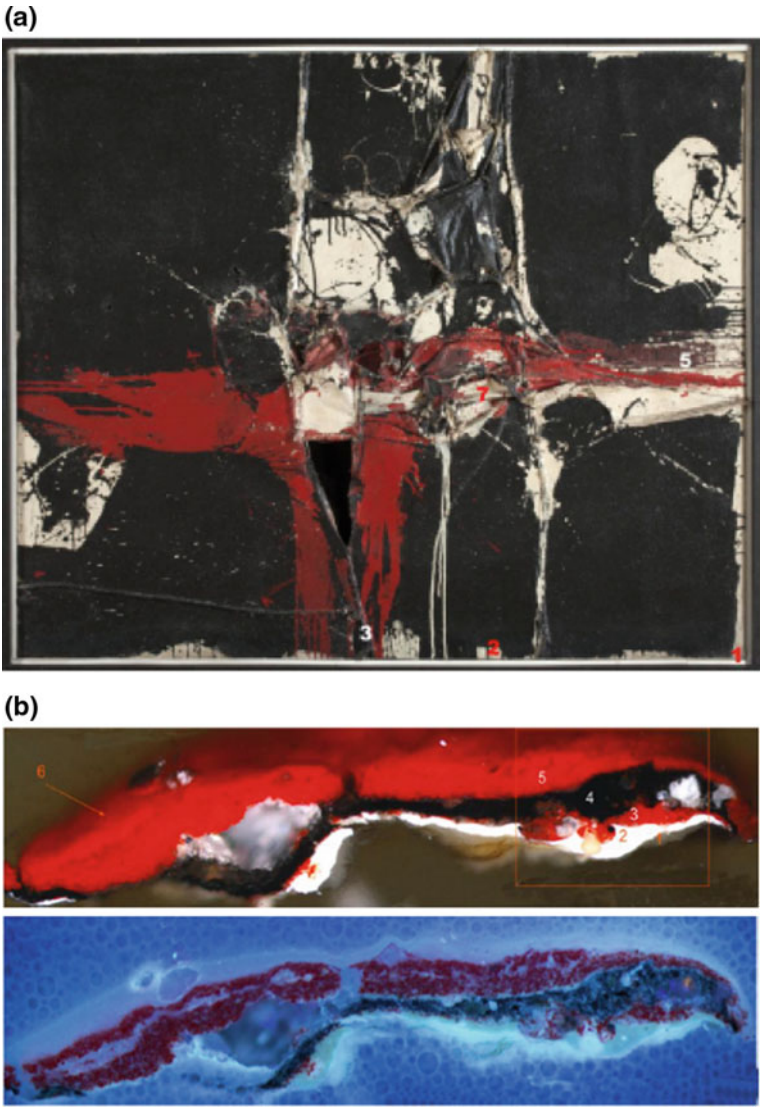

Fig. 9 **a** Up "Cuadro 63". Oil/acrylic on canvas. Manuel Millares (1959). **b** Middle: Cross section corresponding to the intense red color under visible light. Down: the same under UV light

of red color in the section is intense, rather continuous, with a high fluorescence under UV light, so that an organic pigment was suspected.

HPLC–DAD analysis yielded a solitary peak absorbing in the UV region, and also at nearly 500 nm (see Fig. 10a) in the visible region, identifying the dyestuff as a red compound. MS–MS analysis indicated a probable molecular mass of 308 u.m.a and a molecular formula C17H13N3O3 (see Fig. 10b). Not so many known

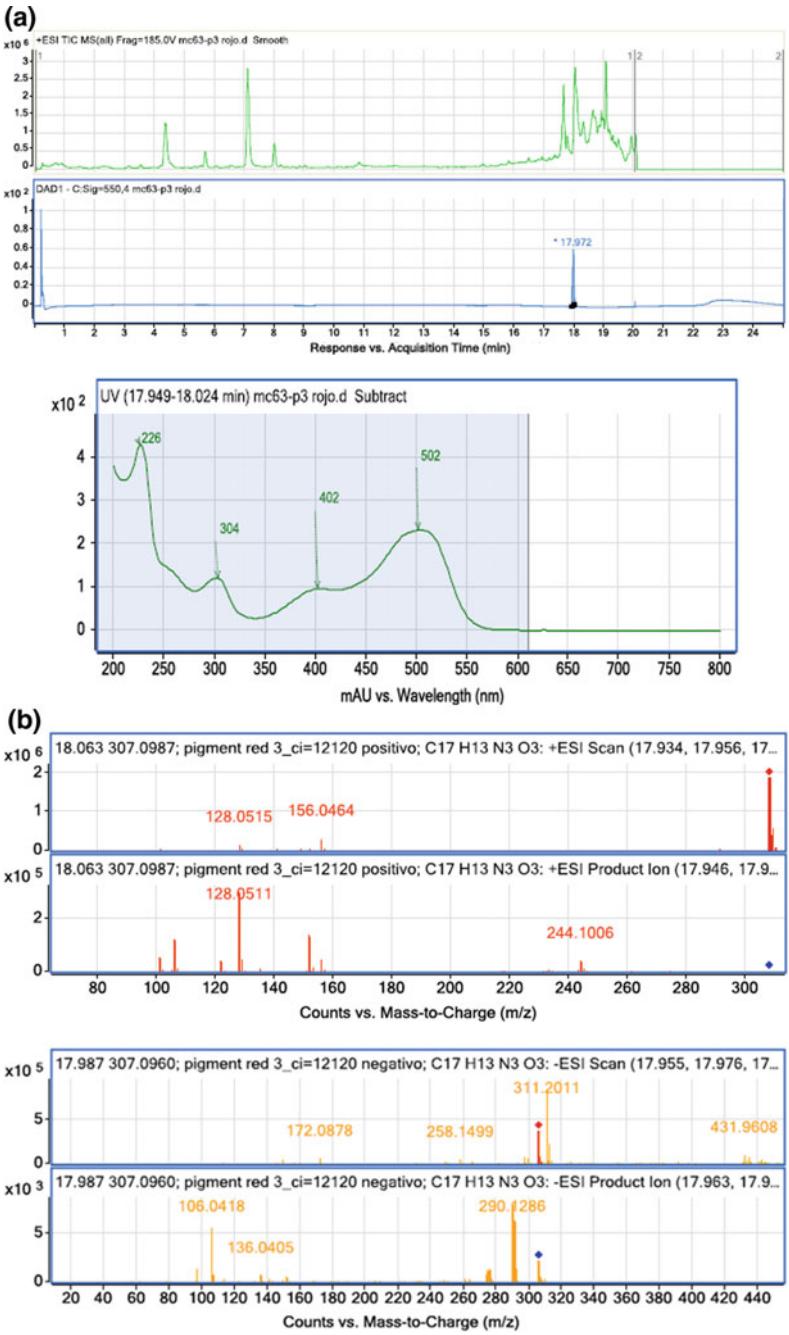

Fig. 10 **a** Up: chromatograms (TIC and Visible at 550 nm) of red paint sample from Millares' painting. Down: UV–VIS absorption spectra of the red dyestuff. **b** Up: Mass-mass spectra acquired with negative polarity of mass detector. Down: Acquired in positive polarity. **c** Chemical structure of Pigment Red 3 (CI 12120) or (1Z)-1-[(4-methyl-2-nitrophenyl) hydrazinylidene] naphthalen-2-one

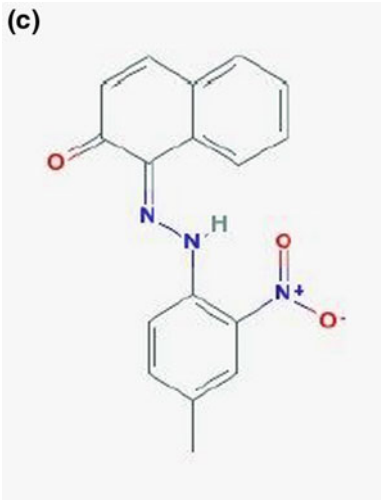

Fig. 10 (continued)

synthetic dyestuff has that molecular mass, and just one matches the molecular formula. It was identified so as Pigment red 3 (Colour index 12120), and its formula can be seen in Fig. 10c.

6 Conclusions

The analytic survey carried out in this research activity shown that there is still a lot of work to do to achieve a complete knowledge and understanding of the world of natural and synthetic organic pigments, its composition and its role in painting film degradation. Although many of the dyes traditionally used by artists are known and well documented, there is a variety of dyeing species not identified yet. With synthetic organic pigments, it is possible to make extraction and identification of soluble or hydrolizable synthetic dyestuffs inside paint matrixes and separate mixtures of them, which allows the source identification, chronological studies and diagnostic analysis of alteration or fading of these organic compounds.

Thanks to its versatility, sensibility and high resolution, the HPLC–Q–TOF–MS proved to be an efficient and powerful tool to the analyses of paint samples and in general for the characterization of Cultural Heritage micro—samples, and to do alteration studies regarding to its chemical stability. Also to the elucidation of unknown dye compounds, using its feasibilities regarding to molecular information, i.e. molecular formulas and fragmentations.

References

1. Schulte F, Brzezinka K-W, Lutzenberger K, Panne U (2008) Raman spectroscopy of synthetic organic pigments used in 20th century works of art. J Raman Spectrosc 39(10):1455–1463
2. Kirby J (2003) A spectrophotometric method for the identification of lake pigment dyestuffs. Nat Gallery Tech Bull 1:35–45
3. Parra E (2001) Estudio de los Materiales de la Colección de El Bosco. In: Garrido C, van Schoute R, El Bosco en el Museo de El Prado. Estudio Técnico. Museo del Prado Madrid, pp 185–211
4. Stathopoulou K et al (2013) Structure elucidation and chromatographic identification of anthraquinone components of cochineal (Dactylopius coccus) detected in historical objects. Analytica Chimica Acta 804:264–272
5. Chernushevich IV et al (2001) An introduction to quadrupole–time-of-flight mass Spectrometry. J Mass Spectrom 36:849–865
6. Sanyova J, Reisse J (2006) Development of a mild method for the extraction of anthraquinones from their aluminum complexes in madder lakes prior to HPLC analysis. J Cult Heritage 7:229–235
7. Vukics V, Guttman A (2010) Structural characterization of flavonoid glycosides by multi-stage mass spectrometry. Mass Spec Rev 29:1–16
8. Parra E, Marras S (2014) Application of HPLC-HR-TOF-MS to the analysis of natural pigments and dyes in paint layers, Art 14. In: 11th international conference on non destructive investigations and microanalysis for the diagnosis and conservation of cultural and environmental heritage. Madrid, junio
9. www.colour-index.com
10. Parra E, Marras S (2014) Detection of starch and organic dyestuffs as painting materials in a series of XVIII century paintings by Zacarías González Velázquez using a HPLC-DAD-QTOF system. In: Technoheritage 2014, 2nd international congress science and technology for conservation of cultural heritage, Seville
11. Wouters J, Verhecken A (1989) The scale insect dyes (Homoptera: Coccoidea). Species recognition by HPLC and diode array analysis of the dyestuff. Annales de la Société Enthomologique de France 01/1989, 25(4):393–410
12. Cardon D (2003) Natural dyes. Sources, tradition and science, Ed. Archetype Books. London, pp 679–682

Chapter 7
Thread Counting in X-Rays of Plain-Weave Painting Canvas

Juan José Murillo-Fuentes and Laura Alba

1 Introduction

Lately, image processing for the analysis and conservation of paintings have received a lot of attention [1]. It has been used to identify the brushstroke of an artist [2], or to study the variation of the thread frequency along the canvas to, mainly, look for matches between paintings [3–7]. In the non-destructive analysis of painting the study of the canvas is of major importance. This analysis leads to interesting conclusions both on the conservation of the painting and on the relation of the painting to other pieces, usually from the same author. In old canvas we cannot, in most cases, use the back of the canvas, as it has been probably relined. A second cloth has been added to strengthen it. An X-ray is of help here, because prior to painting, a primer is applied on the fabric, making threads opaque to the X-ray, see Fig. 1. Furthermore, this priming layer registres the threads deformation due to tension applied to strech the canvas for the first time, even after the canvas is re-stretched. Hence, in areas near nails in the first stretcher bars used, we expect to observe a cusping effect.

Once the X-ray is obtained, the type of fabric is first visually determined. We may find several types of fabrics, ranging from a simple plain-weaves (tafetán) to quite complex twills (sarga). In Fig. 2 we include three examples of fabrics, plain-weave, simple twill and zig-zag twill. While the first is, by far, the most used type, we may also find twill type weaves. Being the simple twill and the zig-zag or fish-bone commonly used. There are more elaborated patterns in twills, such as

J. J. Murillo-Fuentes (✉)
Dep. Teoría de la Señal y Comunicaciones, Escuela Técnica Superior de Ingeniería. Universidad de Sevilla, Seville, Spain
e-mail: murillo@us.es

L. Alba
Documentación Técnica y Laboratorio, Museo Nacional del Prado, Madrid, Spain
e-mail: laura.alba@museodelprado.es

D. M. Bastidas and E. Cano (eds.), *Advanced Characterization Techniques, Diagnostic Tools and Evaluation Methods in Heritage Science*,
https://doi.org/10.1007/978-3-319-75316-4_7

Fig. 1 Radiography interpretation: layers of the painting

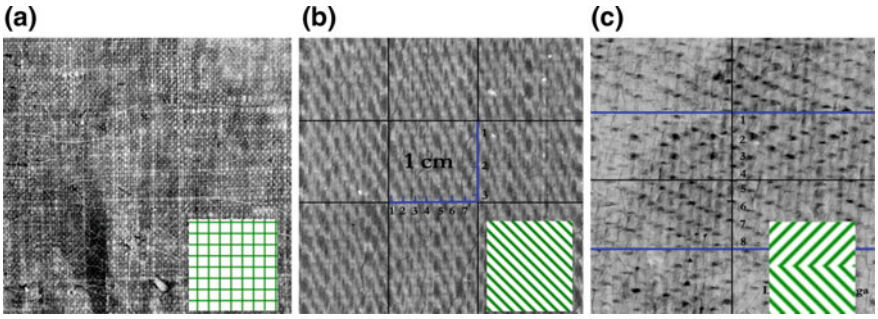

Fig. 2 X-ray of canvases of type **a** plain-weave, **b** simple twill and **c** zig-zag twill. Some details are included with a sketch of the main thread weave

simple diamonds, e.g. used by El Greco, or quite sophisticated patterns, used among others by Murillo.

In this paper we mainly focus on plain-weave canvas. In this scenario, thread counting on X-ray arises as a simple and powerful method. The conservator uses a square pattern, e.g. 1×1 cm, to count the threads on the X-ray by visual inspection. However this is a quite tedious task and it is just performed in a limited number of regions of the canvas.

At the beginning of the last decade, researchers from the signal processing community proposed to apply frequency analysis to the characterization of the fabrics [8]. Some years later, Johnson et al., adapted this method to count threads in X-rays of canvas. A description of this technique along with its features can be found in [7, 9], these include:

- Thread counting along the whole image, for every spot in the canvas.
- Analysis of the angle deviation of the threads from the horizontal and vertical axes.
- Availability to compare two canvases by comparing and matching not only the average counts but also the value of the counts along the width and height of the painting.

The first feature is of interest to take into account information of the whole painting. It also helps to find areas with any irregularity such as a seam or a patch. The analysis can be used to compare two canvases and conclude if they come from

the same roll. The second characteristic is useful when checking for edge cuts or breaks in the canvas. If the fabric has been cut in some edge of the painting, the cusping effect is not present. Finally, two canvases coming from the same roll may present a similar pattern in the weft and/or warp.

In this work we reproduce the results in [9] and apply these tools to paintings from the 17th century of artists Miguel de Pret, Claudio de Lorena, Van Dyck and Rubens. We present the results as a test bed of the results in [9] and its applicability to these old paintings, as a first step for software development. We also face how with little changes the software is valid not only for plain waves but for twills. We have focused and implemented the two first features above, following the requirements of the Museo Nacional del Prado Conservation and Research department in Madrid, Spain. Furthermore, in this work we emphasize the role of the probability density estimation of the thread counting as a feature of the fabrics, when large enough canvases are studied.

2 Methodology

The algorithms are being developed in Matlab®. After the X-ray is loaded, one can process a region or the entire image. A 1×1 cm grid may be showed on the image to help in this task. The intensity of the pixels can also be inverted. Once the area has been selected, we run the counting algorithm. The algorithm provides 6 images and 6 data:

- A pair of images with the horizontal and vertical threads counting. The horizontal thread counting corresponds to the thread counting along the horizontal axis (we count vertical threads), while the vertical thread counting is the thread counting on the vertical direction (we count horizontal threads).
- Two images with the angle deviation along the width and the height. The angle deviation is measured from the vertical axis to the vertical threads, denoted as the horizontal deviation, and from horizontal axis to the horizontal threads, denoted as vertical deviation. The maximum deviation considered is $\pm 25°$.
- The two histograms for the threads counting. The histogram is just a representation of the times each value of the thread counting has been encountered in the horizontal (or vertical) analysis. The range to plot the histogram can be adjusted.
- The mode, mean and standard deviation computed from the histograms of the horizontal and vertical analysis, within the selected range.

The software centers a square window of size $N \times N$ cm in the X-ray to compute the counting and the angle deviation, each pixel of the images above. This window is shifted n cm each time, in both horizontal and/or vertical directions, estimating the frequencies and angle deviations at each point.

The core of the thread counting software is the Fourier transform [10, 11]. In Fig. 3 we depict in the first row some synthetic examples of canvases made from

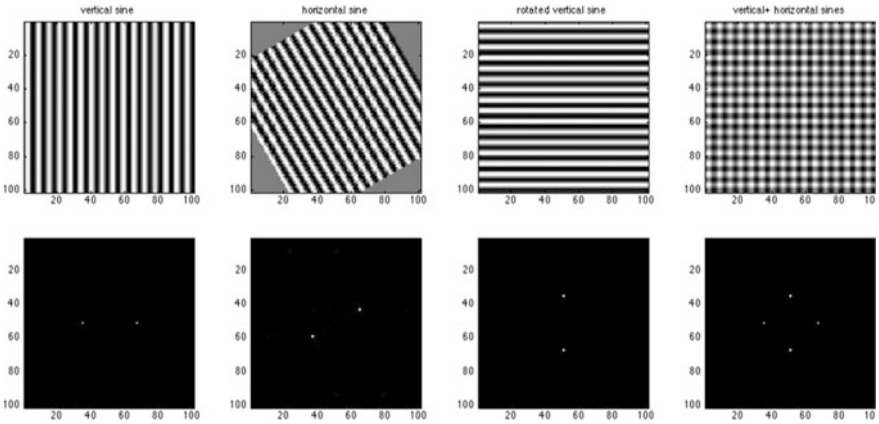

Fig. 3 First row are synthetic models of canvases, made with patterns of parallel lines, second row is the DFT of these models. It can be observed that a pair of points indicates that a parallel patter is present, separation between points depends on the frequency of the lines and the angle of the points their orientation

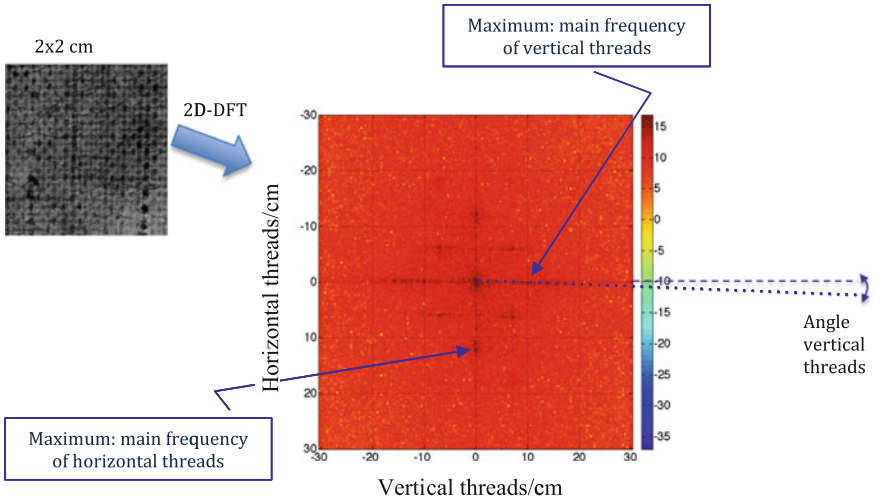

Fig. 4 Thread counting in plain-weave using DFT

parallel lines. Below we include the corresponding DFT. In the last column we have a good model for the plain-weave canvas, where we look for these four maxima in the DFT that would determine threads frequency and angles. The process of thread counting is sketched in Fig. 4, where the DFT of a path is first computed and then we look for the maxima to estimate the frequency of the horizontal and vertical threads, as long as their orientation. One important parameter of this algorithm is the number of points, N_{DFT}, computed. A low value for the number of points, N_{DFT},

involves less computational demanding operations but provides a worse resolution. On the contrary, a high value for f provides a good resolution but leads to a larger running time.

By default, the software performs the thread counting for values between 7 and 25 threads/cm. Later, the user can further limit or extend this range. Points out of the user's selected range are regarded as failed points, i.e. regions where the counting could not be performed.

3 Results of the Thread Counting Software

In this section we present the results of the use of the thread counting software for three types of fabrics: plain-weave, simple twill and the zig-zag twill. The software was initially designed to study plain-weave. However, it can be easily used to study lines patterns in twills, as illustrated in this work.

3.1 Plain Wave

In this section we use the software to analyze one canvas from the 17th century from Miguel de Pret. The canvas, labeled as P07905, a still live painting, is included in Fig. 5.

We include in Fig. 6 two results provided by the software for this painting. The results have been analyzed for a range [8, 14] threads/cm. The study was performed for $N_{\mathrm{DFT}} = 2048$, $N = 1$ cm, and $n = 0.25$ cm. A filtering, based on FFT, was performed to the whole images to remove frequencies below and above the range

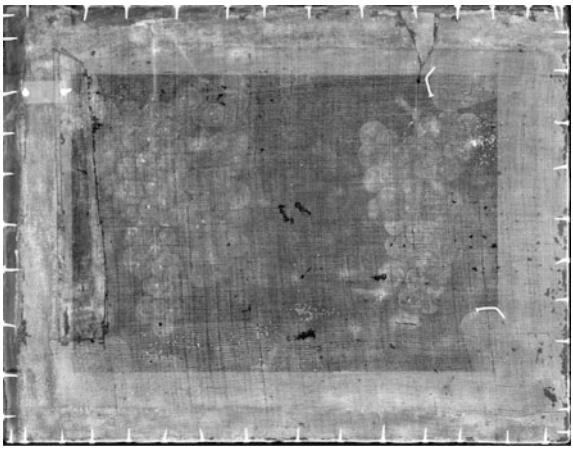

Fig. 5 X-ray of painting P07905 by Miguel de Pret

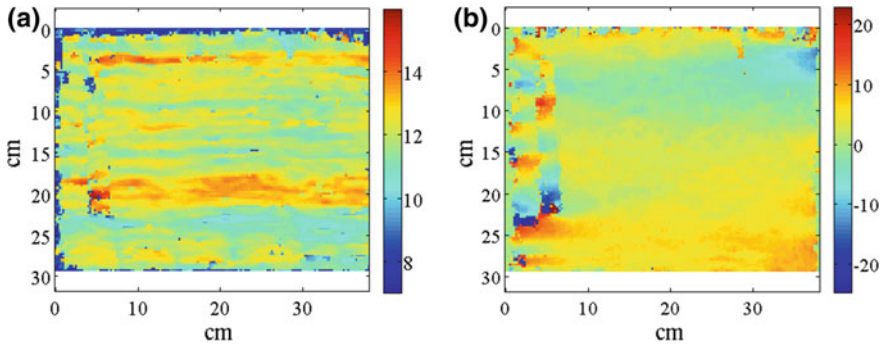

Fig. 6 Counting of horizontal threads and angle variation of vertical threads for P07905

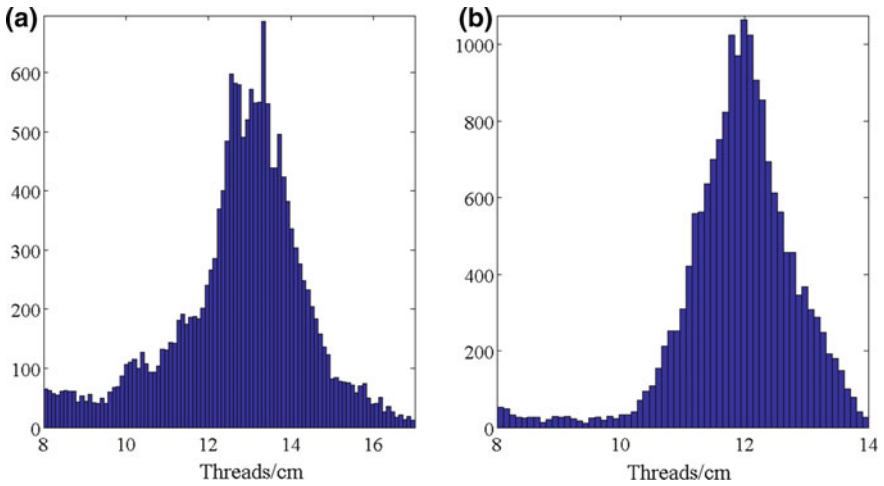

Fig. 7 Histogram of the counting of the **a** vertical and **b** horizontal threads for P07905

[7, 25]. On the left, Fig. 6a, we have depicted the variation of vertical thread counting. The darker spots are regions where the counting fails. They are mainly around the edges. We observe that to the left in the figure we have an 18 cm tall-elongated area about 5 cm far from the left edge. This is a patch that could already be observed in the X-ray image. The interesting point, concluded after applying this software, is that the piece of cloth used, as patch, is similar to the one used in the canvas. In Fig. 6b we have the horizontal angle variation. This image should emphasize the cusping effect in the left and right edges. While the effect is present in the left edge, it is not in the right one. A plausible explanation for both facts is that part of the right canvas was cut. In Fig. 7 we have depicted the histograms for the horizontal and vertical thread counting. The mode, mean and standard deviation (StD) are included in Table 1.

Table 1 Statistics of the tread counting for P7905

Counting of vertical threads			Counting of horizontal threads		
Mode	Mean	StD	Mode	Mean	StD
13.33	12.74	1.61	11.98	11.92	0.90

3.2 *Simple Twills*

A pattern of parallel lines characterizes simple twills, which exhibit some rotation from the vertical. A typical value is around 30°. By rotating the image of the X-ray to align the main lines with the vertical axis we may then run the thread counting software to obtain the frequency of the lines in the pattern and even any variation in the angle. In Fig. 8a we include an area of a simple-twill canvas by Claudio de Lorena, P02254. In Fig. 8b we have the result of the thread counting after rotating the image 30° in the horizontal direction, i.e. counting vertical lines. In Fig. 9a we include the histogram for this study, with a quite sharp and clean peak. The mode obtained was 7.61 lines per cm, with an StD of 0.83. This is a common result in this type of fabric. In Fig. 9b we have the angle deviation. Both thread counting and angle deviation exhibit a quite constant value along the X-ray, except for the bottom, where the framework is located, and some lost part in the right upper corner. The cusping effect is not strong in this type of weave, as plain-twill is less prone to deform. The analysis was performed with $N_{\mathrm{DFT}} = 2048$, $N = 2$ cm and $n = 0.5$ cm.

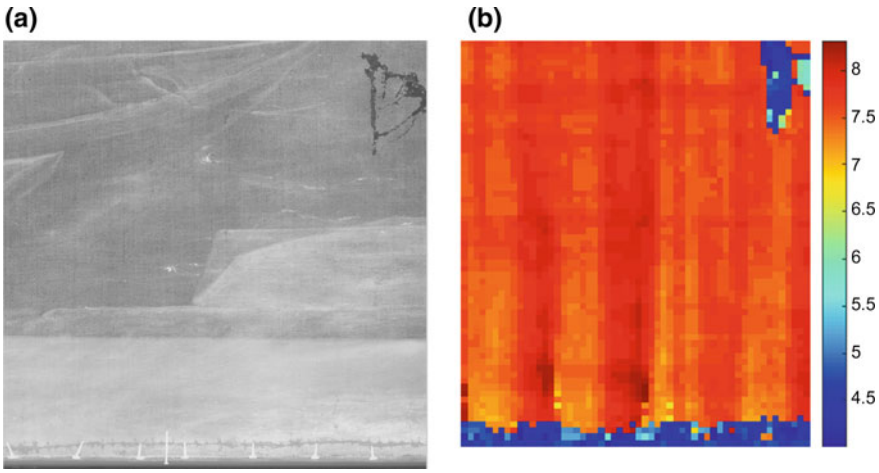

Fig. 8 **a** Area of the X-ray of the painting P02254 processed and **b** number of lines per cm of the pattern

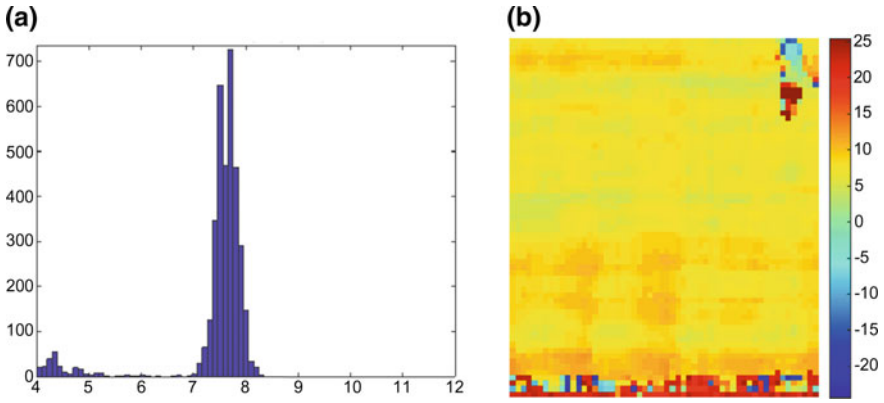

Fig. 9 **a** Histogram of the thread counting and **b** angle variation of the lines of the pattern for P02254

3.3 Zig-Zag Twills

Zig-zag pattern in twills is formed by a set of parallel lines that shift direction in around ±90°, usually a slightly larger value. In Fig. 10 we include an area of the X-ray processed for a canvas by Van Dyck. The lines are not usually parallel to the vertical or horizontal. We propose to use the software but first rotating the X-ray to align them, in this example we rotate it 45°, and run the software as it were plain-weave. The software looks for horizontal and vertical parallel line patters, but it admits an error that we set to ±25°. Therefore, it allows finding the two parallel

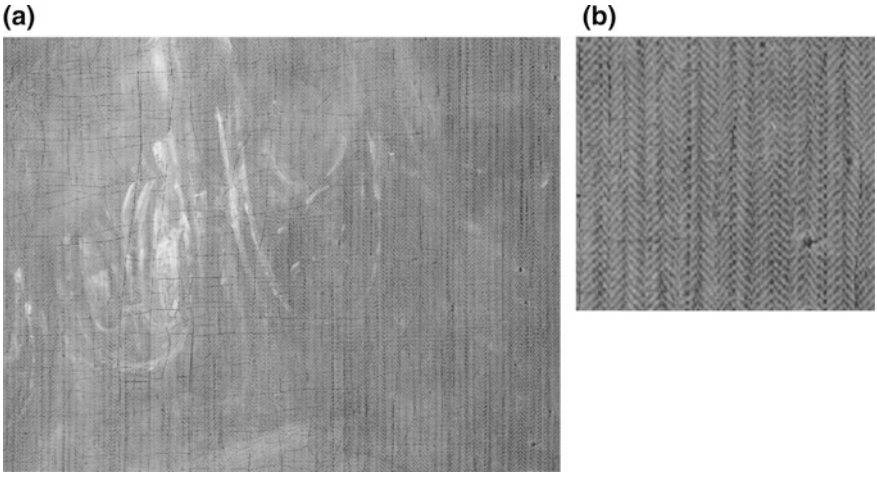

Fig. 10 **a** Processed area of the X-ray of the painting P01474 and **b** a detail

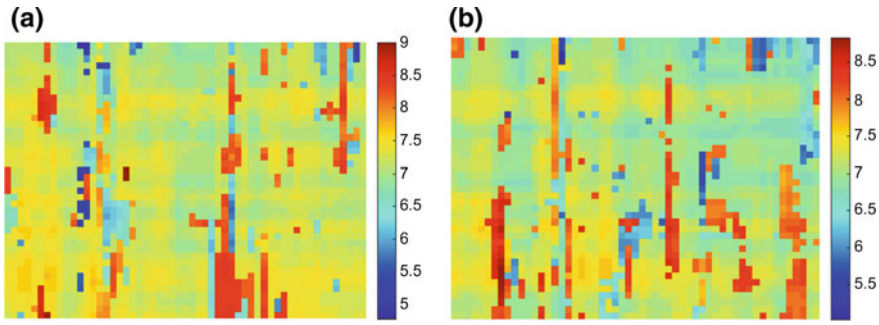

Fig. 11 Lines variation along **a** the horizontal and **b** the vertical for zig-zag twill P02254, after rotating 45°

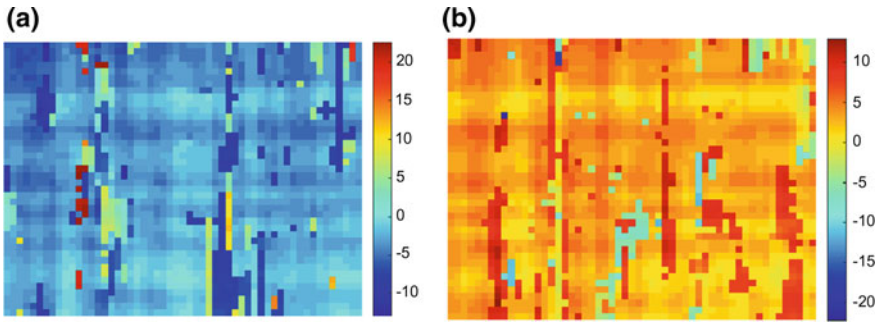

Fig. 12 Angle variation along **a** the horizontal and **b** the vertical for zig-zag twill P02254, after rotating 45°

lines patterns of the zig-zag. In Fig. 11a, b we have the result of the frequency analysis of the parallel line patterns. The histograms, not included, have a maximum at 7.16 with an StD of 0.48. It can be concluded that the lines has a very constant frequency. At some parts of the canvas we observe that threads are slightly more separated. These areas can found in the counting images as vertical elongated areas. In Fig. 12 we have include the angle variation. While lines along the horizontal (left) are in the range 0 to −5 the ones in the vertical have a value in the range 0–5. We may conclude that at the shifts, lines have a change of direction in the range 95–105°.

4 Peter Paul Rubens

In this section we face the thread counting analysis of two paintings from Peter Paul Rubens. The objective is to compare both fabrics to conclude if they could come from the same roll. The study was performed with $N_{\mathrm{DFT}} = 2048$, $N = 2$ cm,

and $n = 0.5$ cm. No filtering was performed to remove frequencies below and above the range [7, 25]. The algorithm used has as main drawback the computing resources needed. The program can handle images with dimensions a few tens of centimeters, providing results within some hours. However, when dimensions tend to be of the order of one meter, times arise significantly. This is the case of these paintings, in Fig. 13. Another problem of big paintings is that the X-rays may be performed in bands of some tens of cm width along one axis. These X-rays are later scanned. The result is a set of X-rays that can be either analyzed in one composed image, or independently. We did perform the thread counting analysis for each X-ray independently, with the software. Later, out of this program, we composed the results for these paintings from these partial results. These compositions are included in this section.

Painting in Fig. 13a, labeled as P01692, was radiated in 7 different tall X-rays. A sample of the composition of the results of the software for every band can be observed in Fig. 14. We excluded the counts out of the range [12, 23]. To the left we have the horizontal threads variations, with deep blue spots there where the counting fails, in this case mainly in the edges and in the seam in the middle. We conjecture that the warp goes from top to bottom, as the width of the loom would be shorter than the 2.5 m, the height of the canvas. Hence, this is thread counting in the warp. To the right we have depicted the difference between the angle deviation in the vertical and horizontal studies. This allows for the inspection of the cusping in one shot, concluding in this case that the original size of the image has been preserved.

In Fig. 15 we include similar results for painting P01693. Here we again composed the results of seven X-rays. We now include the vertical thread counting, as the seam indicates that the warp is in the horizontal axis. Regarding the angle variation, the image to the right evidences that the original size has been preserved, at least it is quite clear in the top, left and right edges.

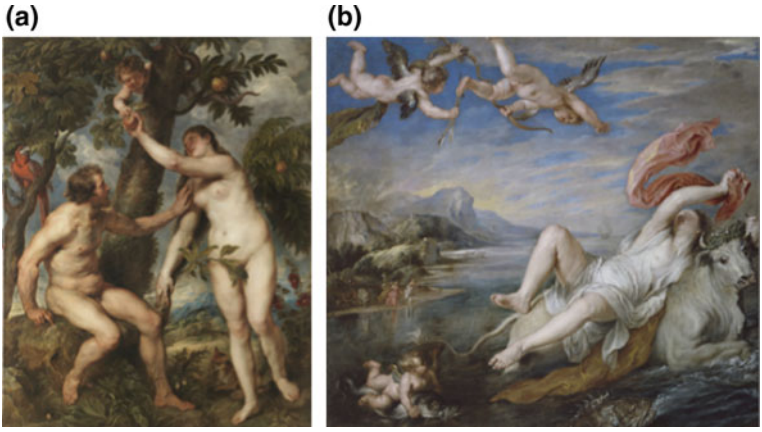

Fig. 13 Paintings by Rubens, in **a** P01692 and in **b** P01693

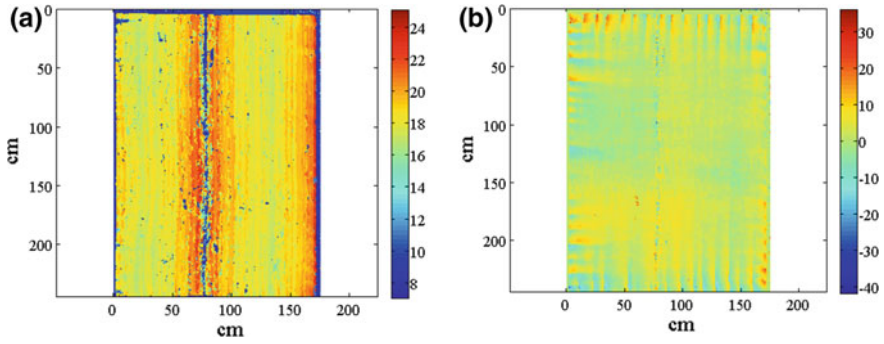

Fig. 14 **a** Counting of vertical threads and **b** difference in angle variations of vertical and horizontal threads for P01692

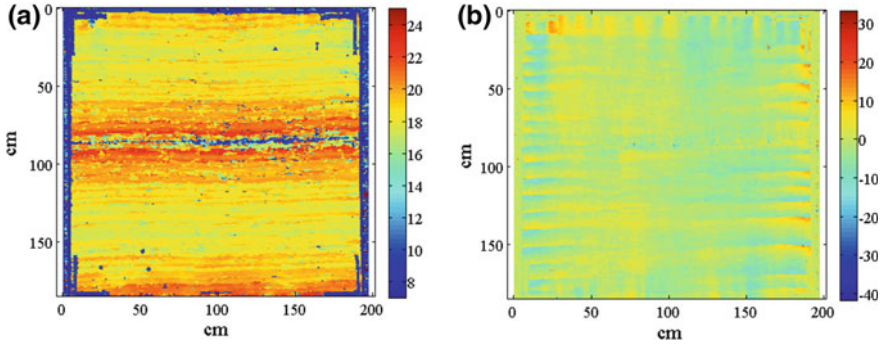

Fig. 15 **a** Counting of horizontal threads and **b** difference in angle variations of vertical and horizontal threads for P01693

Table 2 Statistics of the tread counting for P01692 and P01693

P01692						P01693					
Counting of vertical threads			Counting of horizontal threads			Counting of horizontal threads			Vertical thread counting		
Mode	Mean	StD	Mode	Mean	StD	Mode	Mean	StD	Mode	Mean	StD
18.04	18.66	1.37	17.16	16.67	1.50	18.14	17.78	1.63	18.33	18.90	1.42

We first include some statistics values for the thread counting in both paintings: the mode, mean and StD for the warp of both canvases. Counting of vertical threads for P01692 and horizontal threads for P01693 in Table 2 is quite similar with a very small deviation. Note that although we studied possible counts values from 7 to 25, we later have focused on the range from 12 to 23. Values out of this last range are regarded as failed countings. In the weft, we observe a larger deviation, of one thread/cm. This is standard behavior, as the weft depends on the manual tightening

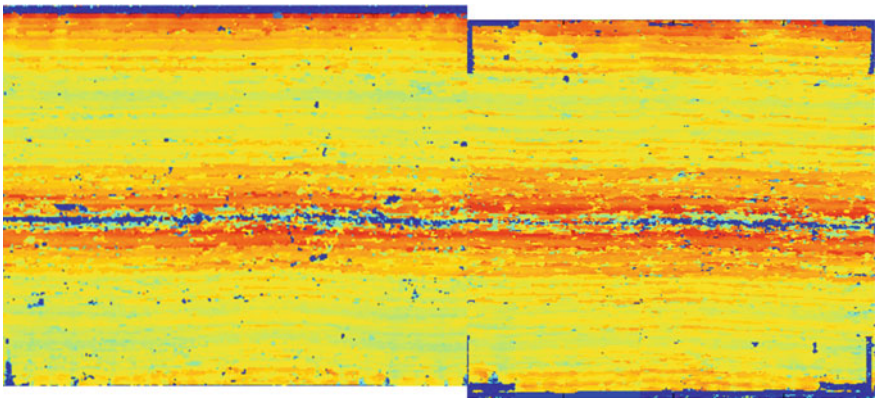

Fig. 16 Match of the warp for P01692 and P01693

of the threads that varies along the roll. The deviation in more than one thread for some of the dimensions makes it difficult to conclude both fabrics coming form the same roll or loom. However, in this scenario, the matching of the variation of the thread counting along what we believe is the warp, helps to prove the similarity between the cloths [12]. In Fig. 16 we have included the matching of the counting of the vertical threads in P01692 and the horizontal ones. In this figure it can be observed that although the variations in one image do not perfectly match the variations in the other one, they very much match in many areas along the warp.

In this work we propose to check for another feature, the shape of the histograms. Note that, because of the big size of the canvases, we have the whole warp, i.e. we have counts along the whole width of the loom. Therefore, imperfections due to how the threads were arranged in the loom, which in turn may be caused by the marks or guides of its breast beam, may cause a pattern to be present in the histograms. We compare the histograms for paintings P01692 and P01693 in Figs. 17 and 18, respectively. Note that the counting of vertical threads in P01692 should be compared to the counting of horizontal ones in P01693, and vice versa. It is most interesting to remark the great similarity between histograms from both paintings. In the weft (to the right in Fig. 17 and to the left in Fig. 18) the histograms fit quite well a Gaussian distribution, explaining the random variation tightening in the weft. Since the pieces of roll used in the paintings are from different parts along the roll, a match between them is not possible. On the other hand, the histogram for the warp may be described as the sum of four sharp Gaussian distributions (see Fig. 17 to the left and Fig. 18 to the right). This can be explained by the deterministic nature of the loom in the warp, assuming that the distance between threads along the warp in the loom is not constant and that four different distances are more probable. In any case, the warp histograms for both paintings are quite rare and at the same time similar. This evidences that both canvas come from the same roll. Up to our knowledge, no previous works have based the study on the similitude between the histograms.

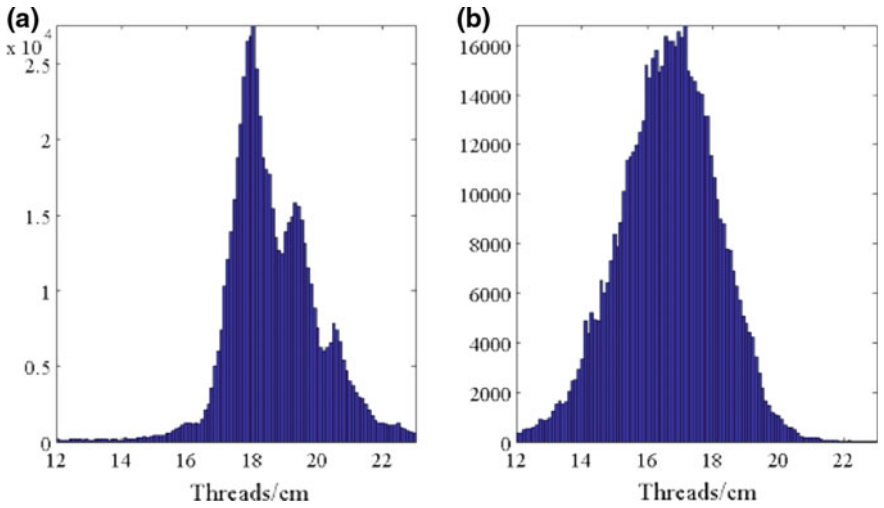

Fig. 17 Histogram of the counting of the **a** vertical and **b** horizontal threads for P01692

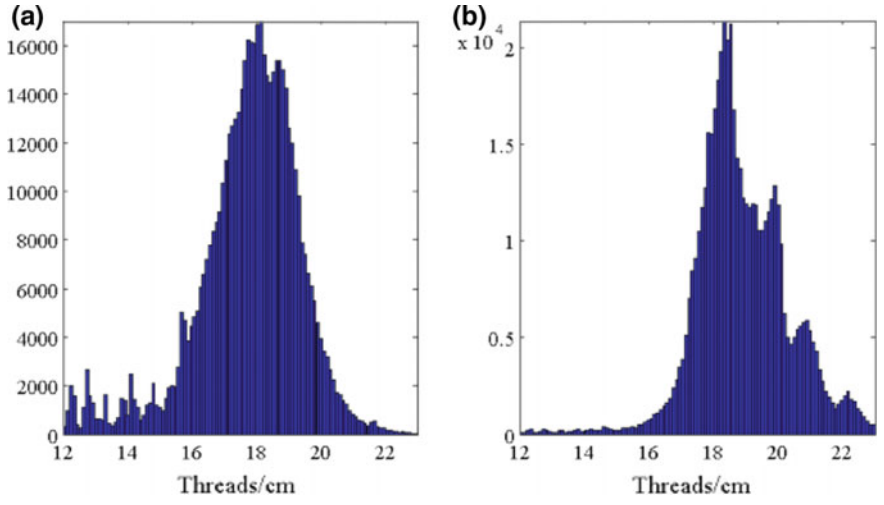

Fig. 18 Histogram of the counting of the **a** vertical and **b** horizontal threads for P01693

5 Conclusions and Future Lines of Research

In this work we report results on the implementation of the thread counting algorithm based on the DFT. We show that as already studied in previous works, it successfully determines the counting for plain-weave canvases. We then show that by tuning its parameters it can be used to determine the frequency of the parallel

line patters of simple twills and zig-zag twills. Finally, we use it to compare two fabrics of two paintings by Rubens, at the Museo N. del Prado, as it was unknown if both have been painted while his stay in Madrid. We conclude, by matching of the counting through the painting, that the same roll was used. Furthermore, in this work we propose to compare the histograms of the full X-ray. Since the big size of these paintings, the whole warp of the loom is present in the canvas. Results are of interest, as the patterns of the histograms are rare and quite close one to each other. This helps to conclude that both fabrics come from the same loom.

Future lines of development include further testing of the software, improving the programing to reduce computing times for large images, multiplatform versions and the extension of the thread counting to other types fabrics. Also, it would be of interest to compare with other thread analysis tools such as those based on histograms-of-oriented-gradient (HOG) features [4] and the 2D synchrosqueezed Transforms [3].

References

1. Barni M, Pelagotti A, Piva A (2005) Image processing for the analysis and conservation of paintings: opportunities and challenges. IEEE Sig Process Mag 22(5):141–144. https://doi.org/10.1109/MSP.2005.1511835
2. Johnson CR Jr, Hendriks E, Berezhnoy IJ, Brevdo E, Hughes SM, Daubechies I, Li J, Postma E, Wang JZ (2008) Image processing for artist identification. IEEE Sig Process Mag 25(4):37–48. https://doi.org/10.1109/msp.2008.923513
3. Yang H, Lu J, Brown WP, Daubechies I, Ying L (2015) Quantitative canvas weave analysis using 2-D synchrosqueezed transforms. IEEE Sig Process Mag 32(4):55–63. https://doi.org/10.1109/MSP.2015.2406882
4. van der Maaten L, Erdmann R (2015) Automatic thread-level canvas analysis. IEEE Sig Process Mag 32(4):38–45. https://doi.org/10.1109/msp.2015.2407091
5. Johnson CR Jr, Johnson DH, Verslype I, Lugtigheid R, Erdmann RG (2013) Detecting weft snakes. ArtMatters Int J Tech Art Hist 5:48–52
6. Fondón-García I, Simois FJ, Murillo-Fuentes JJ (2014) Software tool for thread counting in X-rays of plain-weave painting canvas. In: Proceedings of 11th international conference on non-destructive investigations and microanalysis for diagnostics and conservation of cultural and environmental heritage
7. Erdmann R, Johnson CR, Jr, Schafer M, Twilley J (2013) Reuniting Poussin's Bacchanals painted for Cardinal Richelieu through quantitative canvas weave analysis. In: Proceedings of 41st annual meeting American institute conservation historic and artistic works
8. Escofet J, Millán MS, Ralló M (2001) Modeling of woven fabric structures based on Fourier image analysis. Appl Opt 40:6170–6176
9. Johnson DH, Sun L, Johnson CR, Hendriks E (2010) Matching canvas weave patterns from processing X-ray images of master paintings. In: IEEE international conference on acoustics speech and signal processing (ICASSP), pp 958–961
10. Oppenheim AV, Schafer RW (1999) Discrete-time signal processing. Prentice-Hall, Upper Saddle River, NJ

11. Osgood B (2016) Lecture notes for EE261, the Fourier Transform and its applications, 3rd ed, https://see.stanford.edu/materials/lsoftaee261/book-fall-07.pdf, Cambridge Stanford University. Accessed 19 Nov 2016
12. Johnson DH, Hendriks E, Geldof M, Johnson CR, Jr (2010) Do weave matches imply canvas roll matches? In: Proceedings of 38th annual meeting American institute conservation historic and artistic works